

Unveiling the properties and origin of massive quenched galaxies at $z \geq 2$ in the COLIBRE hydrodynamical simulations

Ángel Chandro-Gómez^{1,2*}, Claudia del P. Lagos^{1,2}, Chris Power^{1,2}, Willian M. Baker³, Alejandro Benítez-Llambay⁴, Evgenii Chaikin⁵, Harry G. Chittenden^{6,7}, Camila Correa⁵, Carlos S. Frenk⁸, Filip Huško⁵, Robert J. McGibbon⁵, Themiya Nanayakkara^{6,7}, Sylvia Ploeckinger⁹, Alexander J. Richings^{10,11}, Matthieu Schaller^{5,12}, Joop Schaye⁵ and James W. Trayford¹³

¹ International Centre for Radio Astronomy Research (ICRAR), The University of Western Australia, 35 Stirling Highway, Crawley, WA 6009, Australia

² ARC Centre for All-Sky Astrophysics in 3 Dimensions (ASTRO 3D)

³ DARK, Niels Bohr Institute, University of Copenhagen, Jagtvej 155A, DK-2200 Copenhagen, Denmark

⁴ Dipartimento di Fisica G. Occhialini, Università degli Studi di Milano Bicocca, Piazza della Scienza, 3 I-20126 Milano MI, Italy

⁵ Leiden Observatory, Leiden University, PO Box 9513, NL-2300 RA Leiden, The Netherlands

⁶ Centre for Astrophysics and Supercomputing, Swinburne University of Technology, P.O. Box 218, Hawthorn VIC 3122, Melbourne, Australia

⁷ JWST Australia Data Centre, Swinburne Advanced Manufacturing and Design Centre, John Street, Hawthorn VIC 3122, Australia

⁸ Institute for Computational Cosmology, Department of Physics, University of Durham, South Road, Durham, DH1 3LE, UK

⁹ Department of Astrophysics, University of Vienna, Türkenschanzstrasse 17, A-1180 Vienna, Austria

¹⁰ Centre for Data Science, Artificial Intelligence and Modelling, University of Hull, Cottingham Road, Hull, HU6 7RX, UK

¹¹ E. A. Milne Centre for Astrophysics, University of Hull, Cottingham Road, Hull, HU6 7RX, UK

¹² Lorentz Institute for Theoretical Physics, Leiden University, PO Box 9506, NL-2300 RA Leiden, The Netherlands

¹³ Institute of Cosmology and Gravitation, University of Portsmouth, Dennis Sciama Building, Burnaby Road, Portsmouth PO1 3FX, UK

Accepted XXX. Received YYY; in original form ZZZ

ABSTRACT

JWST has uncovered a substantial population of Massive ($M_\star \gtrsim 10^{10} M_\odot$), Quenched Galaxies (MQGs) in the early Universe ($z \gtrsim 2$), whose properties challenge current galaxy formation models. In this paper, we examine this population of MQGs within the new COLIBRE cosmological hydrodynamical simulations. We report number densities and stellar mass functions in broad agreement with the latest observations. The predicted quenching and formation timescales are qualitatively consistent with observational inferences. Leveraging the state-of-the-art physics in COLIBRE, the model predicts that MQGs have dust and H₂ fractions more than 1 dex lower than their massive star-forming counterparts; while their sizes and kinematics remain broadly similar. We further explore the processes driving galaxies to become massive and quenched in COLIBRE, identifying active galactic nucleus (AGN) feedback as the primary quenching mechanism. Compared to star-forming galaxies of similar mass, MQGs host more massive black holes (BHs) and exhibit higher star formation efficiencies. These differences arise from their environments, particularly at local (0.3 cMpc) to intermediate scales (1.0 cMpc) before quenching, where overdense regions are associated with enhanced gas inflows, higher BH accretion and, hence, feedback power. We find that about 55% of MQGs survive as the main progenitors of $z = 0$ galaxies when they are selected at $z = 3$, although up to 55% experience rejuvenation episodes. Our results provide robust predictions for MQGs, show that tensions with observations are reduced when an effective observational uncertainty is forward-modelled, and clarify the mechanisms behind their origin.

Key words: methods: numerical – galaxies: formation – galaxies: evolution – galaxies: high-redshift

1 INTRODUCTION

The *James Webb Space Telescope* (*JWST*) has ushered in a new era in observational astronomy, thanks to its high sensitivity and resolution, providing an unprecedented view of the early Universe (see, for example, Adamo et al. 2025, for a review). The first *JWST* results revealed a surprisingly large population of Massive, Quenched Galaxies (hereafter MQGs) at high redshift ($z > 3$), with stellar masses $M_\star \gtrsim 10^{10} M_\odot$ and negligible star formation (Nanayakkara

et al. 2022; Carnall et al. 2023a). Such galaxies had already been detected (Glazebrook et al. 2017; Schreiber et al. 2018; Valentino et al. 2020; Weaver et al. 2022), but *JWST* showed that their number densities are higher than previously thought, that older MQGs exist and that they are found at even higher redshifts (Weibel et al. 2025), implying that this population is not as rare as once believed.

The high number densities inferred from the first *JWST* observations were initially difficult to reconcile with the hierarchical Λ Cold Dark Matter (hereafter Λ CDM) model; these objects appeared too massive for the early epochs at which they are detected and would require implausibly high star formation efficiencies (Boylan-Kolchin

* E-mail: angel.chandrogomez@research.uwa.edu.au

2023). However, as observational samples have grown, through large photometric surveys (e.g. Baker et al. 2025c; Stevenson et al. 2025) and spectroscopic confirmations (e.g. Nanayakkara et al. 2025; Zhang et al. 2025) extending to $z \gtrsim 2$, the inferred number densities have consistently decreased, easing much of the tension. In fact, the initially reported high number densities by Carnall et al. (2023a) have since been revised downward in light of more recent analyses. However, they remain more than a factor of two higher than earlier ground-based estimates. New surveys are beginning to unveil the diverse properties of MQGs, extending stellar mass and star formation rate (SFR) measurements to include dust content (Lee et al. 2024), sizes (Kawinwanichakij et al. 2025) and kinematics (Pascalau et al. 2025), and they are enabling comparisons with lower- z counterparts.

The short timescales on which MQGs form and quench are also puzzling. Spectroscopic observations indicate that some quenched systems must have formed rapidly, as early as when the Universe was about or even less than one Gyr old (with examples at $z \approx 11$; Glazebrook et al. 2024). These studies suggest that strong starburst episodes drive this early mass assembly (Forrest et al. 2020). In the local Universe, feedback processes explain the quiescent state of galaxies (e.g. Man & Belli 2018); these include internal mechanisms such as supernova (SN) and active galactic nucleus (AGN) feedback and external influences such as interactions with, and regulation by, the environment. SN feedback is insufficient to quench massive systems and predominantly affects lower-mass galaxies (Benson et al. 2003), even at high redshifts (e.g. Gelli et al. 2023); while it is believed that environment is already important at high redshifts (e.g. Jin et al. 2024), its role in quenching massive galaxies seems to be minor (e.g. Lee et al. 2015; Shuntov et al. 2025).

Given the short quenching timescales of MQGs, the most plausible mechanism is seen as AGN feedback, the injection of energy and momentum by central supermassive black holes (BHs) into their surroundings. AGN feedback is understood to play a crucial role in shaping the properties of massive galaxies at low redshifts, being necessary to explain the high-mass end of the stellar mass function (SMF) (e.g. Benson et al. 2003). It suppresses star formation by expelling cold gas through powerful outflows (ejective feedback; Di Matteo et al. 2005; Booth & Schaye 2009) and by heating the surrounding medium and preventing further accretion (preventive feedback; Bower et al. 2006; Croton et al. 2006). Observational evidence indicates that AGNs are active in early MQGs, through detections of X-ray (Ito et al. 2022; Stevenson et al. 2025; Baker et al. 2025c), broad emission lines (Martínez-Marín et al. 2024) and AGN-driven outflows seen in absorption lines (Davies et al. 2024; D'Eugenio et al. 2024; Park et al. 2024).

The last decade has witnessed a remarkable growth in galaxy formation simulations that model statistical samples of galaxies within cosmological volumes, capable of producing population properties that are in broad agreement with observations of galaxies in the local Universe (e.g. Schaye et al. 2015; Pillepich et al. 2018). They accomplish this by calibrating parameterised sub-grid models for, for example, BH growth and feedback, to recover particular sets of observational data (e.g. Crain et al. 2015; Chaikin et al. 2025a), typically from low-redshift galaxy surveys, while still enabling genuine predictions for other galaxy properties. Such simulations provide an ideal framework to test what role AGN feedback plays in quenching MQGs at high redshift, and to connect them to their low- z descendants, a link that is difficult to establish observationally (see e.g. the reviews by Somerville & Davé 2015; Crain & van de Voort 2023).

In this paper, we use the new COLIBRE cosmological hydrodynamical simulations (Schaye et al. 2025; Chaikin et al. 2025a) to investigate the properties and origins of MQGs at high redshift.

Chaikin et al. (2025b) show that the evolution of the galaxy SMF in COLIBRE is reproduced across the full redshift range ($z = 0 - 12$) for which observational data are available. That work presents the first results on the abundance of MQGs in these simulations, demonstrating good agreement with *JWST* data. Here, we extend it with a more comprehensive analysis of the COLIBRE MQGs, providing further details on their abundance and assessing whether the COLIBRE model can reproduce the many other key characteristics of MQGs as revealed by recent *JWST* surveys, and identifying the physical mechanisms responsible for their rapid formation and quenching. We focus on a comprehensive set of galaxy properties, including stellar masses, SFRs, dust and molecular gas content, sizes and kinematics; and compare them with the latest observational constraints. Furthermore, by tracing the evolutionary histories of individual MQGs, we also explore the role of BH growth and their associated AGN feedback, as well as environmental factors in driving quenching of these systems. The tracking is performed down to $z = 0$, enabling us to examine the fate of MQGs after quenching.

The structure of this paper is as follows. In § 2 we describe the COLIBRE simulations and their physics models relevant to MQGs. § 3 outlines our sample selection, as well as the properties we analyse throughout the paper. Predictions across a wide range of observables, including number densities, SMFs, star formation histories (SFHs), dust and molecular gas fractions, sizes and kinematics; are presented in § 4. Next, we follow the evolutionary journey of MQGs predicted by the simulations, examining the mechanisms that quench them, tracing their past evolution to understand the quenching origin, and exploring the potential for renewed star formation (rejuvenation) in § 5. Finally, § 6 summarises our results.

2 THE COLIBRE SIMULATION SUITE

For this analysis, we use the new COLIBRE¹ large-volume cosmological hydrodynamical simulations (Schaye et al. 2025; Chaikin et al. 2025a). The COLIBRE suite comprises several simulations that vary in volume (periodic box size of $L = 25 - 400$ cMpc per side), resolution (mean initial gas particle mass, m_g , and mean DM particle mass, m_{DM} , $\sim 10^5 - 10^7 M_{\odot}$), and AGN feedback model (either fiducial thermal or hybrid thermal+jet). Table 1 summarises the simulation set used in this analysis, which allows us to assess how resolution, volume, and feedback variations influence the properties of MQGs. Among these, we adopt the L200m6 simulation as our fiducial choice, as it offers the best compromise between volume ($L = 200$ Mpc per side), sufficient to sample rare MQGs, and resolution (m_g and $m_{\text{DM}} \sim 10^6 M_{\odot}$), adequate to capture their internal structure more accurately. The relatively small gravitational softening lengths (ϵ_{com} and ϵ_{prop}) of this run are particularly important for more reliably analysing galaxy sizes and kinematics, as discussed in § 4.5 and Appendix E.

2.1 Simulation methods

The initial conditions (ICs) are generated with MONOFONIC (Hahn et al. 2020; Michaux et al. 2021) and evolved using the SWIFT code (Schaller et al. 2024). The density field is sampled with cold DM and baryonic particles, with the latter initially representing gas but able to convert into collisionless stellar or BH particles. To suppress spurious energy transfer between DM and stellar particles, the ICs of

¹ <https://colibre-simulations.org/>

Table 1. COLIBRE hydrodynamical simulations used in this work. L : the periodic box size in comoving Mpc (cMpc); N_b : the initial number of baryonic particles in the volume; N_{DM} : the number of DM particles in the volume; m_g : the mean initial gas particle mass in M_{\odot} ; m_{DM} : the mean DM particle mass in M_{\odot} ; ϵ_{com} : the gravitational softening length in ckpc; ϵ_{prop} : the maximum gravitational softening length in proper kpc (pkpc); and the type of AGN feedback implemented (thermal or hybrid including thermal+jet); $N_{\text{MQ}}(z = 3)$: the number of MQGs selected at $z = 3$ using the criteria defined in § 3.1. We highlight in bold the simulation adopted as fiducial in this work.

COLIBRE sim.	L/cMpc	N_b	N_{DM}	m_g/M_{\odot}	m_{DM}/M_{\odot}	$\epsilon_{\text{com}}/\text{ckpc}$	$\epsilon_{\text{prop}}/\text{pkpc}$	AGN feedback model	$N_{\text{MQ}}(z = 3)$
L050m5	50	1504 ³	4×1504^3	2.30×10^5	3.03×10^5	0.9	0.35	thermal	2
L100m6	100	1504 ³	4×1504^3	1.84×10^6	2.42×10^6	1.8	0.7	thermal	79
L200m6	200	3008³	4×3008^3	1.84×10^6	2.42×10^6	1.8	0.7	thermal	470
L200m7	200	1504 ³	4×1504^3	1.47×10^7	1.94×10^7	3.6	1.4	thermal	1527
L400m7	400	3008 ³	4×3008^3	1.47×10^7	1.94×10^7	3.6	1.4	thermal	12359
L100m6h	100	1504 ³	4×1504^3	1.84×10^6	2.42×10^6	1.8	0.7	hybrid (thermal+jet)	5
L200m7h	200	1504 ³	4×1504^3	1.47×10^7	1.94×10^7	3.6	1.4	hybrid (thermal+jet)	310

the simulations contain four times more DM particles than baryonic ones (Ludlow et al. 2019). Stellar and gas particles can increase or decrease their mass due to stellar mass loss. Gas particles exceeding $4 m_g$ are split into two nearly co-spatial equal-mass particles to avoid baryonic particles with very different masses. Gravity is solved with a 4th-order fast multipole method (Dehnen 2014) and softened using a kernel with a functional form given by Wendland (1995), while hydrodynamics is handled with the SPHENIX implementation of smoothed particle hydrodynamics (SPH) (Borrow et al. 2022) using a quartic spline kernel. The simulations are run from $z = 63$ to $z = 0$, adopting the DES Y3 ‘3x2pt + All Ext.’² Λ CDM cosmology (Abbott et al. 2022): $h = 0.681$, $\Omega_{\Lambda} = 0.693922$, $\Omega_m = 0.306$, $\Omega_{\text{CDM}} = 0.256011$, and $\Omega_b = 0.0486$.

Between $z = 30$ and $z = 0$, the simulations output 36 full snapshots and 92 reduced ‘snipshots’ (which record only BH properties and a limited subset of gas and stellar properties). Haloes are first identified with a friends-of-friends (FoF) algorithm that links DM particles separated by less than 0.2 times the mean inter-particle distance, with baryonic particles attached to the nearest DM neighbour. FoF groups with fewer than 32 particles are discarded. Subhaloes are then identified using the HBT-HERONS code (Forouhar Moreno et al. 2025), an extension of HBT+ (Han et al. 2018), which tracks the most bound particles of each structure from the time it was first identified. This explicit temporal tracking improves detection of substructures near halo centres (Forouhar Moreno et al. 2025) and prevents unphysical mass fluctuations in merger trees (Chandrigómez et al. 2025). Finally, the SOAP code (McGibbon et al. 2025) computes halo, subhalo and galaxy properties across multiple 3D and projected apertures, defined either by fixed sizes (e.g. 10, 30, 50 pkpc) or overdensity thresholds (e.g. 200 times the mean density of the Universe, 200 or 500 times the critical density of the Universe), using all or only the bound particles.

2.2 Subgrid prescriptions

Compared to other large-volume hydrodynamical simulations, COLIBRE introduces key innovations in its subgrid prescriptions, which capture processes occurring below the simulation’s spatial resolution.

² Maximum-posterior likelihood values from the Dark Energy Survey year three (DES Y3) assume a spatially flat universe and combine constraints from three two-point correlation functions: cosmic shear, galaxy clustering, and galaxy-galaxy lensing, with external data from baryon acoustic oscillations (BAO), redshift-space distortions, type Ia SNe, and Planck observations of the Cosmic Microwave Background (CMB) (including CMB lensing), Big Bang nucleosynthesis, and local measurements of the Hubble constant.

These improvements are briefly outlined below, although we refer the reader to Schaye et al. (2025) and the individual papers describing each subgrid model for a detailed discussion. The parameters of these models are calibrated (Chaikin et al. 2025a) to reproduce the $z = 0$ galaxy SMF (Driver et al. 2022), galaxy sizes (Hardwick et al. 2022), and BH masses (Graham & Sahu 2023). Each COLIBRE resolution and AGN feedback model uses a separate calibration (see table 1 in Schaye et al. 2025).

(i) *Radiative cooling*: unlike most other hydrodynamical simulations that impose an effective equation of state to model the interstellar medium (ISM), COLIBRE explicitly tracks the chemical processes in the cold ISM, allowing gas to cool down to ≈ 10 K using the HYBRID-CHIMES model (Ploeckinger et al. 2025). HYBRID-CHIMES uses the CHIMES reaction network (Richings et al. 2014a,b) to compute radiative cooling and heating rates, treating hydrogen and helium in full non-equilibrium and metals in equilibrium with corrections for non-equilibrium free electrons.

(ii) *Dust*: the formation and evolution of dust grains is modelled directly on-the-fly, explicitly tracking three grain species and two grain sizes (Trayford et al. 2025). Grains are nucleated in the ISM by ejecta from asymptotic giant branch (AGB) and super-AGB (SAGB) stars (Dell’Agli et al. 2017), as well as by shocks from SNe (Zhukovska et al. 2008). In the ISM, grains grow by accretion (Hirashita & Yoshchinnikov 2014), primarily in molecular clouds, and are destroyed through sputtering (Tsai & Mathews 1995), astration, and SN shocks. Grain sizes evolve through coagulation and shattering (Aoyama et al. 2017). The dust model is coupled to the radiative cooling module, so that reactions and cooling rates account for dust presence and properties.

(iii) *Star formation*: star formation follows the local gravitational instability criterion from Nobels et al. (2024). SFRs of gas particles that satisfy this criterion are calculated using a Schmidt (1959) law with a fixed efficiency of gas-to-stars conversion per free-fall time of 1%. This model reproduces the Kennicutt–Schmidt relation (Kennicutt 1998) self-consistently at kiloparsec scales, without explicit tuning to that relation; including the observed scatter and its dependence on local properties such as stellar surface density and gas metallicity (Lagos et al. 2025a).

(iv) *Chemical enrichment*: yields have been updated with data from the literature to account for stellar mass from AGB stars, massive stars, Type Ia SNe and core collapse SNe (CCSNe). Abundances of key elements for radiative cooling, along with s-process elements (Ba, Sr) important in AGB stars and the r-process element (Eu) important in neutron star mergers, common-envelope jets SNe and collapsars, are tracked to enable a more realistic enrichment of the

ISM. Turbulent diffusion is included to capture small-scale mixing of metals and dust. These and other updates are described in Correa et al. (in prep.).

(v) *Stellar feedback*: early stellar feedback is implemented through stellar winds, radiation pressure, and H II regions (Benítez-Llambay et al. 2025). The model for CCSN feedback is based on Chaikin et al. (2023), with 90% of the energy injected thermally (by heating gas particles stochastically, driving galactic winds; Dalla Vecchia & Schaye 2012) and the remaining 10% injected kinetically (through low-velocity kicks, driving turbulence in the ISM). SN energy injections are distributed statistically isotropically around young stellar particles, following Chaikin et al. (2022).

(vi) *BH growth*: supermassive BHs are modelled, including seeding, growth via mergers and gas accretion, and repositioning to account for dynamical friction (Springel et al. 2005; Bahé et al. 2022). Gas accretion can exceed the Eddington rate by a factor of 100, but is regulated by radiative feedback in the thermal model, and by a combination of radiation, accretion disc winds, and jets in the hybrid model. In the hybrid case, mass loss between the outer accretion disc and the BH horizon is also included; while the accretion disc state (set by the BH accretion rate) determines distinct regimes with different accretion and feedback efficiencies. Further details are provided in Huško et al. (2025a) and § 2.3.

(vii) *AGN feedback*: the fiducial purely thermal model is based on Booth & Schaye (2009) (in which the BH injects energy thermally by increasing the temperature of gas particles) while several simulations adopt a hybrid model that combines a thermal component, modelling winds and radiation, with kinetic jets (in which the BH injects energy kinetically giving a velocity kick to gas particles). The jets are regulated by the BH spin, which also determines their directions and feedback efficiencies (Huško et al. 2025a). A more detailed description is provided in § 2.3.

2.3 Supermassive black hole growth & AGN feedback modelling

BH particles are seeded whenever a non-seeded FoF group exceeds a threshold mass of $M_{\text{FoF,seed}}$, at redshifts later than $z = 19$. The default value of $M_{\text{FoF,seed}}$ is $5 \times 10^{10} M_{\odot}$ for the m7 resolution and $1 \times 10^{10} M_{\odot}$ for m6 and m5 resolutions. If seeding is needed, the densest gas particle in the halo is converted into a collisionless BH particle with initial mass $M_{\text{BH}} = m_{\text{BH,seed}}$, typically of order $\sim 10^4 - 10^5 M_{\odot}$, following the ‘‘heavy seed’’ scenario in which BHs form via direct collapse of gas clouds or rapid mergers of stars/low-mass BHs (e.g. Regan & Volonteri 2024). The exact value depends on the simulation, as listed in table 1 of Schaye et al. (2025), since this is a free parameter during the calibration process. BH particles are repositioned according to the prescription by Bahé et al. (2022) to account for unresolved dynamical friction, ensuring the BH moves toward the galaxy’s potential centre.

Each BH particle has two distinct masses associated with it: a subgrid mass, M_{BH} , which governs BH-related physics; and a particle mass for gravity calculations, $m_{\text{BH,part}}$ (initially equal to the mass of the gas particle converted into the BH). After seeding, M_{BH} grows through both mergers and gas accretion from the BH particle mass, as long as $M_{\text{BH}} < m_{\text{BH,part}}$, reducing the particle mass value in accordance. When $M_{\text{BH}} > m_{\text{BH,part}}$, the BH particle instead grows by ‘‘nibbling’’ mass from neighbouring gas particles to conserve energy and mass (Bahé et al. 2022).

BH mergers occur when two BHs meet the following conditions: their separation is smaller than 3 times the gravitational softening length, the less massive BH lies within the smoothing length of the

more massive one, defined with the same kernel used in the SPH; and their relative velocity satisfies $\Delta v < \sqrt{2G(m_{\text{BH,part,1}} + m_{\text{BH,part,2}})/r}$, where $m_{\text{BH,part,1}}$ and $m_{\text{BH,part,2}}$ are the BH particle masses. When these conditions are met, the less massive BH particle is removed from the computational volume, and both its M_{BH} and $m_{\text{BH,part}}$ are added to the more massive BH. Gravitational-wave energy losses are also accounted for by assuming that the merger is of two non-spinning BHs with masses $M_{\text{BH,1}}$ and $M_{\text{BH,2}}$ and subtracted from the rest mass energy of the descendant for both subgrid and particle masses (Barausse et al. 2012).

Below, we explain how gas accretion and AGN feedback are modelled in the fiducial thermal and hybrid simulations.

2.3.1 Thermal feedback model (fiducial)

Gas accretion follows the Bondi–Hoyle–Lyttleton (BHL) rate (Bondi 1952; Hoyle & Lyttleton 1939):

$$\dot{M}_{\text{BHL}} = 4\pi G^2 \frac{\rho_g}{c_s^3} M_{\text{BH}}, \quad (1)$$

where G is the gravitational constant, ρ_g the gas density and c_s the sound speed of the ambient gas. Turbulence (f_{turb} term, Ruffert & Arnett 1994) and vorticity (f_{ang} term, Krumholz et al. 2005) corrections are introduced to account for aspherical inflows, photon trapping, and large-scale gas accretion (Izquierdo-Villalba et al. 2023):

$$\dot{M}_{\text{accr}} = \dot{M}_{\text{BHL}} \frac{f_{\text{turb}} f_{\text{ang}}}{(f_{\text{turb}}^2 + f_{\text{ang}}^2)^{1/2}}, \quad (2)$$

where the accretion rate may exceed the Eddington accretion rate ($\dot{M}_{\text{accr}} > \dot{M}_{\text{Edd}}$), defined as:

$$\dot{M}_{\text{Edd}} = \frac{4\pi G m_p M_{\text{BH}}}{\epsilon_r \sigma_T c}, \quad (3)$$

where m_p is the proton mass, σ_T is the Thomson cross-section, c is the speed of light, and ϵ_r is the radiative efficiency (Shakura & Sunyaev 1973). The BH accretion is then capped at $100 \times \dot{M}_{\text{Edd}}$.

The BH mass grows as:

$$\dot{M}_{\text{BH}} = (1 - \epsilon_r) \dot{M}_{\text{accr}}, \quad (4)$$

where \dot{M}_{accr} is the accretion rate onto the BH. The radiative efficiency is fixed at $\epsilon_r = 0.1$, representing the fraction of accreted mass radiated away as energy. The accretion is assumed to occur equally at accretion-disc and event-horizon scales.

While the BH is accreting at that rate, the associated feedback energy rate is $\dot{E}_{\text{AGN}} = \epsilon_f \epsilon_r \dot{M}_{\text{accr}} c^2$, where ϵ_f is the fraction of radiative energy that couples to the surrounding gas by heating it or driving a wind through radiation pressure. ϵ_f is calibrated to the $z = 0$ BH-to-stellar mass relation. This energy is stored in a reservoir until it exceeds a threshold, at which point it is inserted into the nearest gas particle. This approach ensures that the gas particle is heated to a high temperature, which helps avoid numerical overcooling. Energy injection is purely thermal (Booth & Schaye 2009), representing the effects of radiation (either direct or through radiatively-driven winds that shock on subgrid scales), with each event delivering:

$$\Delta E_{\text{AGN,thermal}} = \frac{m_g k_B \Delta T_{\text{AGN}}}{(\gamma - 1) \mu m_p}, \quad (5)$$

where $\gamma = 5/3$ is the adiabatic index, $\mu = 0.6$ is the mean molecular weight, and m_g is the gas particle mass. ΔT_{AGN} is the temperature increase applied to the gas particle, and it scales with BH mass as:

$$\Delta T_{\text{AGN}} = 10^9 \text{ K} \left(\frac{M_{\text{BH}}}{10^8 M_{\odot}} \right), \quad (6)$$

with $10^{6.5} \text{ K} < \Delta T_{\text{AGN}} < \Delta T_{\text{AGN,max}}$, where $\Delta T_{\text{AGN,max}} = 10^{9.5} \text{ K}$ for the m7 resolution runs and 10^{10} K for m6 and m5. The dependence of ΔT_{AGN} on BH mass is an important difference between COLIBRE and its predecessor, the EAGLE simulations (Schaye et al. 2015). This implementation enables better sampling of feedback in low-mass galaxies and allows for a gentler early phase of BH growth³.

2.3.2 Hybrid (thermal+jet) feedback model

The hybrid AGN feedback model (Huško et al. 2025a) combines thermal feedback, representing radiation and accretion winds, with kinetic feedback, representing jets. While the underlying BH physics is similar to that in the thermal model, the hybrid implementation introduces key differences in gas accretion and feedback prescriptions. Motivated by both observations and theoretical works, this model incorporates explicit BH spin evolution and accretion disc modelling.

First, BH spin is tracked, evolving through accretion, mergers, jet-induced spin-down, radiation torques, and Lense–Thirring precession. Spin tracking affects both jet orientation and all feedback efficiencies. The BH spin vector is defined as $\vec{a} = \vec{J}_{\text{BH}}c/(M_{\text{BH}}G)$, where \vec{J}_{BH} is the time-integrated BH angular momentum. Its magnitude $a = |\vec{a}|$ and sign indicate the degree of spin and whether accretion is prograde or retrograde with respect to a subgrid accretion disc. Seed BHs are initialised with a small spin ($a = 0.01$) and random orientation, effectively corresponding to non-rotating BHs. A full description of this model is given in Huško et al. (2025a).

Second, the accretion disc magnetisation or the magnetic flux around the BH event horizon is modelled, which modulates feedback efficiencies. The model assumes a magnetically arrested disc (MAD) state (Narayan et al. 2003), where magnetic fields are dynamically important and saturate at a value determined solely by the accretion rate and BH spin (Narayan et al. 2022).

BH growth follows a similar equation as equation (4), but extended to include the efficiencies of disc winds and jets:

$$\dot{M}_{\text{BH}} = (1 - \epsilon_r - \epsilon_{\text{wind}} - \epsilon_{\text{jet}}) \epsilon_{\text{accr}} \dot{M}_{\text{accr}}, \quad (7)$$

where \dot{M}_{accr} (equation 2) here refers to the accretion rate onto a subgrid accretion disc, rather than directly into the BH event horizon. ϵ_{wind} and ϵ_{jet} are the wind and jet efficiencies. ϵ_{jet} depends on the BH spin and the magnetisation of the disc (Tchekhovskoy et al. 2010), such that non-spinning BHs ($a = 0$) produce no jets ($\epsilon_{\text{jet}} = 0$). The parameter ϵ_{accr} , equal to 1 in the thermal model, accounts for mass lost to winds between the accretion disc and the BH horizon. BH accretion is also capped at $\dot{M}_{\text{accr}} = 100 \times \dot{M}_{\text{Edd}}$.

The accretion disc operates in three regimes representing different accretion disc properties, determined by $f_{\text{Edd}} = \dot{M}_{\text{accr}}/\dot{M}_{\text{Edd}}$ (BH spin-dependent via ϵ_r in the Eddington rate in equation 3). Both thermal and kinetic/jet feedback modes are active in all three regimes, which are:

- *Thick disc* ($f_{\text{Edd}} < 0.01$): geometrically thick and optically thin. Gas is hot and diffuse, leading to strong advection and negligible radiative efficiency ($\epsilon_r \lesssim 0.01$). Winds are present, with ϵ_{wind} depending on spin and magnetisation (Sadowski et al. 2014). Spinning BHs can also launch strong jets due to magnetic fields. ϵ_{accr} depends

³ Heating a single particle generates shock waves that propagate into the surrounding gas and expand due to thermal pressure. Although the feedback is injected isotropically, it typically results in bipolar outflows, as the energy preferentially escapes perpendicular to the disc along the path of least resistance (Nobels et al. 2022).

on f_{Edd} and the thick-disc radius, following Narayan & Yi (1995) (which contains a free parameter calibrated to the $z = 0$ AGN bolometric luminosity function).

- *Thin disc* ($0.01 < f_{\text{Edd}} < 1$): geometrically thin and optically thick, with a high radiative efficiency ϵ_r determined by BH spin via the innermost stable circular orbit. No disc winds are present ($\epsilon_{\text{wind}} = 0$). Jets form with power set by the accretion rate and magnetisation state. $\epsilon_{\text{accr}} = 1$, equivalent to the thermal AGN feedback model.

- *Slim disc* ($f_{\text{Edd}} > 1$): intermediate state between thick and thin discs. The disc is geometrically thick, but less than the thick disc, as well as advection-dominated and radiatively inefficient ($\epsilon_r \lesssim 0.01$, dropping as the accretion rate increases). Winds remove most of the inflowing mass, with ϵ_{wind} set by the accretion disc magnetisation (Ricarte et al. 2023). Slim discs produce luminous, powerful jets, though with lower efficiency than in the other regimes. $\epsilon_{\text{accr}} = 0.01$ is assumed, similar to the thick-disc values, which implies that the upper limit for the net accretion rate can not exceed the Eddington rate: $\epsilon_{\text{accr}} \max(\dot{M}_{\text{accr}}) = \epsilon_{\text{accr}} 100 \times \dot{M}_{\text{Edd}} = \dot{M}_{\text{Edd}}$.

The total energy available for feedback has a thermal and a kinetic contribution $\dot{E}_{\text{AGN}} = \dot{E}_{\text{AGN,thermal}} + \dot{E}_{\text{AGN,kinetic}}$, stored in separate energy reservoirs. The thermal energy generation and injection follows the fiducial model, but with additional contributions representing both radiation and winds: $\dot{E}_{\text{AGN,thermal}} = (\epsilon_r \epsilon_r + \epsilon_{\text{wind}}) \epsilon_{\text{accr}} \dot{M}_{\text{accr}} c^2$, where $\epsilon_r = 0$ for thick and slim discs, and calibrated for thin discs to reproduce the $z = 0$ BH-to-stellar-mass relation.

The kinetic feedback energy production is given by $\dot{E}_{\text{AGN}} = \epsilon_{\text{jet}} \epsilon_{\text{accr}} \dot{M}_{\text{accr}} c^2$. When the stored kinetic energy is sufficient, the closest particle is chosen on either side of the BH (defined by the two hemispheres along the BH spin vector). These two particles receive opposite velocity kicks, randomly oriented within 7.5° of the BH spin axis, releasing per feedback event an amount:

$$\Delta E_{\text{AGN,jet}} = 2 \times \frac{1}{2} m_g v_{\text{jet}}^2, \quad (8)$$

where the kick velocity per particle v_{jet} is:

$$v_{\text{jet}} = 10^{4.5} \text{ km s}^{-1} \sqrt{\frac{M_{\text{BH}}}{10^9 M_{\odot}}}, \quad (9)$$

with v_{jet} capped at $10^{2.5} \text{ km s}^{-1}$ and $10^{4.5} \text{ km s}^{-1}$ at the lower and higher end, respectively, where $10^{4.5} \text{ km s}^{-1}$ has been selected during the calibration process. The dependence on BH mass improves the sampling of AGN feedback⁴.

3 GALAXY PROPERTIES AND SAMPLE SELECTION

Galaxies in COLIBRE are embedded within subhaloes, and so determining galaxy properties is intimately linked to identifying subhaloes and quantitatively characterising their contents. Subhaloes in COLIBRE are identified with HBT-HERONS, which tracks particles across timesteps. Galaxy properties are then measured using SOAP in different apertures centred on the most bound particle. Throughout this paper, we adopt a fiducial 50 pkpc spherical aperture to analyse high- z MQGs, considering only particles bound to the subhalo, as in Schaye et al. (2025). Unless otherwise stated, this aperture is used. We also test other aperture radii (e.g., 10 pkpc and 30 pkpc) and find that the measured properties converge even for the smallest aperture (Appendix A). This reflects the compact nature of MQGs at high

⁴ The velocity kick generates shocks that drive jets and inflate hot gas bubbles on Mpc scales (see fig. 1 in Huško et al. 2024).

redshift (see § 4.5) and confirms that the galaxy properties we use are robust to the choice of aperture. For reference, *JWST* observations typically employ apertures of ≈ 10 ckpc to measure colours for MQGs (see section 2.3 in Lagos et al. 2025b). Below, we summarise the main galaxy properties and definitions used throughout the paper.

- *Stellar mass (M_\star)*: computed as the sum of all stellar particles.
- *SFR*: calculated as the sum of the SFRs of gas particles flagged as star-forming (i.e., locally gravitationally unstable; Nobels et al. 2024). We adopt this measure of instantaneous SFR, but we verify that using 10 Myr or 100 Myr averages, more comparable to observational tracers such as H α and UV luminosities (Kennicutt & Evans 2012), does not significantly alter the results (see Appendix A).
- *Dust mass (M_{dust})*: the total dust mass in gas particles (the sum over the 6 species described in § 2).
- *Molecular hydrogen mass (M_{H_2})*: the sum of H_2 mass in gas particles.
- *Stellar half-mass radius (r_\star)*: the radius enclosing half of the stellar mass, measured in projected 50 pkpc apertures along the x , y , and z -axes, considering bound particles only. The final value is the average of the three projections to mimic the random viewing orientation of observed galaxies.
- *BH mass (M_{BH}) and properties*: defined by the most massive BH particle within the fiducial spherical 50 pkpc aperture, considering only particles bound to the subhalo, as used in Huško et al. (2025a).
- *Gas mass in/outflow rate ($\dot{M}_{\text{in/outflow}, fR_{200c}}$)*: the rate at which gas mass crosses into/out of spherical shells centred at $fR_{200c} = 0.1R_{200c}$, $0.3R_{200c}$ or R_{200c} , with a shell width of $0.1 \times fR_{200c}$. Here, R_{200c} is the radius within which the mean density equals 200 times the critical density of the Universe. Gas particles are further classified by temperature: cold ($T_{\text{gas}} < 10^3$ K), cool ($10^3 \text{ K} < T_{\text{gas}} < 10^5$ K), warm ($10^5 \text{ K} < T_{\text{gas}} < 10^7$ K), and hot ($T_{\text{gas}} > 10^7$ K).
- *Halo mass (M_{halo})*: defined as the total mass of the group they belong to, as identified by the 3D FoF algorithm.

3.1 Selecting the high- z MQG sample

Multiple definitions for MQGs at high- z exist in the literature. We adopt the following criteria, focusing on systems at $z \geq 2$ where there appears to be various degrees of tension with galaxy formation models and simulations (Lagos et al. 2025b).

- Massive criterion: $M_\star > 10^{10} \text{ M}_\odot$.
- Quenched criterion: $\text{sSFR} < 0.2/t_{\text{age}}$, where the specific star formation rate is defined as $\text{sSFR} = \text{SFR}/M_\star$ and t_{age} is the age of the Universe at the redshift of selection. Galaxies above this threshold are classified as star-forming.

The massive threshold is defined following common practice. For the definition of quiescence, several approaches exist, including colour–colour cuts, fixed specific sSFR thresholds, or redshift-dependent sSFR thresholds. We opt for a redshift- and mass-dependent cut following Franx et al. (2008), since relevant timescales (e.g. gravitational or cooling times) scale with the Hubble time and gas density; while colour-based methods can be contaminated by obscured star formation or emission lines (Schreiber et al. 2018) and may even miss quiescent galaxies that fall outside the traditional strict criteria (Merlin et al. 2018). Table 1 shows the number of MQGs identified at $z = 3$ using this definition. A comparison of alternative criteria is presented in Appendix A.

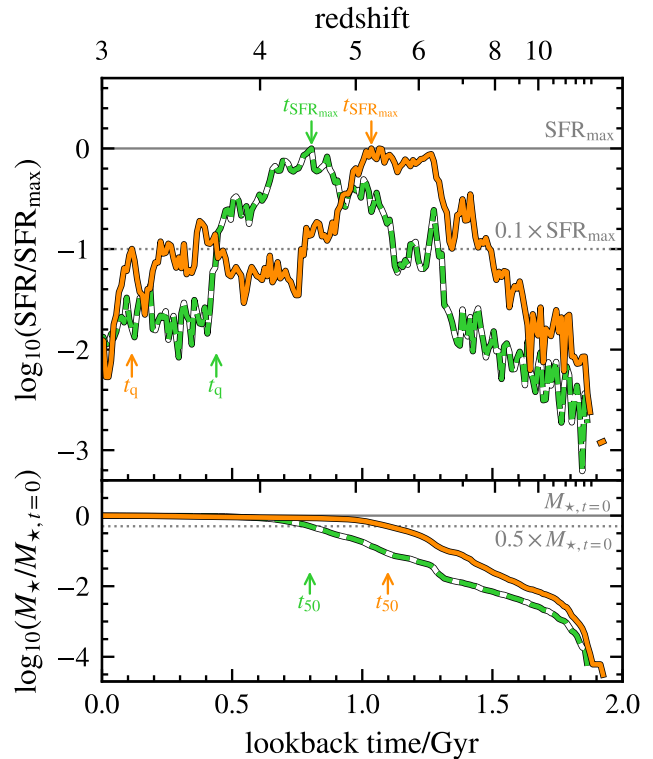


Figure 1. *Top panel*: normalised SFHs ($\text{SFR}/\text{SFR}_{\text{max}}$ versus lookback time, with redshift indicated by the top x -axis) of two example galaxies identified to be massive and quenched at $z = 3$ in L200m6. The horizontal solid line corresponds to the peak SFR value, SFR_{max} , while the dotted line shows the $0.1 \times \text{SFR}_{\text{max}}$ threshold used to define the quenching timescale, t_q . Arrows indicate t_q for each galaxy, defined as the latest time the galaxy’s SFR drops below this threshold; as well as the SFR peak time, $t_{\text{SFR}_{\text{max}}}$. The green curve represents a galaxy that, once it has crossed the threshold indicated by the dotted line, never rises above it again. The orange curve represents a galaxy that experiences several star formation episodes above the threshold after its SFR peak. *Bottom panel*: normalised stellar mass assembly histories ($M_\star/M_{\star,t=0}$ versus lookback time, with redshift indicated by the top x -axis) for the same galaxies. The horizontal solid line shows the maximum stellar mass value, $M_{\star,t=0}$; while the dotted line shows the $0.5 \times M_{\star,t=0}$ threshold used to define the formation timescale, t_{50} . Arrows indicate t_{50} .

3.2 Computing star formation histories

Star formation histories (SFHs) are computed from stellar particles gravitationally bound to each galaxy within the fiducial 50 pkpc spherical aperture, using their stellar ages and stellar masses at birth to construct a mass-weighted histogram of formation times. It is important to note that this method does not distinguish between in-situ (stars formed within the galaxy) and ex-situ (stars formed outside the galaxy’s main progenitor) star formation. Consequently, star formation bursts could reflect the peak formation of an accreted ex-satellite rather than intrinsic activity in the galaxy itself.

We adopt a bin size of 10 Myr to sample the SFHs, which gives reasonable results, being much longer than the simulation time step and comparable to observational studies capable of probing SFR variations on similar short timescales via spectral features (Kennicutt & Evans 2012). We also test a 20 Myr bin size, which yields similar overall results but smooths out variability, making it less effective at capturing short-timescale features in the SFHs.

Observationally, different SFH features are extracted to characterise key evolutionary events in a galaxy, rather than comparing

their overall shapes, which have less quantitative meaning. To enable meaningful comparisons with observations, we therefore focus on a subset of these features, measured in lookback time from the epoch of selection, following common practices in the literature:

- The quenching timescale, t_q , indicates when a galaxy effectively ceases star formation. We define t_q as the lookback time from the selection redshift (not from $z = 0$) when the SFR last dropped below 10% of its peak value: $\text{SFR}(t_q) = 0.1 \times \text{SFR}_{\text{max}}$. Our approach is inspired by [Nanayakkara et al. \(2025\)](#), although they define quenching as the longest continuous period below this threshold after the peak.

The top panel of Fig. 1 shows a single-starburst SFH of a $z = 3$ MQG (green line), where the SFR remains below the threshold once crossed. For MQGs with multiple starburst episodes after the peak (orange line), we adopt the last time the galaxy crosses it, reflecting when it finally transitions to quiescence before the selection snapshot. The fraction of galaxies with multiple starbursts after the peak is dominant in general with ≈ 0.76 at $z = 2$, ≈ 0.64 at $z = 3$, ≈ 0.46 at $z = 4$, ≈ 0.09 at $z = 5$, and ≈ 0.50 at $z = 6$ for L200m6. Multiple episodes of SF, before or after the peak could be connected to ‘mini-quenching’ discussed in the literature ([Strait et al. 2023](#); [Loosher et al. 2024](#); [Baker et al. 2025d](#)).

- The formation timescale describes how rapidly a galaxy assembles its stellar mass. It can be defined in several ways: for example, the time at which 50% (t_{50}) or 90% (t_{90}) of the stellar mass has formed, or the interval $t_{90} - t_{50}$. We adopt t_{50} as the primary measure of formation time, which we compute in lookback time from the selection redshift as follows. Using the SFH, we calculate the cumulative stellar mass by integrating over time bins and estimate when its mass first exceeds 50% of its integrated mass at $z = 0$ ($0.5 \times M_{\star, t=0}$). This is shown in the bottom panel of Fig. 1. Note that $M_{\star, t=0}$ ignores stellar mass loss and may therefore differ from the actual galaxy stellar mass M_{\star} .

3.3 Kinematic tracer v_{\star}/σ_{\star} definition

To characterise the kinematics of a galaxy, we focus on the stellar component and measure v_{\star}/σ_{\star} as a tracer. This approach has recently been applied to massive quenched systems ([Pascalau et al. 2025](#); [Slob et al. 2025](#); [Forrest et al. 2025](#)). Here, v_{\star} represents the stellar rotational velocity, indicating the galaxy’s rotational support, while σ_{\star} quantifies the stellar velocity dispersion, indicating the random motion contribution. This measure differs from the classical spin parameter λ_r , although the two can be converted using the relation in [Cappellari \(2016\)](#).

To compute these quantities, we must first define a reference frame: 1. measure the galactic centre, and 2. rotate the galaxy to align it with the stellar angular momentum vector. We define our centre as the stellar centre of mass and its corresponding velocity in a 50 pkpc spherical aperture, using only bound particles. Other options are: (i) the stellar centre of mass and its velocity within other apertures such as 10 or 30 pkpc, (ii) the position and velocity of the most massive BH particle within a 50 pkpc spherical aperture, considering only bound particles, or (iii) the most bound particle of the subhalo (subhalo centre) and stellar centre of mass velocity within 10 pkpc. We find that our approach gives more stable results, minimising the mean position and velocity within our fiducial aperture. Secondly, we rotate the galaxy so that the z -axis aligns with the stellar angular momentum vector of the 10 pkpc core.

Once aligned, we compute the stellar kinematics using cylindrical coordinates for each bound particle (v_r, v_{ϕ}, v_z) in the fiducial 50 pkpc aperture centred on the most bound particle. The rotational

velocity is given by the azimuthal component, v_{ϕ} , and the total galaxy’s stellar rotational velocity is computed as the mass-weighted root mean square (RMS):

$$v_{\star} = \sqrt{\frac{\sum_{i \in R} m_i v_{\phi, i}^2}{\sum_{i \in R} m_i}}. \quad (10)$$

The perpendicular component to the plane traces the vertical velocity dispersion in the disc, v_z , and its final value is similarly computed as the mass-weighted RMS:

$$\sigma_{\star} = \sqrt{\frac{\sum_{i \in R} m_i v_{z, i}^2}{\sum_{i \in R} m_i}}. \quad (11)$$

We caution the reader that our v_{\star}/σ_{\star} measurements ([§ 4.5.1](#)) are not quantitatively comparable to observations because of limitations such as beam smearing ([Harborne et al. 2019](#)) and projection effects, which make our values effectively upper limits. Observations measure line-of-sight velocity and velocity dispersion (which differ from our definition) and are sensitive to galaxy orientation, although inclination corrections are applied. Observations also typically measure v_{\star}/σ_{\star} within the half-light radius, whereas we use all stellar particles within the aperture.

3.4 Environmental tracer $\delta_{\sigma_{\text{subh, rel}}(< R)}$ definition

We also aim to characterise the environment of the MQGs on different scales, not only through their halo masses. Several approaches exist for this purpose; however, we follow recent works in the field, which have employed the density contrast to quantify environment ([Kimmig et al. 2025](#); [Chittenden et al. 2025](#); [Weller et al. 2025](#)). We use the subhalo density contrast as:

$$\delta_{\text{subh}}(< R) = \frac{\rho_{\text{subh}}(< R) - \bar{\rho}_{\text{subh}}}{\bar{\rho}_{\text{subh}}}, \quad (12)$$

where $\rho_{\text{subh}}(< R)$ is the subhalo density within a real-space sphere of radius R while $\bar{\rho}_{\text{subh}}$ is the mean subhalo density of the Universe. We compute $\rho_{\text{subh}}(< R) = \sum_{i \in R} M_{\text{subhalo}, i}/V_R$, where $M_{\text{subhalo}, i}$ is the total subhalo mass (all bound particles) of each neighbouring galaxy whose galaxy centre, as defined by the most bound particle, resides within the sphere of radius R . V_R is the volume of the sphere. The second variable is computed as $\bar{\rho}_{\text{subh}} = M_{\text{bound}}/V_{\text{box}}$, where $M_{\text{bound}} = \sum_{i \in \text{box}} M_{\text{subhalo}, i}$ is the mass bound to any galaxy in terms of subhalo hierarchy in the whole simulation box and V_{box} the simulation volume.

The density contrast characterises the environment of each galaxy. To compare the environments of MQGs and massive star-forming galaxies (hereafter MSFGs), we also examine the distributions of their subhalo density contrasts ([Kimmig et al. 2025](#)). For this purpose, we use the deviation from the mean subhalo density contrast:

$$\delta_{\sigma_{\text{subh, rel}}(< R)} = \frac{\delta_{\text{subh}}(< R) - \bar{\delta}_{\text{subh}}(< R)}{\sigma_{\delta_{\text{subh}}}(< R)}, \quad (13)$$

where $\bar{\delta}_{\text{subh}}(< R)$ is the mean subhalo density contrast for the distribution of both MQGs and MSFGs, while $\sigma_{\delta_{\text{subh}}}(< R)$ is the standard deviation of that distribution. This metric allows us to quantify the relative subhalo density contrast of each galaxy with respect to the overall population of massive galaxies. We choose three different apertures $R = 0.3, 1.0, 3.0 \text{ cMpc}$ to capture the environment in a range of local to larger scales in the cosmic web.

4 THE DEMOGRAPHICS OF MQGS IN COLIBRE

We present predictions from the COLIBRE model for MQGs (as defined in § 3.1) at high-redshift ($z \geq 2$). Our analysis considers a broad set of properties, including those that can be constrained observationally and others that remain largely theoretical due to current observational limitations.

4.1 Number densities of MQGs

We begin by analysing the evolution of the number density (i.e. number of objects per unit comoving volume) of MQGs. Lagos et al. (2025b) have shown that galaxy formation and evolution models face challenges in consistently reproducing the number density of MQGs inferred from *JWST* observations. Chaikin et al. (2025b) perform a COLIBRE analysis using only two simulations with the thermal AGN feedback model; here, we extend this study.

4.1.1 Results

The top panel of Fig. 2 presents results from the various COLIBRE simulations listed in Table 1; these differ in volume, resolution, and AGN feedback implementation. Number densities are computed at intervals of 0.5 in redshift over $z = 2 - 8$. When no galaxies are identified as MQGs at a given redshift, the corresponding redshift bin is omitted; thus, some lines end at $z < 8$. These predictions are compared with the latest *JWST* observational constraints.

Fig. 2 reveals that there is significant variation among the different simulations. At fixed colour, the dashed and solid lines correspond to different simulated volumes at fixed mass resolution. Larger volumes capture rarer galaxies at the highest redshifts, reducing cosmic variance (particularly important for these systems, e.g. Lim et al. 2025) and improving number statistics (notably at $z \gtrsim 4$ for the m6 runs and at $z \gtrsim 6$ for m7 runs), as well as including longer-wavelength fluctuations that give rise to the largest overdensities capable of forming these galaxies. However, the bump seen in L100m6 around $z \approx 5$ is not solely due to Poisson noise but reflects a pronounced overdensity in its ICs traced at high redshift (final part of appendix A1 in Chaikin et al. 2025b).

Resolution effects are also apparent. Darker (lighter) lines represent lower (higher) mass resolution simulations. There is a systematic offset between the different resolution simulations, indicating that galaxies in higher-resolution simulations are less quenched. Two factors contribute to this trend: (1) at higher resolution, gas particles trace smaller effective volumes, producing denser gas around BHs, and so stronger feedback is required to eject or heat it; (2) AGN feedback becomes less bursty at higher resolution, due to the resolution-dependent nature of the feedback prescriptions in equations (5) and (8). These effects make AGN feedback less effective at higher resolution. Differences in BH seed masses may also play a role, since higher-resolution simulations use lower seed masses, delaying BH growth and the onset of AGN feedback.

The dotted lines represent simulations that include hybrid AGN feedback, thermal plus jet feedback, instead of purely thermal AGN feedback. This hybrid model produces significantly less quenching. In Appendix G, we show that the difference arises because the hybrid model features BHs that grow more slowly in the early Universe compared to the fiducial, purely thermal AGN feedback model. We can see this by considering the ratio, M_{BH}/M_{\star} . The medians are comparable in the thermal L200m7 and hybrid L200m7h simulations at $z = 2$ (~ 0.67); however, at $z = 5$, the medians are 0.70 (thermal) versus 0.64 (hybrid), and 0.70 versus 0.60 at $z = 8$. Moreover, jet

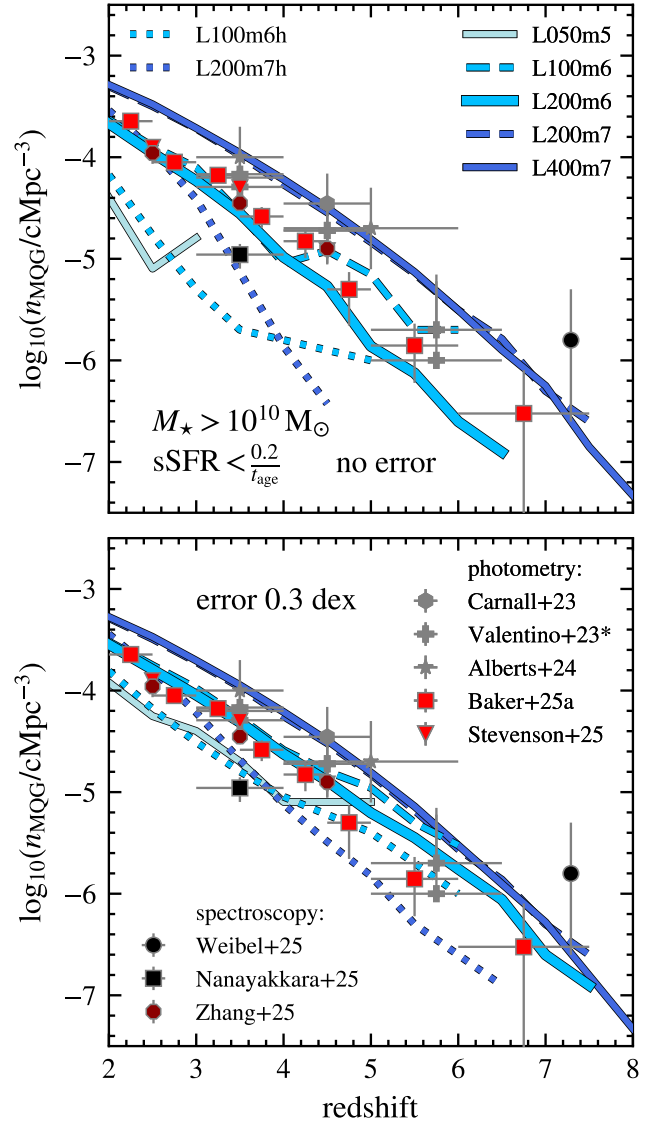


Figure 2. Comoving number density of MQGs, defined by $M_{\star} > 10^{10}$ and $\text{sSFR} < 0.2/t_{\text{age}}$, as a function of redshift. Lines represent predictions from various COLIBRE boxes (spanning different volumes, resolutions, and AGN feedback models) in Table 1, with the selection at $2 \leq z \leq 8$. These are compared with the latest *JWST* observational estimates: black (smaller area) and dark red (larger area) points show spectroscopic measurements, while grey (smaller area) and red (larger area) points correspond to photometric measurements. Observational data are taken from Carnall et al. (2023a); Valentino et al. (2023); Alberts et al. (2024); Nanayakkara et al. (2025); Weibel et al. (2025); Baker et al. (2025a); Zhang et al. (2025); Stevenson et al. (2025). Top panel: predicted simulation values. Bottom panel: M_{\star} and SFR values in the simulations are convolved independently with a Gaussian distribution (mean 0, standard deviation 0.3 dex) representing a reasonable error budget for these quantities.

feedback appears to take longer to quench galaxies than thermal feedback. At fixed stellar mass and for $z \lesssim 3$, the same cumulative injected BH energy leads to a higher fraction of quenched systems in the thermal feedback model (see Fig. G1). These effects do not appear to depend on mass resolution; the same trend is evident in both the m7 and m6 runs, with the pronounced overdensity visible around $z \approx 5$ in L100m6h as well. By $z < 2$, however, hybrid feedback becomes more efficient at quenching because the weaker

early feedback allows galaxies to build more stellar mass, which must then converge by $z = 0$ (see fig. 13 in Chaikin et al. 2025b).

Ultimately, runs at different resolutions, and within the same resolution, runs with different AGN feedback models (thermal or hybrid), were independently tuned to reproduce $z = 0$ observations. Each run should therefore be seen as a distinct model. We remind the reader that all of them have been calibrated to consistently reproduce the $z = 0$ SMF, the galaxy size–mass relation, and the galaxy BH–mass relation (figs. 12, 14 and 15 in Schaye et al. 2025).

Compared with observations, the top panel of Fig. 2 shows that the highest-resolution m5 and m6 COLIBRE thermal AGN feedback runs, as well as the hybrid AGN feedback runs, underpredict the high number densities inferred from *JWST*. However, the tension is significantly alleviated if we consider potential errors associated with the derivation of stellar mass and SFR of galaxies. Bellstedt & Robotham (2025) showed that the many decisions behind the derivation of stellar masses and SFRs (i.e. adopted functional form of the star formation history and metallicity histories; the choice of stellar population models; the IMF; to mention a few; see Conroy 2013, for a review) can lead to differences in the derived stellar masses and SFRs of 0.1 – 0.2 dex and ≈ 0.2 dex, respectively, in the $z \approx 0$ spectroscopic GAMA survey. We refer the reader to other works for further discussion of these uncertainties (e.g. Conroy et al. 2009; Robotham et al. 2020; Cochrane et al. 2025; Jones et al. 2025). The uncertainties reported by Bellstedt & Robotham (2025) could be seen as lower limits for the uncertainties one would expect for high- z galaxies with potentially more bursty SFHs, poorer wavelength coverage and potentially with photometric redshifts only. It is thus natural to expect uncertainties to be even larger at high- z .

To exemplify the impact such an error budget could have, we show in the lower panel of Fig. 2 the number densities after convolving the stellar masses and SFRs of COLIBRE galaxies with a Gaussian centred at 0 with a width of $\sigma = 0.3$ dex. This is a conservative case, in which there are no systematic shifts in the recovered quantities (in a population sense), and instead the individual uncertainties coming from SED fitting, photometric redshifts, etc, contribute to broadening the scatter of the recovered quantities, consistent with the findings of Bellstedt & Robotham (2025) at $z = 0$. We carry out the error convolution for stellar masses and SFRs in an independent manner, which is a simplification, as errors could potentially be correlated. In Appendix B, we explore the impact of adopting different values for the standard deviation (Fig. B1). This procedure produces perturbed values (M_\star^{conv} and SFR^{conv}), to which we then apply the MQG selection (§ 3.1). To reduce stochastic noise introduced by the convolution, the procedure is repeated 100 times, and the median of the resulting measurements is taken. This error convolution is just for reference, and the aim is to make the visual argument that quantifying uncertainties in the observational estimates is crucial to isolate the level of tension between models and the observations. For a more detailed analysis of the impact of errors on the quenched fraction, SMF and number densities of galaxies, we refer the reader to appendix D in Chaikin et al. (2025b).

4.1.2 Comparison with observations

For the remainder of § 4, we primarily focus on the fiducial L200m6 simulation. This run provides a sufficiently large volume to contain dozens of MQGs while also resolving their internal structure more reliably (see § 4.5 and Appendix E). This run also performs better in reproducing the observed number density evolution after we consider errors. We additionally include results from the L400m7 simulation where relevant. We do not show results from the L200m7h hybrid

run henceforth, but confirmed that the results look broadly similar, highlighting the places where this may not be the case.

In Fig. 3, we show the L200m6 predictions (including Gaussian-distributed uncertainties in the stellar masses and SFRs of width 0.3 dex) alongside the same observational data shown in Fig. 2. We have already discussed observational uncertainties arising from some of the choices behind SED modelling. However, there are additional, important caveats and biases that affect observationally derived number densities that are worth discussing in more detail.

- *Selection criteria:* The observations by Carnall et al. (2023a), Baker et al. (2025a) and Stevenson et al. (2025) are most directly comparable to our data; they adopt the same criteria described in § 3.1 ($M_\star > 10^{10} M_\odot$ and $\text{sSFR} < 0.2/t_{\text{age}}$). Baker et al. (2025a) also apply a colour–colour selection to clean their sample. However, other studies use different definitions. For example, Alberts et al. (2024) apply a lower stellar mass cut ($M_\star \geq 10^{9.5} M_\odot$), while Valentino et al. (2023)⁵ use a UV or NUVUVJ colour–colour selection in addition to $M_\star \geq 10^{9.5} M_\odot$. Similarly, Nanayakkara et al. (2025) select galaxies via UVJ colours but with $M_\star > 10^{10.5} M_\odot$. Colour–colour selections have been reported to suffer from contamination of obscured star formation or strong emission lines (Schreiber et al. 2018; Zhang et al. 2025) and can also miss significant numbers of quiescent galaxies that fall outside the traditional criteria (Merlin et al. 2018), motivating the development of alternative methods (e.g. Long et al. 2024). Finally, Weibel et al. (2025) and Zhang et al. (2025) report galaxies with $\text{sSFR} < 10^{-10} \text{yr}^{-1}$. The former work for a single $M_\star = 10^{10.23} M_\odot$ galaxy (hence the large error) and at higher redshift, where our threshold $\text{sSFR} < 0.2/t_{\text{age}} \approx 3 \times 10^{-10}$ diverges more, biasing simulation results higher; the latter for $M_\star > 10^{10.3} M_\odot$ ($m_{\text{F444W}} < 24$ in table 1, corresponding to a complete sample above that stellar mass).

A more detailed comparison, matching the exact observational selection criteria used to compute number densities, is left for future work. For reference, Chaikin et al. (2025b) present COLIBRE results with different M_\star cuts ($> 10^{10} M_\odot$, $> 10^{10.5} M_\odot$ and $> 10^{11} M_\odot$), although they adopt an $\text{sSFR} < 10^{-10} \text{yr}^{-1}$ criterion for quiescence.

- *Photometric versus spectroscopic measurements:* Only two studies provide a fully robust spectroscopic sample (Nanayakkara et al. 2025; Zhang et al. 2025), plus the Weibel et al. (2025) galaxy, which is spectroscopically confirmed as well. Most other works rely on photometric redshifts, which can misidentify MQGs due to dust obscuration, old stellar ages, AGN activity, or reduced star formation (Forrest et al. 2024; Zhang et al. 2025). Some studies account for errors in the photometric (Valentino et al. 2023; Alberts et al. 2024) or spectroscopic redshifts (Nanayakkara et al. 2025; Zhang et al. 2025), or apply contamination corrections (Stevenson et al. 2025), whereas others consider only Poisson errors.

- *Area coverage:* Sample size and coverage statistics also play a role; some datasets cover relatively small areas of the sky, potentially targeting over- or under-dense regions. This is particularly true for the photometric samples from Carnall et al. (2023a); Valentino et al. (2023); Alberts et al. (2024) (all in overdense regions, with at most dozens of objects), as well as the spectroscopic samples from Weibel et al. (2025) (a single galaxy in a pronounced overdensity) and Nanayakkara et al. (2025) (covering a smaller region). Some works account for cosmic variance in their error bars (Baker et al. 2025a; Zhang et al. 2025), which explains the larger uncertainties.

⁵ We homogenise the Valentino et al. (2023) results by combining $10^{9.5} \leq M_\star/M_\odot < 10^{10.6}$ and $M_\star > 10^{10.6} M_\odot$.

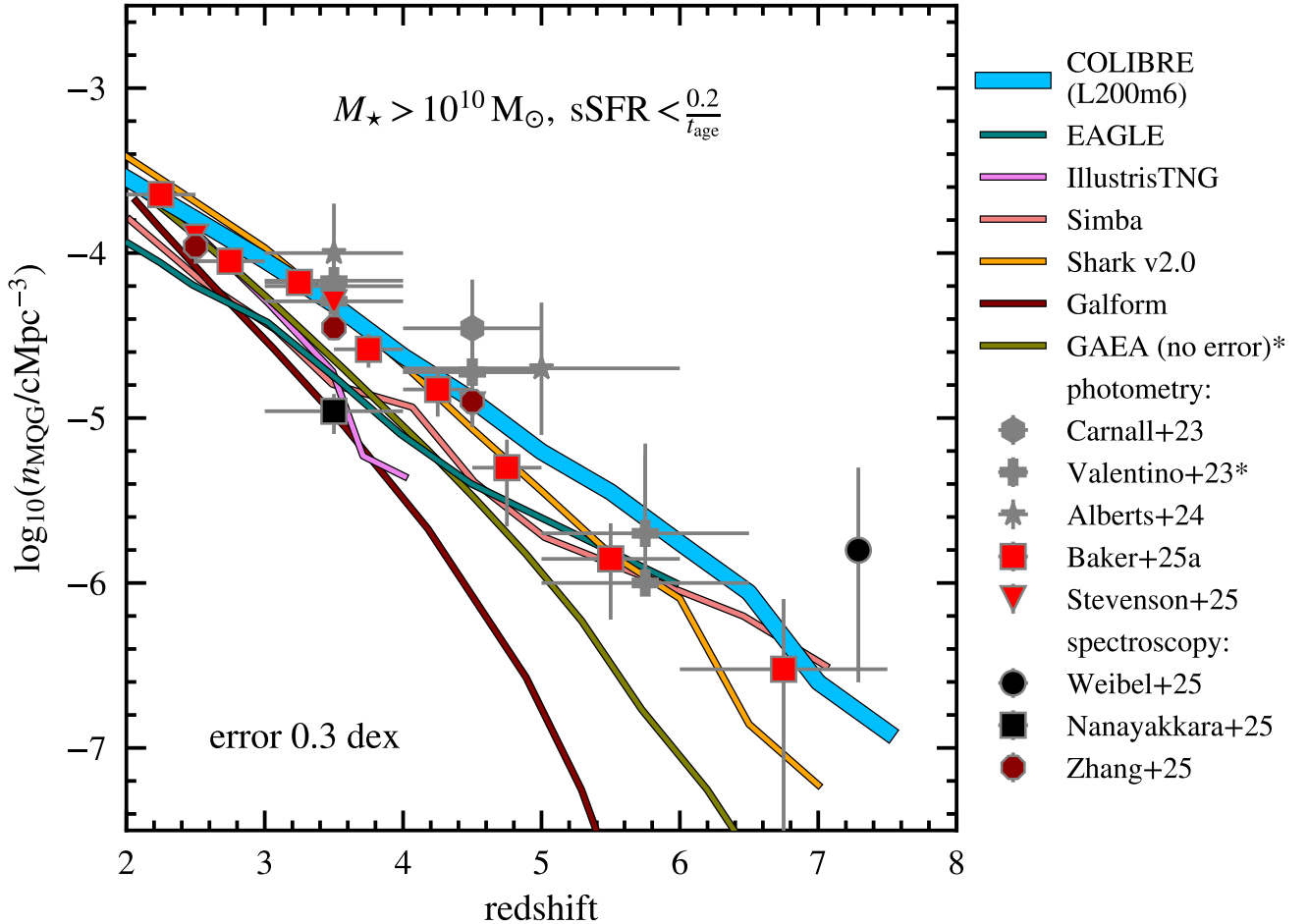


Figure 3. Comoving number density of MQGs, defined by $M_\star > 10^{10} M_\odot$ and $\text{sSFR} < 0.2/t_{\text{age}}$, as a function of redshift. Light-blue line shows predictions from our fiducial L200m6 COLIBRE simulation, with the selection at $2 \leq z \leq 8$, compared to results from other galaxy formation and evolution models in the literature (GAEA defines quenching using a fixed cut of $\text{sSFR} = 10^{-10} \text{yr}^{-1}$). For all simulation results (except GAEA), M_\star and SFR values in the simulations are convolved independently with a Gaussian distribution (mean 0, standard deviation 0.3 dex) representing a reasonable error budget for these quantities. These are compared with the latest *JWST* observational estimates: black (smaller area) and dark red (larger area) points show spectroscopic measurements, while grey (smaller area) and red (larger area) points correspond to photometric measurements. Observational data are taken from Carnall et al. (2023a); Valentino et al. (2023); Alberts et al. (2024); Nanayakkara et al. (2025); Weibel et al. (2025); Baker et al. (2025a); Zhang et al. (2025); Stevenson et al. (2025).

- *Choice of SFR timescale:* The SFR timescale deduced from modelling of the SED can depend on the photometric bands or spectral features used to infer the galaxy's SFR (Kennicutt & Evans 2012). Some photometric studies adopt a 100 Myr timescale (e.g. Alberts et al. 2024; Baker et al. 2025a), while others use shorter timescales of around 10 Myr (e.g. Zhang et al. 2025). We tested the impact of varying these timescales and found that the results remain largely unchanged (see Appendix A). In COLIBRE, this shows that the SFHs of MQGs are not extremely bursty on average over the past 100 Myr. The dominant MQG population with multiple starbursts (§ 3.2) appears to undergo these episodes earlier in time, or they are not strong enough to alter the averaged values.

- *Wavelength coverage:* The wavelength range used in SED fitting is critical for mitigating dust contamination. E.g. UV–NIR photometry alone is insufficient to constrain AGN contributions (Chang et al. 2025). The incorporation of the mid-IR (MIR) data, such as *JWST*/MIRI observations (e.g. Wang et al. 2025b), has proven to provide stronger constraints. Valentino et al. (2023); Weibel et al. (2025) and Baker et al. (2025a) include them when available.

Taking all these factors into account, larger, more robust samples provide more consistent and reliable results. In Fig. 3, these are some photometric data (e.g. Baker et al. 2025a; Stevenson et al. 2025) (light red) and spectroscopic data with incompleteness corrections (e.g. Zhang et al. 2025) (dark red). These more robust datasets show better agreement with each other, and the simulations are no longer as far from the observed values, reducing the tension highlighted in previous works (e.g. Carnall et al. 2023a; Valentino et al. 2023). The observational landscape is evolving rapidly, especially with the increase in sample sizes and a better understanding of the systematic effects associated with different selection criteria, as demonstrated by the recent works of Yang et al. (2025) and Shuntov et al. (2025).

We conclude that COLIBRE predictions are broadly consistent with the most recent and robust *JWST* measurements (red and dark red points), particularly after invoking an error budget of 0.3 dex in stellar masses and SFRs.

4.1.3 Comparison with other galaxy formation models

We also place our COLIBRE results in the context of other recent simulation predictions in Fig. 3. Here we compare our fiducial run with hydrodynamical galaxy formation simulations: EAGLE (Schaye et al. 2015), ILLUSTRIS-TNG (Pillepich et al. 2018) and SIMBA (Davé et al. 2019); and semi-analytic models: SHARK v2.0 (Lagos et al. 2024), GALFORM (Lacey et al. 2016), and GAEA (De Lucia et al. 2024). Except for GAEA, all models adopt the same quenching definition (§ 3.1) and include Gaussian-distributed errors in their measurements, although the convolution is not repeated 100 times as for the COLIBRE results. In contrast, GAEA defines quenching using a fixed threshold of $\text{sSFR} = 10^{-10} \text{ yr}^{-1}$.

For EAGLE, we use the L100N1504 simulation with $L = 100 \text{ cMpc}$, $m_g \sim 10^6 M_\odot$ and $m_{\text{DM}} \sim 10^7 M_\odot$; for ILLUSTRIS-TNG, the TNG100 run with $L \approx 111 \text{ cMpc}$, $m_g \sim 10^6 M_\odot$ for the initial gas cell mass and $m_{\text{DM}} \sim 10^7 M_\odot$; while for SIMBA, the m1000n1024 run with $L \approx 147 \text{ cMpc}$, $m_g \sim 10^7 M_\odot$ per gas element mass and $m_{\text{DM}} \sim 10^8 M_\odot$. In the case of the SAMs, SHARK v2.0 has been run on a $L = 800 \text{ cMpc}$ box with $m_{\text{DM}} \sim 10^8 M_\odot$; GALFORM on a $L \approx 710 \text{ cMpc}$ box with $m_{\text{DM}} \sim 10^9 M_\odot$; while GALFORM on a $L \approx 685 \text{ cMpc}$ per side with $m_{\text{DM}} \sim 10^9 M_\odot$. The larger volumes of the SAMs provide better number statistics, reducing the impact of cosmic variance, probing lower number densities (as seen in Fig. 3) and capturing more extreme overdensities.

COLIBRE and SHARK v2.0 tend to predict higher number densities compared to the other models over the redshift range, with COLIBRE about 0.5 dex higher for $z > 5$. In COLIBRE, Chaikin et al. (2025b) suggest that this arises from two factors: the explicit modelling of the cold gas phase and the allowance for BH accretion above the Eddington limit. Resolving the cold, dense gas enables BHs to accrete more rapidly, triggering stronger AGN feedback and earlier quenching. Since the BHL accretion rate is directly proportional to the local gas density (equation 1), higher densities lead to higher accretion rates. Super-Eddington accretion, common at these high redshifts (Huško et al. 2025b), further accelerates BH growth, reinforcing this effect.

The other models underpredict the observations: EAGLE and SIMBA at $z \lesssim 5$, while GALFORM and GAEA at $z \gtrsim 3$. These discrepancies reflect differences in subgrid physics, especially AGN feedback, which plays a central role in regulating the quenching of massive galaxies (Lagos et al. 2025b). Other simulations, not included in Fig. 3, predict higher number densities without accounting for observational uncertainties: for example, MAGNETICUM (Kimmig et al. 2025) and THESAN (Chittenden et al. 2025). However, we note that MAGNETICUM has only been run down to $z \approx 2$, where it overpredicts the number densities (Lagos et al. 2025b); while THESAN focuses on $z \geq 5.5$ and has not been tested in the local Universe.

4.2 Stellar mass functions of MQGs

The works of Lagos et al. (2025b) and Baker et al. (2025c) show that the SMF is an important diagnostic of predictions of MQGs. While the number densities can compare reasonably well with observations, the SMF can reveal deficiencies and, in some cases, sharp tensions with the observations.

4.2.1 Results

We analyse the SMF of MQGs in Fig. 4. The left panel presents the SMF predicted by COLIBRE at different redshifts $2 \leq z \leq 7$ for the fiducial L200m6 simulation. The predictions show a clear increase in

the number of MQGs with decreasing redshift, as expected: galaxies need time to assemble enough stellar mass to be classified as massive, and additional time for quenching mechanisms to suppress their star formation. Consequently, the population shifts towards higher stellar masses at lower redshifts. Interestingly, these galaxies exhibit a peak around $M_\star \approx 10^{10.5} M_\odot$, where quenching is most efficient: galaxies are massive enough for the quenching mechanism to act strongly, yet extremely massive systems remain rare. Once quenched, they undergo little further stellar mass growth.

For comparison, in Fig. 4 we also show observational results from Baker et al. (2025a) and Stevenson et al. (2025). The COLIBRE results are broadly consistent with current observational constraints, which also show a similar peak (at around $M_\star \approx 10^{10.6} M_\odot$ in Baker et al. 2025a). A comparable peak is also reported in Shuntov et al. (2025) using the larger COSMOS-Web survey, although that study has reduced filter coverage and depth. We further test the impact of excluding satellite galaxies from the MQG selection and find that the SMF still peaks at a similar stellar mass to the case where both centrals and satellites are included. Differences between the two selections emerge only at the low-mass end across $2 \leq z \leq 6$, with a small fraction of quenched satellites already present by $z = 5$, potentially consistent with recent observational discoveries of such systems in overdense regions (Baker et al. 2025b).

While the observational data used here are robust in terms of large sample sizes and reliable selection of massive quenched systems, they are photometrically derived and thus may suffer from systematic uncertainties (Forrest et al. 2024). The lack of similarly large spectroscopic samples to measure SMFs highlights the need for future follow-up campaigns. Upcoming wide-area photometric surveys such as MINERVA (Muzzin et al. 2025), with extensive NIR and MIR coverage, will help reduce systematics and provide valuable targets for spectroscopic confirmation.

For completeness, we note that the SMF for the L400m7 simulation shows an excess of galaxies around $M_\star \approx 10^{10.6} M_\odot$ at all redshifts, consistent with the overestimated number densities discussed in § 4.1.1. In contrast, the L200m7h SMF at $z = 2$ predicts fewer galaxies at $M_\star \lesssim 10^{10.4} M_\odot$ and more at the high-mass end ($M_\star \gtrsim 10^{11.2} M_\odot$), while at $z > 2$ it yields lower number densities across the full mass range.

4.2.2 Comparison with galaxy formation models

The right panel of Fig. 4 presents the SMF after convolving stellar masses and SFRs with a Gaussian-distributed error of width 0.3 dex (as was computed for the number densities) at $z = 3$ in COLIBRE (L200m6). These results are compared with similarly error-convoluted predictions from other galaxy formation and evolution models for the $z = 3$ SMF with the same definition of massive quenched (except for GAEA, which does not include Gaussian-distributed errors either). A general trend emerges: models either accurately reproduce the low-mass end of the SMF (EAGLE, GALFORM), the high-mass end (SHARK v2.0) or both ends but not the intermediate mass regime (SIMBA), but none match the full mass range simultaneously. This has been noted in Lagos et al. (2025b) and Baker et al. (2025c) and linked to the different AGN feedback prescriptions. In contrast, COLIBRE performs well across the full stellar mass range. While GAEA and ILLUSTRIS-TNG may appear to match the full mass range, GAEA produces fewer galaxies above $M_\star \sim 10^{10.5} M_\odot$ and ILLUSTRIS-TNG suffers from small-number statistics at the high-mass end, with the number density of MQGs that declines rapidly beyond $z > 3$ (Fig. 3). Overall, the consistency of both SMFs and number densities in COLIBRE, once reasonable

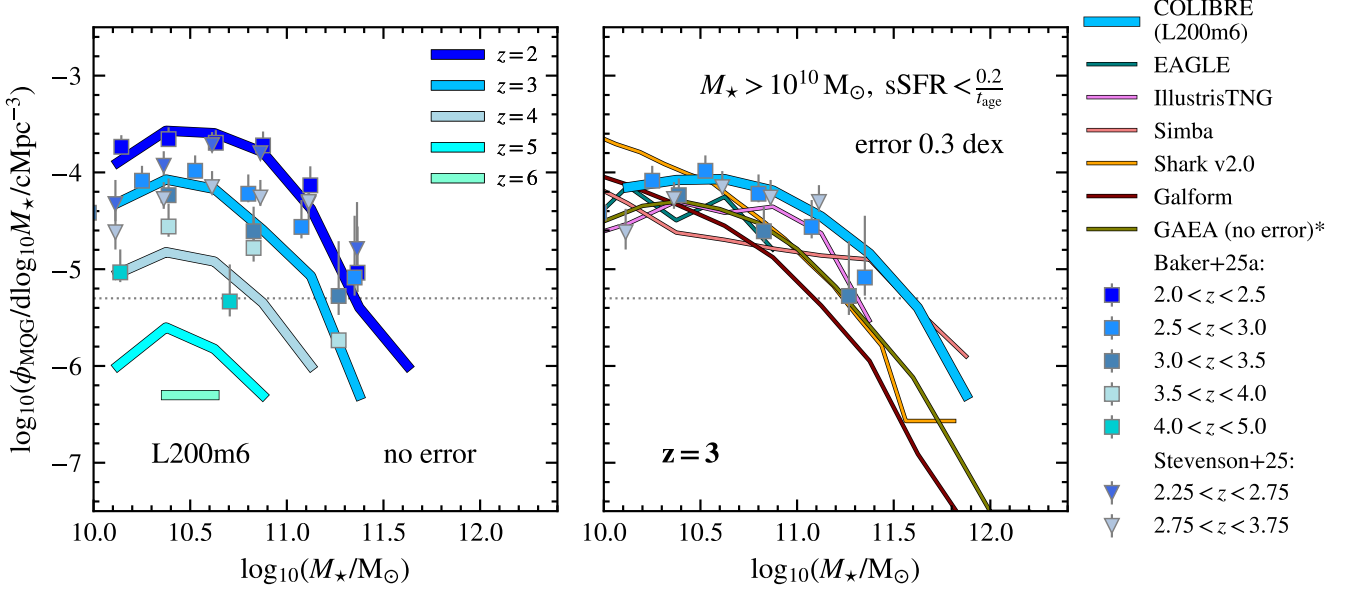


Figure 4. SMF of MQGs, defined by $M_\star > 10^{10}$ and $\text{sSFR} < 0.2/t_{\text{age}}$, from the fiducial L200m6 simulation. *Left panel*: predicted simulation values at different redshifts $2 \leq z \leq 7$ (colour-coded as labelled in the left panel), compared with observational estimates from Baker et al. (2025a) and Stevenson et al. (2025) within the same redshift range, as labelled. *Right panel*: the SMF at $z = 3$ from COLIBRE in light blue (fiducial L200m6) compared with results from other galaxy formation and evolution models, where M_\star and SFR values in the simulations are convolved independently with a Gaussian distribution (mean 0, standard deviation 0.3 dex) representing a reasonable error budget for these quantities (GAEA defines quenching using a fixed cut of $\text{sSFR} = 10^{-10} \text{ yr}^{-1}$ and its results are not convolved with potential observational errors). The horizontal dotted line denotes the threshold of 10 galaxies, below which the statistics become unreliable.

uncertainties in stellar masses and SFRs are considered, highlights its robust performance in reproducing MQG properties compared to other models. The SMF results derived with the error convolution across the full redshift range are shown in Appendix C.

4.3 Star formation histories of MQGs

SFHs provide key insights into how galaxies assemble their stellar mass (through a single intense starburst, multiple bursts, or an extended period of star formation) and how quenching occurs, either abruptly or gradually. Here, we reconstruct SFHs (§ 3.2) for the selected MQGs in COLIBRE and compare with observational data. Before we present our main results, it is important to note some caveats for the following subsections in § 4 compared to observations:

- To select massive quenched systems, we use the predicted M_\star and SFR of galaxies in COLIBRE, ignoring any potential uncertainties in these quantities.
- The observational samples considered here consist of spectroscopically confirmed galaxies. This is important, as photometrically selected galaxies are less robust as explained earlier, particularly at high redshift (Forrest et al. 2024).
- The definition of “massive quenched” varies across observational studies; this should be kept in mind when interpreting results.

In Fig. 5, we show the fiducial COLIBRE simulation predictions for SFH properties as a function of M_\star , compared to recent *JWST* spectroscopic observations, displayed as individual data points colour-coded by spectroscopic redshift. Observationally, SFHs are derived from SED modelling. For the data from Nanayakkara et al. (2025); Baker et al. (2025c), we use the full SFH Markov chain Monte Carlo (MCMC) output provided by the SED-fitting code PROSPECTOR (Johnson et al. 2021), computing each galaxy’s properties as the

median and the 16th and 84th percentile range of the MCMC. For Nanayakkara et al. (2025), we adopt an exponentially increasing continuity prior between SFH bins rather than the manuscript’s fiducial choice, which is broadly consistent with expectations from Λ CDM cosmology (Dekel et al. 2013). For Carnall et al. (2024), we use the values reported directly in the paper.

4.3.1 Formation timescale

In the top panel of Fig. 5, we show the formation timescale for MQGs (the lookback time from the time of selection at which 50% of the $z = 0$ stellar mass without accounting for mass losses was formed; see §3.2) as a function of M_\star . Each colour represents the median relation at a different selection redshift, with shaded areas indicating the corresponding 16th and 84th percentile range. Here, we focus on MQGs selected at $2 \leq z \leq 5$, although there are too few galaxies at $z > 4$ for L200m6 to compute reliable medians per stellar mass bin. In L200m6, the simulated galaxies undergo a rapid mass assembly, forming the bulk of their mass early in cosmic time, with no significant dependence on stellar mass. Selections at higher redshift correspond to later t_{50} due to the limited cosmic time available, but also to earlier median t_{50} values: $z_{50} = 3.40$ at $z = 2$, $z_{50} = 4.47$ at $z = 3$, $z_{50} = 5.25$ at $z = 4$, $z_{50} = 6.08$ at $z = 5$, and $z_{50} = 7.28$ at $z = 6$ (for 2 galaxies), consistent with expectations. The scatter decreases with redshift, which may reflect smaller sample sizes at higher redshifts. In L400m7 (thin lines), t_{50} interestingly peaks at $M_\star \approx 10^{10.2} M_\odot$ and increases again at higher masses.

Qualitatively, the simulation values in the top panel are consistent with the observational sample. The Nanayakkara et al. (2025) data show shorter formation timescales around $M_\star \approx 10^{11} M_\odot$, indicating later mass assembly and burstier SFHs than in COLIBRE, a trend also seen across the full mass range in Baker et al. (2025c).

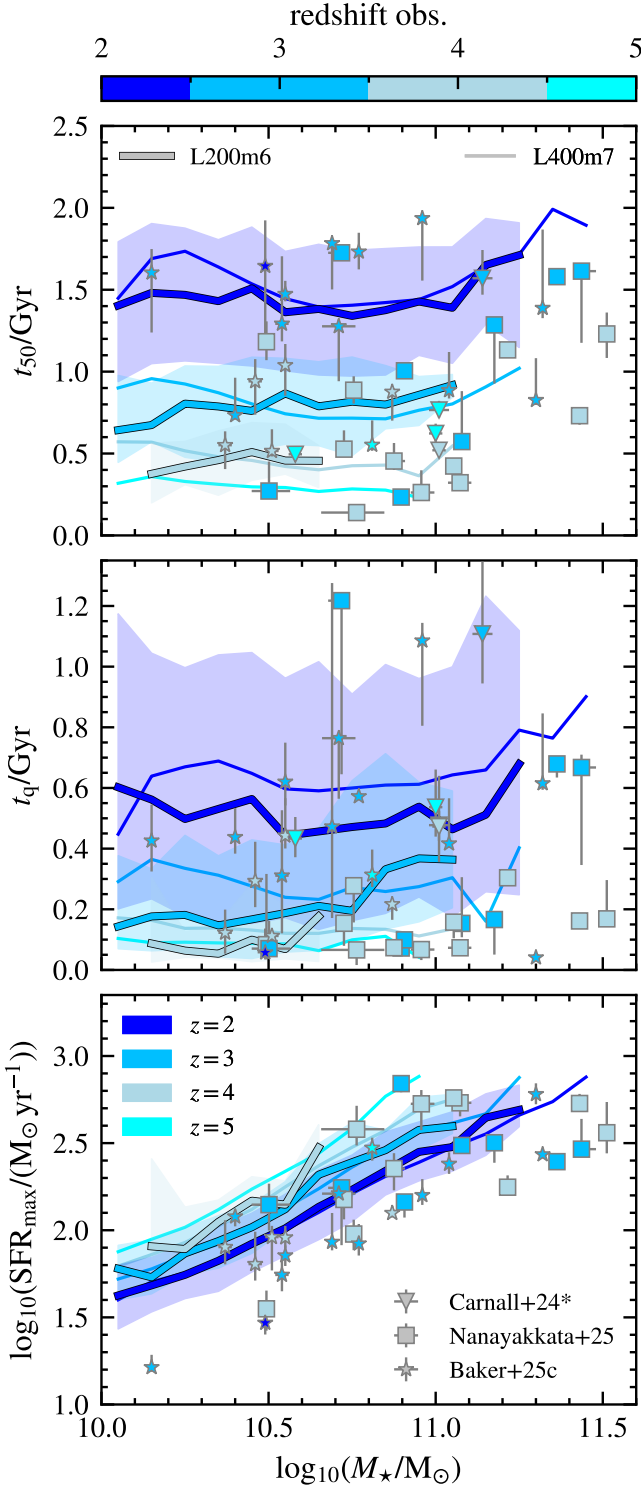


Figure 5. SFH properties of MQGs as a function of M_\star . Thick solid lines show the median predictions from L200m6 at different redshifts $2 \leq z \leq 5$ (as labelled in the bottom panel), with shaded regions indicating the 16th and 84th percentile range. At $z = 5$, MQGs are too few to split in stellar mass bins (9 galaxies). Thin solid lines show the corresponding medians from L400m7. These are compared to recent *JWST* spectroscopic measurements (Carnall et al. 2024; Nanayakkara et al. 2025; Baker et al. 2025c), shown as symbols colour-coded by observed galaxy redshift, with the corresponding colorbar at the top. *Top panel*: formation times (t_{50}), defined in § 3.2. *Middle panel*: quenching times (t_q), defined in § 3.2 (the earliest lookback time at which the galaxy first crosses the threshold $\text{sSFR} < 0.2/t_{\text{age}}$ for Carnall et al. 2024). *Bottom panel*: SFR peak (SFR_{max}) (no data from Carnall et al. 2024).

However, as discussed in Section 4.3.4, early-time SFHs are observationally uncertain because old stellar populations provide limited constraints. The same applies to the few longer timescales inferred from $z \approx 3$ observations. Observed galaxies at the high-mass end ($M_\star \gtrsim 10^{11.2} M_\odot$) are not well matched by the simulation medians either. The Carnall et al. (2024) observations display a different behaviour compared to the other two studies. This is likely due to their distinct SFH parametrisation using a double power-law in BAGPIPES (Carnall et al. 2018) (parametric form as opposed to the non-parametric of the other two works, discussed in § 4.3.4), which tends to produce SFHs resembling a single burst with minimal star formation outside that period.

4.3.2 Quenching timescale

In the middle panel of Fig. 5, we examine the quenching timescale (as defined in lookback time from the time of selection in § 3.2). We find no strong trend with M_\star for L200m6. Higher-redshift systems exhibit lower t_q values, although this trend is less pronounced than for the formation times. Galaxies at earlier times quenched more recently relative to their selection redshift, as expected, since the available cosmic time is shorter. The median values are $z_q = 2.36$ for selection at $z = 2$; $z_q = 3.26$ at $z = 3$; $z_q = 4.20$ at $z = 4$; $z_q = 5.27$ at $z = 5$; and $z_q = 6.14$ at $z = 6$ (for 2 galaxies).

The L400m7 simulation (thin lines) exhibits the same peak in t_q as in t_{50} , around $M_\star \approx 10^{10.2} M_\odot$. Although not shown, the scatter at $z = 2$ is comparable to that in L200m6, despite the larger number of galaxies. L200m7h shows significantly shorter quenching timescales ($t_q \lesssim 0.4$ Gyr) at $z = 2$ for low-mass systems ($M_\star < 10^{10.5} M_\odot$), producing a non-flat positive correlation between quenching time and stellar mass, where more massive galaxies quench earlier.

COLIBRE predictions broadly agree with observations, indicative of recent quenching $t_q \lesssim 0.6$ Gyr. The simulated data recover the Baker et al. (2025c) data well. The Nanayakkara et al. (2025) data show shorter quenching timescales around $M_\star \approx 10^{11} M_\odot$, consistent with the later formation timescales found previously due to burstier SFHs. Carnall et al. (2024) uses a different definition for t_q (the earliest lookback time at which the galaxy first crosses $\text{sSFR} < 0.2/t_{\text{age}}$) yielding longer values, although they follow the same overall trend as the formation times because of the double power-law SFH parametrisation (parametric form).

4.3.3 Peak of SFR

Finally, we show the SFR peak, SFR_{max} , in the bottom panel of Fig. 5. The lookback time of the SFR peak, $t_{\text{SFR}_{\text{max}}}$, follows a similar trend to that of t_{50} (as shown in Fig. 1). SFR_{max} increases with galaxy mass, reflecting the stronger SF episodes required to assemble more stellar mass. The peak also decreases toward lower redshift, indicating that stellar mass can be built up more gradually over time, rather than through a single intense starburst as seen for MQGs selected at $z = 4$. Observational results exhibit considerable scatter but generally follow a similar trend with selection redshift. Values in Nanayakkara et al. (2025) and Baker et al. (2025c) are quantitatively reproduced, suggesting that, although some galaxies may form and quench later, the strength of their starbursts is comparable. In addition, a fraction of galaxies experience very strong starbursts in L200m6 ($\text{SFR}_{\text{max}} > 300 M_\odot \text{ yr}^{-1}$): 10% at $z = 2$, 14% at $z = 3$, 23% at $z = 4$, 27% at $z = 5$ (3 galaxies), and 50% at $z = 6$ (1 galaxy). This may point to an evolutionary link with highly star-forming galaxies.

4.3.4 Discussion

The level of agreement between simulations and observations is highly sensitive to sample selection and the assumptions made during SED fitting, even when spectroscopic data are available. Choices made during SED fitting can introduce systematic biases that affect the inferred galaxy properties. In particular, the complex SFHs involving multiple bursts, described in § 3.2, are challenging to recover via SED-fitting (Suess et al. 2022; Wang et al. 2025a).

For example, Nanayakkara et al. (2025) compares two different codes: PROSPECTOR and FAST++ (Kriek et al. 2009). While both produce qualitatively consistent average SFHs for large samples, individual SFHs differ due to distinct assumptions regarding metallicity, SFHs, SSPs, and other parameters. In particular, the parametric nature of FAST++ (the BAGPIPES results from Carnall et al. 2024) favours less gradual mass build-up and narrower bursts than the more flexible SFH parametrisation of PROSPECTOR; this results in stronger early-time enhancement (fig. 11 in Nanayakkara et al. 2025). Some scatter in derived properties such as stellar masses is therefore expected (Leja et al. 2019b), and according to Nanayakkara et al. (2025) could be up to ≈ 0.4 dex.

Even within PROSPECTOR, choices such as the selection of SSP models and the priors used in non-parametric SFH reconstructions can influence the inferred properties of individual galaxies. These effects are typically minor, but they become more pronounced during the first ≈ 250 Myr of cosmic history, when old stellar populations dominate the observed spectrum and time resolution is inherently limited, likely contributing to the shorter observational timescales. Incorporating rest-frame near-IR (NIR) data helps mitigate these uncertainties. In this work, we compare to the results of Nanayakkara et al. (2025), who use an exponentially increasing continuity prior between SFH bins, motivated by the average halo mass accretion rate over cosmic time (Dekel et al. 2013), which is consistent with expectations from a Λ CDM framework. By contrast, Baker et al. (2025c) also employ PROSPECTOR with a non-parametric SFH, but adopt a flat continuity prior (Leja et al. 2019a), use different lookback time binning, and rely on distinct SSP models: C3K (Conroy et al. 2009) in Nanayakkara et al. (2025) versus MILES (Falcón-Barroso et al. 2011) in Baker et al. (2025c); among other methodological differences. Appendix D illustrates how these choices impact the recovered median SFH shapes of observed galaxies.

We emphasise that, although observational estimates of these SFH properties carry significant uncertainties, and we have not applied the 0.3 dex convolution error for M_\star and SFR when selecting our sample for this analysis, there is still overall broad agreement between our COLIBRE predictions and the observational estimates across all measured properties. Performing SED-fitting of COLIBRE MQGs is left for future work and will help clarify these comparisons.

4.4 Dust and molecular hydrogen fractions of MQGs

Dust and molecular gas are fundamental components in quenched galaxies, closely tied to their star formation history. Molecular gas, the primary fuel for star formation, is expected to be depleted in MQGs due to quenching mechanisms such as gas ejection or thermal heating, resulting in low gas reservoirs. Dust exhibits a similar decline: it originates from star formation processes, grows within the ISM, and can be destroyed or expelled by feedback. Importantly, dust grains facilitate the formation of molecular hydrogen and their emission is commonly used as a proxy for molecular gas content (Tacconi et al. 2020). As such, molecular gas, dust, and star formation are

intimately connected, and their co-evolution provides key insights into the quenching process.

Observations at lower redshift indicate that the dust (Gobat et al. 2018; Magdis et al. 2021) and molecular gas (Spilker et al. 2018) content of MQGs can evolve significantly. However, constraints for high-redshift quiescent galaxies remain limited: their emission is intrinsically faint, and until recently, telescopes lacked the sensitivity to detect them. Consequently, most available measurements are either upper limits from non-detections or are biased toward quiescent systems that are unusually gas- and dust-rich. Upcoming observations with instruments such as *JWST* MIRI and NIRSpec, deep ALMA surveys, and the future *PRIMA* space-based observatory (Faisst et al. 2025, covering the wavelength gap between the previous two) are expected to improve these measurements substantially, making theoretical predictions from simulations particularly valuable. COLIBRE provides an ideal testbed for such predictions, as it models dust self-consistently, and captures a cold gas phase, with temperatures as low as ~ 10 K (§ 2). This enables a relatively realistic treatment of both components and a direct investigation of their content.

4.4.1 Dust fraction evolution

Fig. 6 shows the evolution of the dust fraction, $f_{\text{dust}} = M_{\text{dust}}/M_\star$, for MQGs as a function of selection redshift. The blue line indicates the median value, with shaded regions representing the 16th and 84th percentile range. We find that the dust fraction remains roughly constant at $f_{\text{dust}} \sim 10^{-4}$ across $2 \leq z \leq 6$ for both L200m6 (thick) and L400m7 (thin lines) (beyond $z > 5$ there are only 2 MQGs for L200m6). For comparison, the dust fractions of MSFGs (selected using the same stellar mass cut and sSFR threshold as in § 3) are also shown (dashed grey line). MSFGs exhibit dust fractions at least two orders of magnitude higher than MQGs, consistent with the expectation that ISM material in passive systems is removed by the feedback processes responsible for quenching, even at high redshift and over short timescales (Leśniewska et al. 2025).

Observational constraints on dust content are typically obtained from far-IR/sub-mm continuum data by fitting a modified blackbody spectrum to the SED, assuming a fixed dust temperature and emissivity. These assumptions, however, introduce significant uncertainties, especially at high redshift (Sommovigo & Algara 2025). The top panel of Fig. 6 compiles current dust measurements and upper limits for spectroscopically confirmed quenched⁶. Lee et al. (2024) report a single source with unusually high dust content, clearly at odds with the MQGs in our simulations and likely representing a rare dust- and gas-rich quenched system, same as one galaxy in Suzuki et al. (2022), and another one in Whitaker et al. (2021a) (although the dust fraction is slightly lower). These systems are rare in COLIBRE (Fig. 7), but there is overlap with the Whitaker et al. (2021a) system. Other observations shown with arrows and a more faded colour (Whitaker et al. 2021a; Kalita et al. 2021; Suzuki et al. 2022; Setton et al. 2024) are upper limits, which are consistent with our predictions.

4.4.2 Molecular hydrogen fraction evolution

Molecular gas observations are less reliable due to the absence of strong emission lines or direct H₂ detections. Molecular gas masses

⁶ Lee et al. (2024); Suzuki et al. (2022) only account for photometric errors (the latter one not including M_\star uncertainties); while Whitaker et al. (2021a) consider uncertainties additionally when varying the dust temperature.

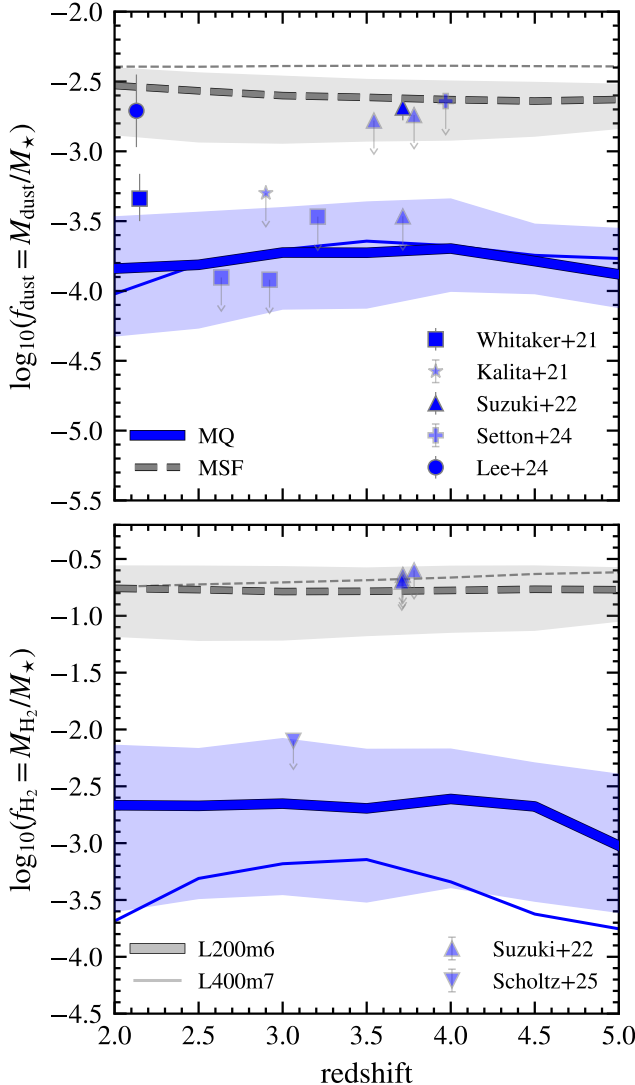


Figure 6. Dust fraction, $f_{\text{dust}} = M_{\text{dust}}/M_{\star}$, (top panel) and molecular hydrogen fraction, $f_{\text{H}_2} = M_{\text{H}_2}/M_{\star}$, (bottom panel) as a function of redshift at $2 \leq z \leq 5$ for L200m6. Median values for the MQGs (thick solid blue) and MSFGs (thick dashed grey) with the corresponding 16th and 84th percentile range at each selection redshift. At $z = 6$, MQGs are too few to define a median (1 galaxy), since we consider here all galaxies together rather than splitting by stellar mass bins. Thin lines show the corresponding median from L400m7. Observational data of MQGs are taken from the literature: for dust fractions from Whitaker et al. (2021a); Kalita et al. (2021); Suzuki et al. (2022); Setton et al. (2024); Lee et al. (2024), and for molecular hydrogen fractions from Suzuki et al. (2022); Scholtz et al. (2024). Arrows indicate upper limits from non-detections (also shown with a more faded colour).

are therefore typically inferred either from dust continuum measurements, assuming a dust-to-gas ratio (DGR) (e.g., Whitaker et al. 2021b; Chang et al. 2025), or from emission of tracers such as CO, [CII], or [CI] (e.g., Suzuki et al. 2022), which rely on uncertain conversion factors. The bottom panel of Fig. 6 shows the median molecular hydrogen fraction, here referring exclusively to H_2 , and its scatter in these systems. For L200m6, the molecular hydrogen fraction remains roughly constant over time and is about two orders of magnitude lower in MQGs than in star-forming counterparts, consistent with H_2 photodissociation driven by feedback processes. In L400m7, the molecular hydrogen fraction is about 1 dex lower, potentially indi-

cating a more efficient destruction of molecular gas by a more bursty feedback while the dust content remains comparable.

Observational estimates not derived from dust continuum, and thus not requiring corrections, as they trace H_2 alone; are included: all of them are upper limits either from [CI] (Suzuki et al. 2022) or CO (Scholtz et al. 2024) (which hosts a neutral outflow that efficiently removed gas, indicative of ejective AGN feedback), illustrating the difficulty of measuring molecular gas in these systems due to their low reservoirs. The COLIBRE predictions are consistent with these observational upper limits.

4.4.3 Distribution functions

In Fig. 7, we show (from left to right) the distributions of the dust fraction, f_{dust} ; molecular hydrogen fraction, f_{H_2} ; and dust-to-gas ratio (DGR), $\delta_{\text{DGR}} = M_{\text{dust}}/M_{\text{H}_2}$ for L200m6 (thick) and L200m7 (thin) lines. Each coloured line represents the distribution at a different redshift, while vertical dashed lines indicate the median values for MSFGs of the same stellar mass.

Focusing on f_{dust} (left panel), for L200m6 we see that typical values cluster around $f_{\text{dust}} \sim 10^{-4}$ but the distribution has extended tails. Some galaxies reach $f_{\text{dust}} \sim 10^{-3}$, comparable to values found in MSFGs. These likely represent galaxies that have not yet removed their dust, consistent with the fact that systems with $f_{\text{dust}} > 10^{-4}$ show shorter median quenching times ($t_{\text{q}} \sim 0.4$ Gyr) than those with $f_{\text{dust}} \leq 10^{-4}$ ($t_{\text{q}} \sim 0.7$ Gyr) at $z = 2$. Appendix F1 shows that this correlation is shallow and exhibits substantial scatter, though.

The L400m7 simulation exhibits a higher distribution, as was seen for the number densities. It also shows an increased number of galaxies with extremely low dust fractions ($f_{\text{dust}} < 10^{-4}$), reaching values as low as $f_{\text{dust}} \sim 10^{-6}$ across all redshifts. This may suggest that a more bursty feedback implementation can reduce dust content more dramatically. A similar broadening at the low-dust end is observed in L200m7h at $z = 2$.

Dust may also regrow in the ISM or through external processes after quenching, potentially linked to AGN feedback. Both scenarios have been proposed in both observations (e.g., Donevski et al. 2023; Kakimoto et al. 2024) and other simulations, including SIMBA (Lorenzon et al. 2025). SIMBA, like COLIBRE, includes explicit ISM dust growth, but following McKinnon et al. (2017). Unlike COLIBRE, however, SIMBA’s dust budget is dominated by direct stellar production, driven by the order-of-magnitude larger stellar dust yields adopted from Dwek (1998) (see fig. 1 in Trayford et al. 2025), and it does not model the cold ISM.

Focusing on the molecular hydrogen fraction (middle panel), we see that the peak values for the quenched population are more than an order of magnitude lower than those of star-forming galaxies for L200m6, consistent with gas depletion due to quenching. Nevertheless, a fraction of galaxies retain significant molecular gas reservoirs, with $f_{\text{H}_2} > 10^{-2}$. These systems correspond to the relatively high-dust content galaxies (see the correlation between f_{dust} and f_{H_2} in Appendix F1) that quench at later times.

L400m7 again shows a larger number of galaxies with extremely low molecular gas fractions ($f_{\text{H}_2} < 10^{-4}$). In contrast, L200m7h produces results similar to L200m6 for f_{H_2} . Given that dust fractions are lower in L200m7h compared to L200m6, this suggests that dust is removed more efficiently than molecular gas in the hybrid feedback model. This may occur because jets affect dust more strongly. In SIMBA, the combination of AGN feedback and fast/slow quenching determines the future fate of dust: the jet mode removes dust over short (slow quenchers) or long (fast quenchers) timescales, while radiative-mode systems allow dust regrowth in the ISM (Lorenzon

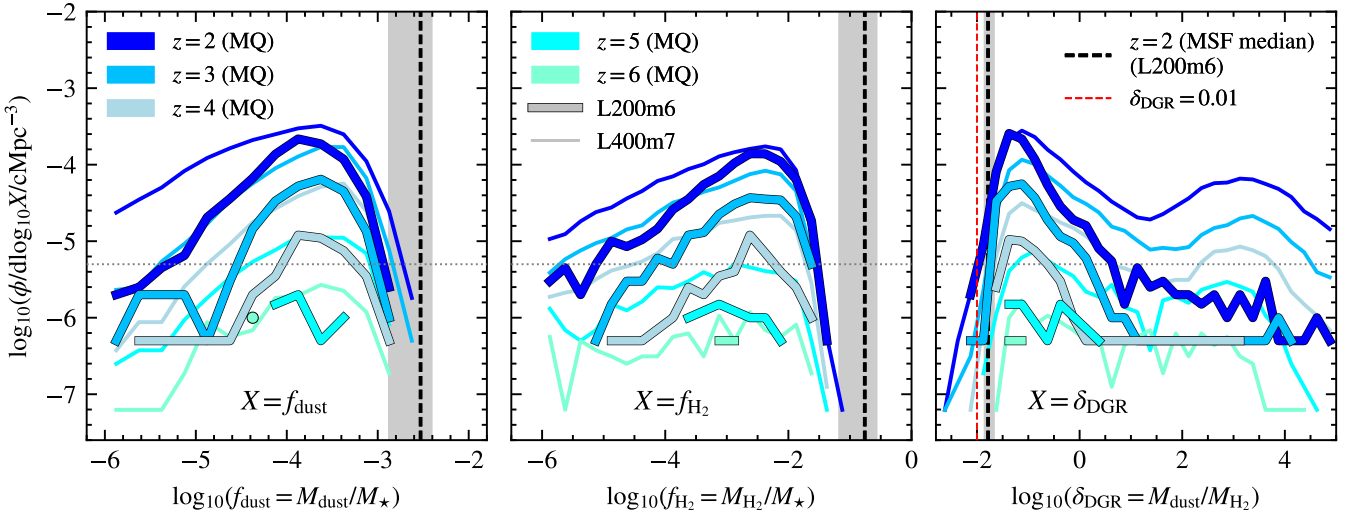


Figure 7. Distribution functions of dust fraction, $f_{\text{dust}} = M_{\text{dust}}/M_{\star}$ (left panel), molecular gas fraction, $f_{\text{H}_2} = M_{\text{H}_2}/M_{\star}$ (middle panel), and dust-to-gas ratio, $\delta_{\text{DGR}} = M_{\text{dust}}/M_{\text{H}_2}$ (right panel) for L200m6. Solid lines show the distributions for MQGs, colour-coded by selection redshift ($2 \leq z \leq 6$). Vertical dashed lines indicate the median values for MSFGs at $z = 2$, with shaded regions marking the corresponding 16th and 84th percentile range. Thin lines show the corresponding medians from L400m7. In the right panel, the red vertical dashed line marks the canonical value $\delta_{\text{DGR}} = 0.01$. The horizontal dotted line denotes the threshold of 10 galaxies for L200m6, below which the statistics become unreliable.

et al. 2025). Prospective work could explore whether similar correlations exist in COLIBRE.

The DGR distribution (right panel) reveals that passive galaxies exhibit a wide scatter in this quantity, with median values intriguingly higher ($\delta_{\text{DGR}} \sim 0.1$) than those of star-forming galaxies. Gas metallicity (measured within the 50 pkpc fiducial aperture as the linear sum of the diffuse oxygen over hydrogen ratio of gas, multiplied with the gas mass) for the MQGs is lower and despite this, they have a higher DGR value (e.g. the median values for $12 + \log_{10}(\text{O/H})$ at $z = 2$ are ≈ 8.14 for MQGs and ≈ 8.49 for MSFGs). This suggests that molecular gas is destroyed more rapidly than dust. L400m7 (and similarly L200m7h) predicts a pronounced local peak in DGR around $\delta_{\text{DGR}} \sim 1000$, corresponding to galaxies that retain significant dust.

Here we omit galaxies with $M_{\text{H}_2} = 0$. In L200m6, only $\approx 2\%$ of MQGs at $z = 2$ fall into this category (and 90% of those also have $M_{\text{dust}} = 0$), with the fraction decreasing toward higher redshifts. The $z = 2$ median value for MSFGs is computed including the $M_{\text{H}_2} = 0$ cases, although in practice none occur.

The DGR results support the idea that dust content may more closely reflect the nature of the quenching feedback (e.g. AGN-driven), with molecular gas and dust evolving on different timescales. This behaviour has been reported using SIMBA (Lorenzon et al. 2025). However, in SIMBA the H_2 content is computed using the Krumholz & Gnedin (2011) prescription rather than by resolving the cold ISM, and its DGRs are systematically lower than in COLIBRE. The latter difference arises from the contrasting dust models: in SIMBA, stellar yields play the dominant role, while ISM dust growth is insufficient to offset them, resulting in systematically lower dust masses and DGRs.

Moreover, the common observational assumption of a constant DGR of ~ 0.01 (red vertical dashed line) for the total ISM gas content (not only for the dense, cold H_2 ; see, e.g., Whitaker et al. 2021a; Setton et al. 2024) may be an oversimplification, as even when computing the ratio as $M_{\text{dust}}/(M_{\text{HI}} + M_{\text{H}_2})$, the model predicts substantially lower DGRs, with median values of ~ 0.001 for MQGs.

More observational data are needed to robustly test these predictions. While recent programs are beginning to address this, current samples remain small. Future surveys will increase the number

of detected objects and may enable stacking analyses for dust and molecular gas measurements, including non-detections, following the approach of Adscheid et al. (2025), but for spectroscopic samples. This will be crucial since, as noted earlier, existing observations are biased toward dust- and gas-rich systems.

4.5 Sizes of MQGs

Quenched galaxies are known to evolve in size, with trends differing from those of their star-forming counterparts at $z \lesssim 3$. van der Wel et al. (2014) find that quenched systems are more compact than star-forming galaxies and exhibit a more dramatic evolution, reaching much smaller sizes near $z = 3$ than their descendants at $z \approx 0$ (Buitrago et al. 2008; van Dokkum et al. 2008; Cutler et al. 2022). Thanks to the high resolution of JWST, direct measurements of rest-frame NIR and optical sizes are now possible up to $z \approx 5$. Observations reveal that high- z MQGs are very compact, with typical effective radii below 1 kpc (Wright et al. 2024b; Ito et al. 2024; Williams et al. 2024; Kawinwanichakij et al. 2025). These studies also report negative colour gradients (Wright et al. 2024b; Ito et al. 2024), indicative of older stellar populations in the centre, which supports an inside-out growth scenario.

In simulations, reproducing such compact sizes can be challenging because of resolution limitations (Remus & Kimmig 2025). It is therefore interesting to examine the sizes of MQGs in COLIBRE.

4.5.1 Results & discussion

The top panel of Fig. 8 shows the galaxy mass-size relation for MQGs from the fiducial L200m6 simulation, where sizes are defined by the stellar half-mass radius averaged over three random projections (r_{\star} ; see § 3). These are shown as solid coloured lines for $2 \leq z \leq 4$ for the fiducial simulation. Dashed lines indicate the corresponding relation for MSFGs at the same redshifts. Overall, we find no significant differences between the two populations, although MQGs appear slightly more compact at the low-mass end ($M_{\star} \lesssim 10^{10.5} M_{\odot}$) at

$z = 2$. This result is consistent with [Ormerod et al. \(2024\)](#), who report no distinction between both populations at $z > 3$; but contrasts with [van der Wel et al. \(2014\)](#), who find that quenched systems are more compact even at $z \approx 2 - 3$.

Blue arrows indicate the gravitational softening length, ϵ_{prop} , at different redshifts (see Table 1). The similarity between the median values and ϵ_{prop} at $z = 4$, and their proximity at $z = 3$, reflects that caution is needed when interpreting predictions at high redshifts, since gravity is non-Newtonian below this scale. However, the flattening at our low-mass end when including all systems (MQGs and MSFGs) is also present in L400m7, which has a lower spatial resolution. This suggests that the feature is not a direct consequence of the softening length. A similar case, where flattening at low masses near the spatial resolution limit does not arise from the softening length, was found for EAGLE (fig. 8 in [Ludlow et al. 2023](#)), where it was instead driven by low DM mass resolution. Predictions for the L400m7 run are provided in Appendix E.

We find that galaxies become larger with decreasing redshift, highlighting their size evolution. The most massive systems are also more extended, and the slope of the mass–size relation appears to change around $M_\star \sim 10^{10.8} M_\odot$, at least in the $z = 2$ results. This trend is consistent with [Ji et al. \(2024\)](#), who identify a similar transitional mass scale for MQGs, where more massive objects evolve more rapidly with likely higher ex-situ stellar mass contributions. We also find that the most compact galaxies tend to have later formation times (with median $t_{50} \approx 1.3$ Gyr for $r_\star \leq 1$ kpc, while $t_{50} \approx 1.5$ Gyr for $r_\star > 1$ kpc at $z = 2$, and similar at other redshifts as shown in Appendix F1) in agreement with observational results (see fig. 11 in [Kawinwanichakij et al. 2025](#)).

The galaxy sizes in our analysis are defined as the stellar half-mass radius. Observational studies, however, typically use half-light radii, which are themselves influenced by projection effects (although in our case, averaging over three random projections helps to minimise these). Observationally, galaxy sizes are typically measured by fitting a [Sersic \(1968\)](#) profile to the surface brightness distribution (including point spread function (PSF) convolution) and deriving the half-light effective radius. The inferred sizes depend not only on the fitting algorithm used ([Häussler et al. 2007](#)) but also on the wavelength probed ([Suess et al. 2019](#)), with NIR measurements offering the most reliable tracer of stellar mass ([Bell & de Jong 2001](#)). For this reason, we introduce NIR-based observations in Fig. 8, despite the methodological and sample selection differences with simulations. Taking these caveats into account, the agreement with [de Graaff et al. \(2025\)](#); [Kawinwanichakij et al. \(2025\)](#); [Baker et al. \(2025c\)](#) appears to be of a qualitatively good nature.

4.6 Kinematics of MQGs

We also examine the kinematics of MQGs, characterised by the stellar rotation-to-dispersion velocity ratio, v_\star/σ_\star . At $z \approx 0$, MQGs are primarily dispersion dominated, but their rotational support increases at higher redshift ([van Dokkum et al. 2008](#); [van der Wel et al. 2011](#); [Belli et al. 2017](#)). Measuring stellar kinematics in these compact systems is challenging and, before *JWST*, was only feasible in strongly lensed cases ([Newman et al. 2018](#)). Observationally, v_\star/σ_\star is derived from spectral absorption features via line fitting, which requires very high signal-to-noise ratios and is particularly demanding at high redshift. Additional systematics arise from wavelength coverage, fitting codes, and modelling assumptions ([Belli et al. 2017](#)). *JWST* has now opened a new window: with NIRSpec/IFU and NIRSpec/MSA, spatially resolved kinematics can be obtained even for faint, compact galaxies, complemented by forward kinematic modelling ([Pascalau](#)

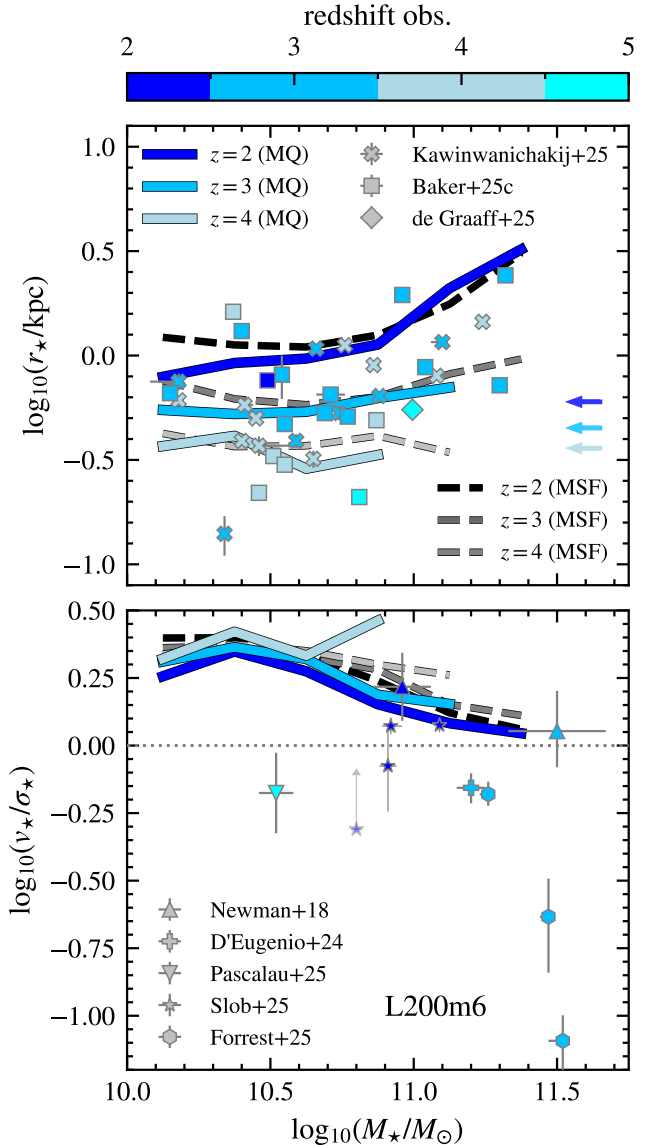


Figure 8. Stellar size-mass relation, with r_\star defined as the half-mass radius (top panel); and v_\star/σ_\star versus stellar mass relation for L200m6. Solid blue-palette lines show the median predictions for MQGs, and dashed grey-palette lines for MSFGs at different selection redshifts, $2 \leq z \leq 4$. At $z > 4$, the number of massive quenched systems is too small to define a median split in stellar mass bins (9 galaxies at $z = 5$ and 2 at $z = 6$). Observational data of MQGs are from [Kawinwanichakij et al. \(2025\)](#); [Baker et al. \(2025c\)](#); [de Graaff et al. \(2025\)](#) for the size-mass relation (defined as half-light radius), and [Newman et al. \(2018\)](#); [D'Eugenio et al. \(2024\)](#); [Pascalau et al. \(2025\)](#); [Slob et al. \(2025\)](#); [Forrest et al. \(2025\)](#) for the v_\star/σ_\star -mass relation. Arrows in the error bars indicate lower limits for galaxies where rotational velocity could not be constrained (also shown with a more faded colour). Blue arrows in the size–mass relation mark the gravitational softening length, ϵ_{prop} , at each redshift.

[et al. 2025](#); [Slob et al. 2025](#)). These advances highlight the importance of simulation-based predictions for interpreting observations.

4.6.1 Results and discussion

The bottom panel of Fig. 8 shows COLIBRE predictions for v_\star/σ_\star (computed as in § 3.3) as a function of stellar mass in the range

$2 \leq z \leq 4$ for L200m6. Solid blue-palette lines indicate the median values for MQGs, while dashed grey-palette lines show MSFGs. Observational results from lensed systems (Newman et al. 2018) and JWST (D’Eugenio et al. 2024; Pascalau et al. 2025; Slob et al. 2025; Forrest et al. 2025) are included for comparison.

The horizontal dotted line ($v_\star/\sigma_\star = 1$) serves as a reference. There is a clear offset between the simulation predictions and the observations: most COLIBRE MQGs lie above this threshold, appearing more rotationally supported than the observed galaxies. However, it is important to recall that the simulation values represent upper limits relative to the observations, due to differences in definitions and the caveats (§ 3.3). In addition, some observational values (e.g., Forrest et al. 2025) are reported using the spin parameter λ_r and have been converted to v_\star/σ_\star using the relation in Cappellari (2016); apart from differences in sample selection. A more detailed comparison that closely mimics the observational analysis is left for future work.

Current observations suggest MQGs are commonly fast rotators at high redshift (Pascalau et al. 2025). One exception is the slow rotator reported by Forrest et al. (the lowest datapoint from 2025), likely the result of a major merger or isotropic gas infall (values around $v_\star/\sigma_\star = 0.4$ are generally taken to indicate dispersion-dominated systems; Cappellari 2016). In COLIBRE, individual slow-rotator MQGs are also present at $z = 2$ in the left panel of Fig. F2.

Both MQGs and MSFGs in COLIBRE become more dispersion-supported towards lower redshift, with the most massive systems showing the strongest bulge dominance by $z \lesssim 3$. At $z \gtrsim 2$, however, MQGs and MSFGs exhibit similar kinematics, implying that quenching preserves discs and precedes morphological transformation. Predictions for L400m7 are provided in Appendix E, where the trend reverses, with morphological transformation occurring before quenching. This is likely a consequence of its larger softening length, which limits the ability to resolve the internal structure of galaxies.

In the EAGLE simulations, Lagos et al. (2022) showed this behaviour with galaxies quenching first, and only later (≈ 2 Gyr) evolving into slow rotators through mergers (particularly dry mergers) that increase masses, sizes, and erode rotational support (see also Lagos et al. 2018). Feedback mechanisms do not appear to affect kinematics directly, as seen in D’Eugenio et al. (2024), where a rotation-supported system showed clear evidence of ejective feedback. The absence of star-forming gas in quenched galaxies likely makes mergers (particularly dry mergers) more effective at disrupting rotational support. This may explain why MQGs in COLIBRE show slightly lower v_\star/σ_\star than coeval MSFGs by $z \approx 2$, in agreement with Pascalau et al. (2025). However, this contrasts with the findings of Shuntov et al. (2025), who report that most high- z MQGs are bulge-dominated, implying that a morphological transformation occurred before quenching.

This emerging population of slow rotators is found primarily in dense environments or recently quenched systems, consistent with our finding of a correlation between dispersion and environment (Appendix F2). More extended objects are also more dispersion-supported (left panel of Fig. F1), supporting the merger-driven scenario, since mergers increase size.

5 THE JOURNEY OF MQGS

We now turn to developing a deeper understanding of the physical drivers that shape the properties of MQGs in the COLIBRE model. In § 5.1, we investigate what suppresses star formation so early in time for such massive systems. We focus on the role of AGN feedback because it is most likely to be the dominant mechanism driving

quiescence⁷. In § 5.2, we explore the link between quenching and a galaxy’s environment, and how this shapes its subsequent evolution. Finally, in § 5.3, we examine the long-term fate of MQGs and their potential to undergo rejuvenation episodes.

For this part of the analysis, we fix the selection redshift for our samples at $z = 3$, which provides sufficient statistics, and we have verified that the results are similar when the sample is selected at another redshift $z \geq 2$. We follow the merger histories of both MQGs and MSFGs, tracking their evolution backwards and forwards in time relative to the selection redshift, using HBT-HERONS. We assess the effects of AGN feedback in the fiducial L200m6 simulation, which includes only a thermal model and contains 470 $z = 3$ MQGs (following the selection in § 3.1); and in the L200m7h simulation, which includes the hybrid (thermal+jet) model and contains 310 $z = 3$ MQGs. The results from these two simulations should be compared qualitatively, given their different mass resolutions and free parameter values in the calibration.

5.1 AGN feedback (selection time or “present”)

As a first step toward understanding the role of AGN feedback in MQGs, we calculate the cumulative energy injected by the most massive BH particle within the fiducial aperture (50 pkpc). The value $E_{\text{inj},\text{BH}} = \sum_{\text{event}} \Delta E_{\text{AGN}}$ is the cumulative sum over all the AGN feedback events associated with that BH particle. In the thermal simulation, this corresponds to the thermal energy deposited into gas particles within the BH’s smoothing kernel (accumulating the contribution from equation 5); in the hybrid simulation, this corresponds to thermal energy (as in the fiducial simulation) as well as kinetic energy from jets (accumulating the contributions from equations 5 and 8). Note that this does not include energy contributions from BHs that previously merged with this BH particle.

Fig. 9 shows the normalised histograms of the cumulative BH energy for MQGs (solid red curves) and MSFGs (solid grey curves) at $z = 3$. The top panel presents results for the thermal L200m6 simulation, while the bottom shows the hybrid L200m7h simulation. In both cases, the MQGs and MSFGs peak at different values: BHs in star-forming systems inject, on average, significantly less energy. In the thermal simulation, the median cumulative energy is $\approx 10^{59.8}$ erg for MQGs compared to $\approx 10^{58.9}$ erg for MSFGs, while in the hybrid simulation $\approx 10^{60.5}$ erg and $\approx 10^{59.4}$ erg, respectively. These differences reinforce the conclusion that AGN feedback drives quenching.

The hybrid case broadly resembles the thermal case, but the total (thermal+jet) energy for MQGs is larger. To assess the effect of the AGN feedback model independently of volume and resolution, we include the L200m7 simulation, which shows that the hybrid simulation still injects more feedback energy compared to the thermal AGN feedback run, which may appear contradictory since quenching is less efficient in the hybrid simulation (see Fig. 2). Note that there is more energy injection overall in the m7 resolution runs, though.

The cumulative BH-injected energy in the hybrid case consists of a combination of thermal plus kinetic jet energy ($E_{\text{inj},\text{BH}} = E_{\text{thermal}} + E_{\text{jet}}$). Vertical arrows mark the median thermal, $\text{med}(E_{\text{thermal}})$, and jet, $\text{med}(E_{\text{jet}})$, contributions, showing that the jet model dominates

⁷ SN feedback is not expected to quench galaxies in this massive regime (Benson et al. 2003), and the quenching timescales analysed in § 4.3.2 (with median values up to $t_q \approx 0.6$, Gyr) make this even less plausible. Although SN feedback can, in principle, inject a larger cumulative amount of energy (see fig. 14 in Huško et al. 2025a), the gas it affects experiences much stronger cooling losses, severely limiting its ability to halt star formation.

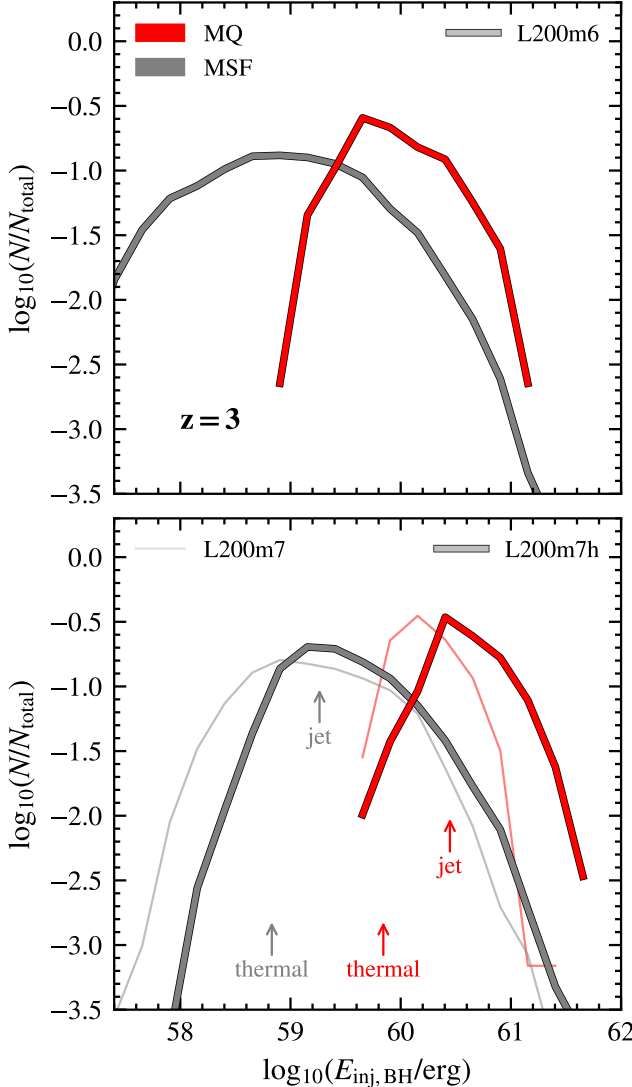


Figure 9. Normalised histogram of cumulative BH-injected energy for MQGs (red) and MSFGs (grey) at $z = 3$ in the fiducial L200m6 simulation (top panel) and the hybrid L200m7h simulation (bottom panel). Vertical arrows in the bottom panel mark the median contributions from the jet and thermal components in the hybrid case. Narrow solid lines in the background show the L200m7 results, included to illustrate the AGN feedback model effect.

both MQGs and MSFGs, while the thermal contribution falls below that of L200m7. This suggests that jets require longer timescales to quench galaxies, consistent with Appendix G. Furthermore, the appendix also shows that early feedback in the hybrid simulation limits BH growth compared to the thermal simulation, leading to weaker quenching at $z > 3$.

Table 2 shows the median energy contribution from each feedback model, split by accretion disc state (thick, thin, slim; see § 2.3.2). In all massive galaxies, the thin disc dominates, contributing over 90% of the injected energy. This is consistent with Huško et al. (2025a), who noted that the thin disc behaves similarly to the fiducial thermal model when $f_{\text{Edd}} < 0.3$ and thermal feedback then is dominant, since $\epsilon_{\text{acc}} = 1$ (see their table 1). However, in the regime $0.3 < f_{\text{Edd}} < 1$, jets dominate in the thin disc. In MQGs, 79% of the cumulative energy comes from the thin-disc jet model, compared to 70% in MSFGs. The thin-disc thermal contribution is also non-negligible.

Table 2. Energy contribution from each BH accretion disc state (thick, thin, or slim) or AGN feedback model (thermal or jet) in the hybrid L200m7h simulation for MQGs and MSFGs at $z = 3$. $\text{med}(E_i/E_{\text{inj,BH}})$ denotes the median ratio of each cumulative component E_i relative to the total BH-injected energy, $E_{\text{inj,BH}} = \sum_i E_i$.

property at $z = 3$ (L200m7h)	MQ	MSF
$\text{med}(E_{\text{thick,thermal}}/E_{\text{inj,BH}})$	0.00	0.00
$\text{med}(E_{\text{thin,thermal}}/E_{\text{inj,BH}})$	0.16	0.24
$\text{med}(E_{\text{slim,thermal}}/E_{\text{inj,BH}})$	0.04	0.03
$\text{med}(E_{\text{thick,jet}}/E_{\text{inj,BH}})$	0.00	0.02
$\text{med}(E_{\text{thin,jet}}/E_{\text{inj,BH}})$	0.79	0.70
$\text{med}(E_{\text{slim,jet}}/E_{\text{inj,BH}})$	0.00	0.00

Importantly, in $\approx 95\%$ of MQGs, the thin-disc jet model dominates the BH energy budget, peaking at $z \approx 3$ (Huško et al. 2025a). We find that $\approx 86\%$ of the quenched systems are still in that state at $z = 3$.

We find that there is a non-negligible population of active galaxies whose SMBHs inject large amounts of energy ($> 10^{60}$ erg) yet remain star-forming at $z = 3$. Tracking their descendants shows that in L200m6 (L200m7h), 33% (68%) quench by $z = 2$ and 57% (84%) by $z = 1$, excluding $\approx 16\%$ (7%) that disappear through mergers by $z = 2$ (they are not the main progenitor). There is also a fraction, 25% (8%), that were already quenched at $z = 3.5$ but experience a rejuvenation phase (more details about rejuvenation in § 5.3). These systems are therefore likely on the verge of quiescence or have undergone temporary rejuvenation. More isotropic inflows reducing feedback efficiency may also contribute, though exploring this further is beyond the scope of this paper.

Overall, we find a very tight correlation between quenching and AGN feedback in COLIBRE. This aligns with galaxy formation models such as Lagos et al. (2025b), which show that the AGN feedback prescription leaves clear imprints on MQG predictions. It also agrees with observations reporting AGN feedback signatures in MQGs (e.g. Davies et al. 2024; Stevenson et al. 2025; Baker et al. 2025c). In COLIBRE, AGN feedback drives outflows and shock-heats the intergalactic medium (IGM), suppressing gas cooling. This naturally explains the low molecular hydrogen reservoirs and reduced dust content arising from sputtering in hot gas (see fig. 9 in Schaye et al. 2025), as discussed in § 4.4.

We now turn to why some massive systems quench while others of similar mass remain star-forming.

5.2 Environment (pre-selection or “past”)

The fact that MQGs host BHs that release more energy relative to MSFGs raises the question of what is different between the two populations. Here we identify the origin of these differences. In this subsection, we present results for the thermal L200m6 simulation only, as the conclusions are unchanged for the hybrid L200m7h simulation (allowing for resolution effects).

5.2.1 BH masses and star formation efficiencies

We begin by examining the BH–stellar mass relation in the left panel of Fig. 10, focusing on the massive systems analysed in this section at $z = 3$ (MQGs and MSFGs). Scatter points are colour-coded by sSFR, showing that galaxies with more massive BHs tend to have lower sSFR values, consistent with AGN feedback driving quenching. The red and grey lines mark the median relations for

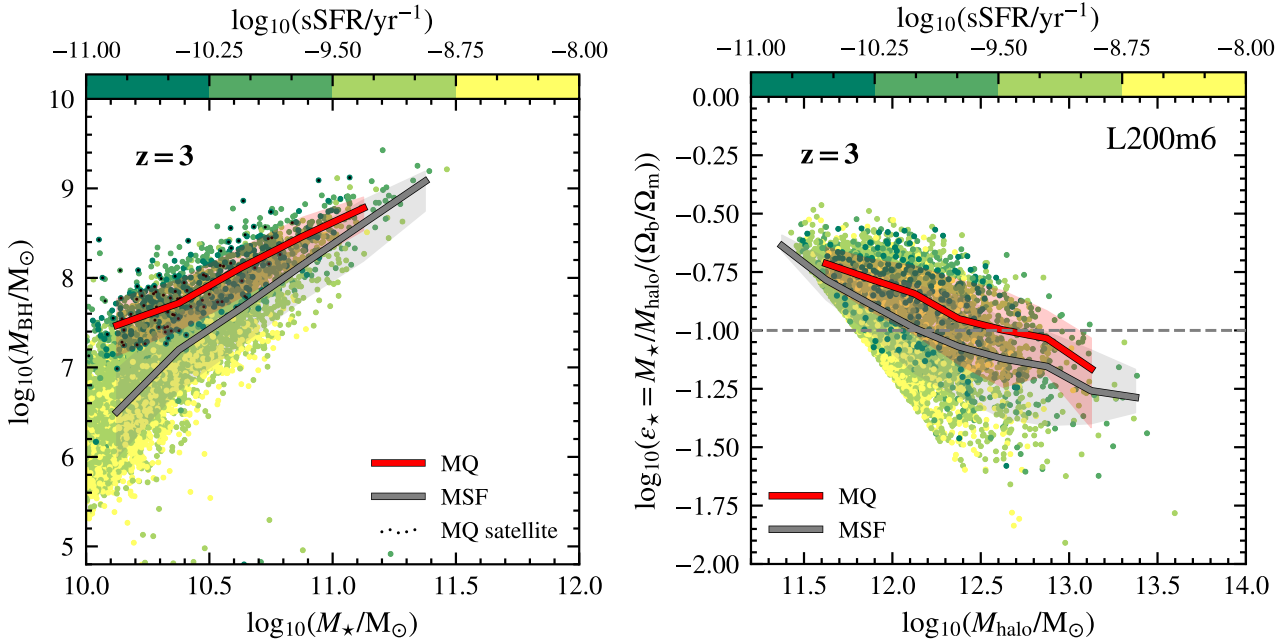


Figure 10. BH mass–stellar mass relation for all massive systems (left panel) and star formation efficiency, defined as $\varepsilon_{\star} = M_{\star}/M_{\text{halo}}/(\Omega_b/\Omega_m)$, versus halo mass (right panel) for central massive systems selected at $z = 3$ in L200m6. Scatter points are individual massive galaxies ($M_{\star} > 10^{10} M_{\odot}$), colour-coded by sSFR. Solid lines show the median values for MQGs (red) and MSFGs (grey), with shaded regions indicating the 16th and 84th percentile range. In the right panel, the dashed horizontal line marks a reference value of 10% star formation efficiency. Satellite MQGs are marked with black dots in the left panel.

MQGs and MSFGs, respectively, with shaded regions indicating the scatter. Passive systems clearly host more massive BHs, which in turn inject more feedback energy, as expected from the prescriptions in § 2.3.1 and § 2.3.2. In these models, the injected energy, whether in the form of a temperature increase (equation 6) or velocity kick (equation 9), scales with BH mass (equations 5 and 8). This trend is also evident in Appendix F2 for MQGs and can be extended to MSFGs as well. Satellite MQGs (marked with black dots) host BHs with masses that lie predominantly above the MSF median, indicating that these systems are likewise quenched by BH physics (AGN feedback) rather than by environmental effects.

Unlike other models, such as ILLUSTRIS-TNG (Kurinchi-Vendhan et al. 2024), where kinetic feedback is triggered once the Eddington ratio (a BH mass–dependent quantity) falls below a threshold, COLIBRE does not impose a transition BH mass for AGN activity. Observationally, BH masses in high- z quiescent systems remain difficult to constrain, although first estimates have emerged (e.g. Carnall et al. 2023b; Ito et al. 2025a), making our predictions a useful benchmark for future surveys.

The right panel of Fig. 10 shows the star formation efficiency, defined as $\varepsilon_{\star} = M_{\star}/M_{\text{b}}$ with $M_{\text{b}} = (\Omega_b/\Omega_m) \times M_{\text{halo}}$, versus halo mass for only central massive systems. Scatter points are again colour-coded by sSFR, with a dashed line marking 10% efficiency for reference. Galaxies with lower sSFR generally display higher efficiencies, indicating that quenched systems have been more effective at converting available gas into stars. By splitting the sample into MQGs and MSFGs, we see that MQGs are more efficient on average. Efficiency decreases with increasing halo mass. In COLIBRE, MQG efficiencies remain below the $\gtrsim 30\%$ values inferred from some spectroscopic studies (Carnall et al. 2024; Glazebrook et al. 2024), although these have been reported to decrease to $\sim 10\%$ once environmental effects are considered (Jespersen et al. 2025). Our MQG efficiencies, however, are consistent with other theoretical predic-

tions (Lagos et al. 2025b). Higher efficiencies might be achieved if measured before the quenching epoch (considering all progenitors), since the efficiency can only decrease as stellar mass growth stalls.

Taken together, the results in Fig. 10 highlight systematic differences at the selection redshift: MQGs host more massive BHs and have higher SF efficiencies than MSFGs. The key question is, therefore, what drives BHs to become more massive, or efficiencies to be higher, in MQGs. To answer this, we next trace the evolutionary histories of both populations using their main progenitors.

5.2.2 Evolutionary histories of MQGs

Fig. 11 shows the past evolution of several galaxy properties in look-back time, starting from the selection redshift $z = 3$ backwards until $z = 20$. To avoid biases when comparing MQGs and MSFGs and to ensure a truly stellar mass–matched sample, since MQGs are typically more massive, we restrict the sample to galaxies within the $10^{10.4} < M_{\star}/M_{\odot} \leq 10^{10.8}$ bin. The results remain unchanged when selecting a different stellar mass bin (e.g. $10^{10.0} < M_{\star}/M_{\odot} \leq 10^{10.4}$ or $10^{10.8} < M_{\star}/M_{\odot} \leq 10^{11.8}$).

The first row presents the evolution of BH mass, BH-injected energy, and the outflow mass rate of cool gas at R_{200c} (for central galaxies only). The second row shows the star formation efficiency (central galaxies only), BH accretion rate (BHAR) averaged over 100 Myr, and the inflow mass rate of cool gas at $0.3 R_{200c}$ (central galaxies only). Median values are shown for MQGs (red) and MSFGs (grey), with shaded regions indicating the scatter. The vertical line marks the median quenching timescale t_q , as defined in § 3.2. The mass flow rates are computed as described in § 3, focusing on cool gas with temperatures $10^3 \text{ K} < T_{\text{gas}} < 10^5 \text{ K}$, since this is the dominant component. It traces both the cold streams that supply inflows to galaxies and the possible neutral/ionised outflows reported

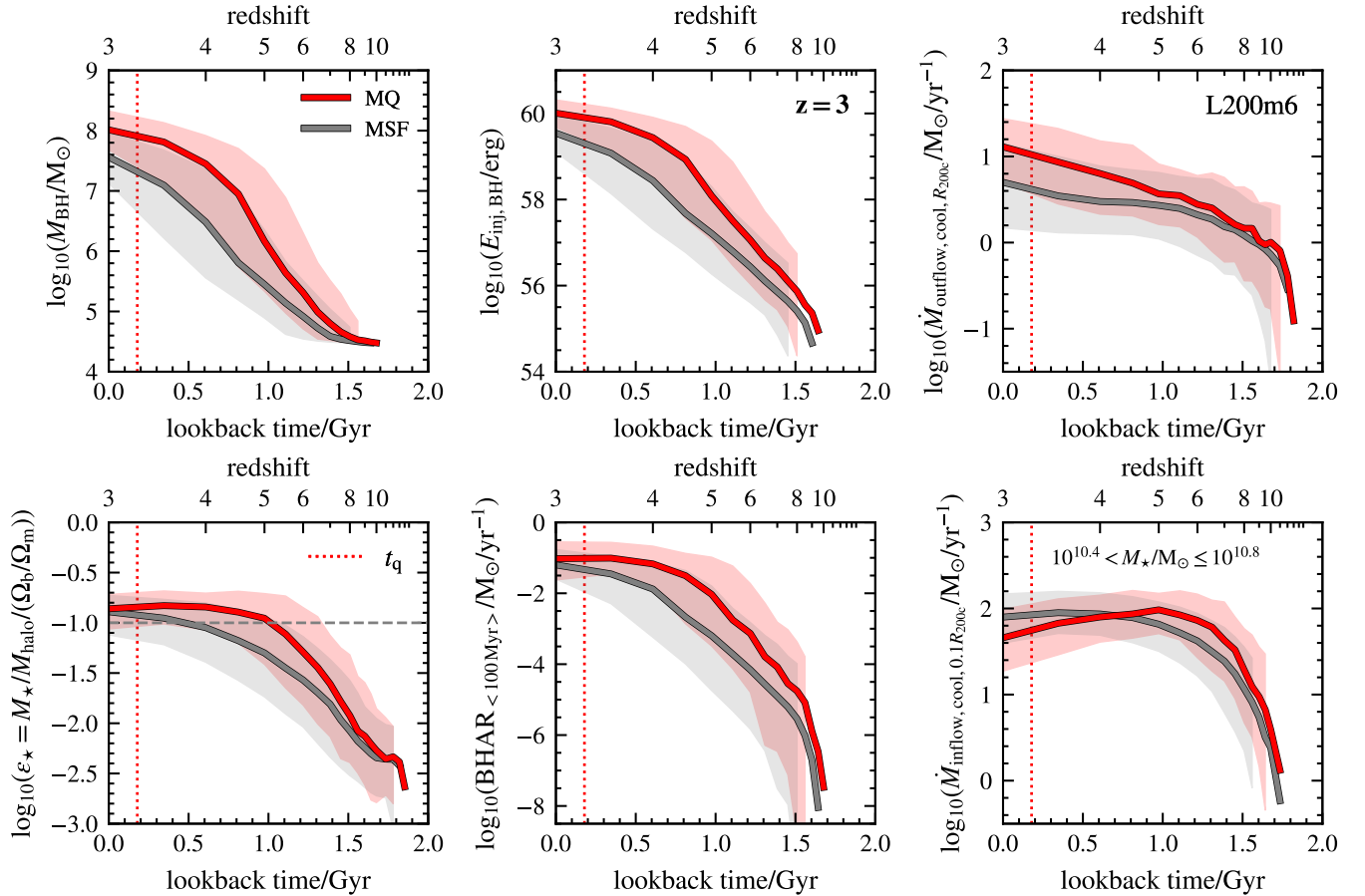


Figure 11. Evolution of BH- and galaxy-related properties as a function of lookback time (with redshift indicated by the top x -axis) for galaxies with $10^{10.4} < M_\star / M_\odot \leq 10^{10.8}$. Top row: BH mass (left) cumulative BH-injected energy (middle), and outflow rate of cool gas ($10^3 \text{ K} < T_{\text{gas}} < 10^5 \text{ K}$) at R_{200c} only for central galaxies (right). Bottom row: star formation efficiency, $\epsilon_\star = M_\star / M_{\text{halo}} / (\Omega_b / \Omega_m)$ only for central galaxies (left), BH accretion rate averaged over 100 Myr (middle), and inflow rate of cool gas ($10^3 \text{ K} < T_{\text{gas}} < 10^5 \text{ K}$) at $0.1 R_{200c}$ only for central galaxies (right). Solid lines show the median values for MQGs (red) and MSFGs (grey) selected as in § 3.1 at $z = 3$, with shaded regions indicating the 16th and 84th percentile range. The vertical red dotted line marks the median quenching timescale, t_q , of the MQGs. In the bottom left panel, the dashed horizontal line marks a reference value of 10% star formation efficiency.

observationally (e.g. D'Eugenio et al. 2024). The main conclusions from these panels are:

- **BH mass:** MQG BHs are seeded slightly earlier, reflecting their host FOF/haloes being slightly more massive (§ 2.3). They also grow at a much faster rate for $z \lesssim 8$. The earlier seeding and faster growth of BHs in quenched systems is consistent with the behaviour reported in Kurinchi-Vendhan et al. (2024).

- **BH-injected energy:** following the same trend, MQGs inject more energy on average (§ 5.1). This is consistent with the expectation that AGN energy drives their quenching, which is captured in the COLIBRE feedback prescription (§ 2.3).

- **Outflowing mass rate:** we trace the gas outflowing at R_{200c} , which we use to define the halo boundary. This allows us to track material expelled from the halo. As MQG BHs grow more massive and inject more energy, they drive stronger outflows, particularly by $z \lesssim 6$. These powerful outflows, driven by the AGN, suppress the local cooling rate of the circumgalactic medium (CGM) and contribute to quenching. They are also the primary mechanism for heating and removing the galaxy's gas reservoir, which directly leads to the low molecular hydrogen and dust fractions discussed in § 4.4.

- **Star formation efficiency (ϵ_\star):** MQGs reach higher efficiencies, remaining above the 10% reference value for longer (for main

progenitors at least). Efficiencies are higher before the quenching event and decline afterwards as stellar mass growth saturates.

- **BHAR:** we employ a 100 Myr time-averaged BHAR, which smoothes over the short timescale fluctuations in the instantaneous value. The shapes of the curves mirror those of the BH-injected energy evolution, with MQGs offset earlier due to earlier seeding. Importantly, BHAR typically peaks before quenching, after which accretion reaches a plateau or drops. This is as we would expect: rapid accretion triggers stronger feedback, which quenches the system by driving outflows and heating the surrounding gas, suppressing further efficient accretion. A similar feature is reported in FLARES, a set of zoom-ins using the EAGLE model (Lovell et al. 2023).

- **Inflowing mass rate:** we trace the gas inflowing at $0.1 R_{200c}$, which is expected to follow cold streams feeding the galaxy, though it may also include some recycled gas from feedback (Mitchell et al. 2020; Wright et al. 2024a). MQGs initially show larger inflows of cool material, but once their BHs become sufficiently powerful, these inflows decline, falling below those of MSFGs. This prevents replenishment of the gas reservoir and reinforces quiescence as a direct consequence of AGN heating and gas expulsion. As these are mass-matched samples, we might expect their median values to cross over at some point in the past.

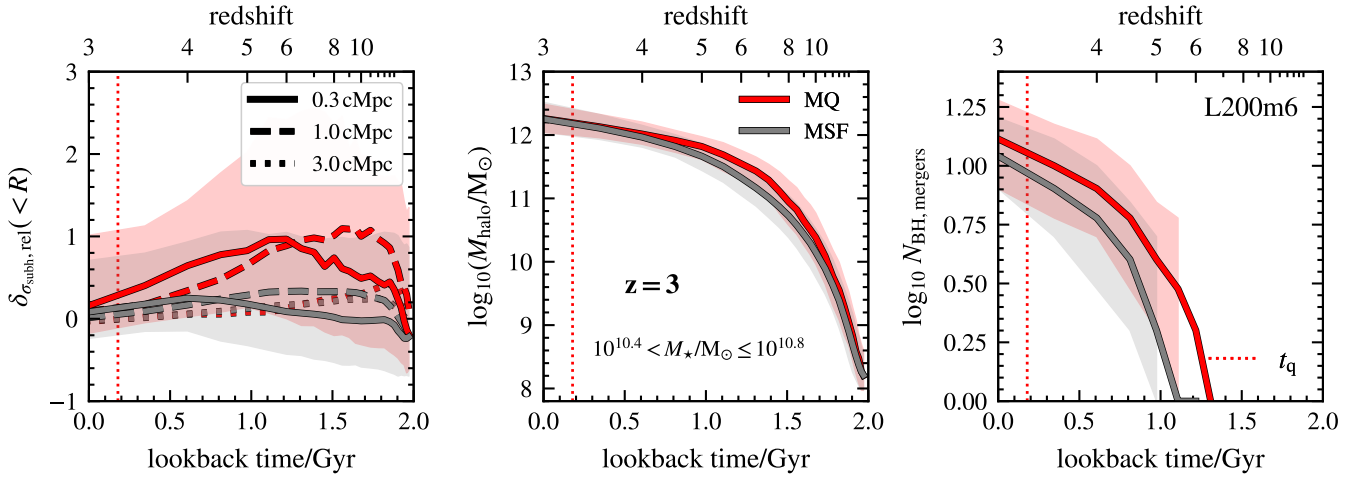


Figure 12. Evolution of environment-related galaxy properties as a function of lookback time (with redshift indicated by the top x -axis) for galaxies with $10^{10.4} < M_*/M_\odot \leq 10^{10.8}$. $\delta_{\sigma_{\text{subh,rel}}(< R)}$ deviation from the mean subhalo density contrast, as defined in § 3.4, in a sphere of radius $R = 0.3, 1$ or 3.0 cMpc (left panel); halo mass only for central galaxies (middle panel); and number of BH mergers (right panel). Solid lines show the median values for MQGs (red) and MSFGs (grey) selected as in § 3.1 at $z = 3$, with shaded regions indicating the 16th and 84th percentile range (for the left panel, this shading corresponds only to the $R = 0.3 \text{ cMpc}$ curves). The vertical red dotted line marks the median quenching timescale, t_q , of the MQGs.

Our results make clear that the evolutionary histories of MQGs and MSFGs diverge between $z = 3$ and earlier times: quiescent systems host more massive, energetic BHs and achieve higher stellar-to-halo mass ratios due to greater early accretion of cool gas. This raises the question of what drives the differences in the first place.

5.2.3 Environment shaping MQGs

We examine the environment and merger history of MQGs in Fig. 12. The environment is characterised by $\delta_{\sigma_{\text{subh,rel}}(< R)}$, the deviation from the mean subhalo density contrast in different spherical apertures (0.3, 1.0, or 3.0 cMpc) introduced in § 3.4, and by the halo mass. The merger history is traced by the number of BH mergers, which serve as a ‘proxy’ for mergers, since, by construction, these only occur when both merging galaxies are massive enough to host seeded BHs (§ 2.3). These three tracers (subhalo density contrast, halo mass, and mergers) correlate as shown in Appendix F2 for MQGs, with this correlation extending to MSFGs as well.

Fig. 12 shows that MQGs typically reside in slightly more overdense regions than MSFGs at the selection time, but they occupied markedly more overdense areas before that ($z \gtrsim 4$ in this case), particularly on local (0.3 cMpc, halo) and intermediate (1.0 cMpc, local cosmic web) scales, with some tendency towards more overdense environments even on larger scales (3.0 cMpc) at very early times. The environmental differences are significant beyond $z \gtrsim 4$ but smooth out by the selection time, being more pronounced at larger scales the earlier we consider. This likely reflects our use of a subhalo density contrast, highlighting that these neighbouring subhalos are eventually accreted. Plus, rather than being the primary quenching mechanism, the higher merger rate in MQGs is another consequence of their dense environment, serving to accelerate mass assembly triggering star formation bursts and potentially fueling the rapid BH growth that ultimately powers quenching feedback, consistent with observational evidence that merger fractions increase with local density at such high redshifts (Shibuya et al. 2025). Moreover, although mergers are more common in MQGs, they do not produce morphological differences between MQGs and MSFGs (§ 4.6).

Overall, MQGs are more likely to reside in overdense regions,

particularly at earlier times in their evolutionary history. Their early position within the cosmic web and host halo masses imply deeper potential wells and stronger gas inflows, fuelling both star formation and BH accretion. This, in turn, enables higher stellar masses, faster SMBH growth, and ultimately more powerful feedback, producing outflows that quench them more efficiently. These are the trends evident in Fig. 12.

The correlation between environment and quenching has been widely reported in the literature. For instance, Kurinchi-Vendhan et al. (2024) find in ILLUSISTRIS-TNG that large-scale structure plays a key role in setting galaxy evolutionary paths, a result also seen in ASTRID (Weller et al. 2025). In THESAN, which includes radiative transfer and enhanced BH growth, Chittenden et al. (2025) show that MQGs exhibit faster BH accretion and stronger environmental imprints, especially on small to intermediate scales, consistent with our COLIBRE results. Similarly, Szpila et al. (2025) report that MQGs in SIMBA-C occupy more overdense regions at earlier times, before the selection, which enhances the efficiency of feedback coupled with early and rapid BH growth. However, by the selection time, they are found in less dense environments than their massive star-forming counterparts, because in their model, powerful kinetic jets that quench the galaxy require low BH accretion rates, which only occur when the surrounding environment is not too dense. We note that Kimmig et al. (2025) find the opposite trend: MQGs occupy less overdense regions, particularly at local scales, even before selection. These systems form in local, rather than global, nodes associated with weaker filaments, which AGN feedback can easily disrupt.

Observational constraints remain sparse, but emerging results suggest a consistent picture of MQGs residing in overdense environments (Jin et al. 2024; Ito et al. 2025b; de Graaff et al. 2025; Kawinwanichakij et al. 2025; Baker et al. 2025b; McConachie et al. 2025), with the caveat that this observed trend will be influenced by survey biases, which target overdense regions.

5.3 Rejuvenation (post-selection or “future”)

The final stage of our journey to understand the physical drivers that shape MQGs focuses on examining their future evolution, a

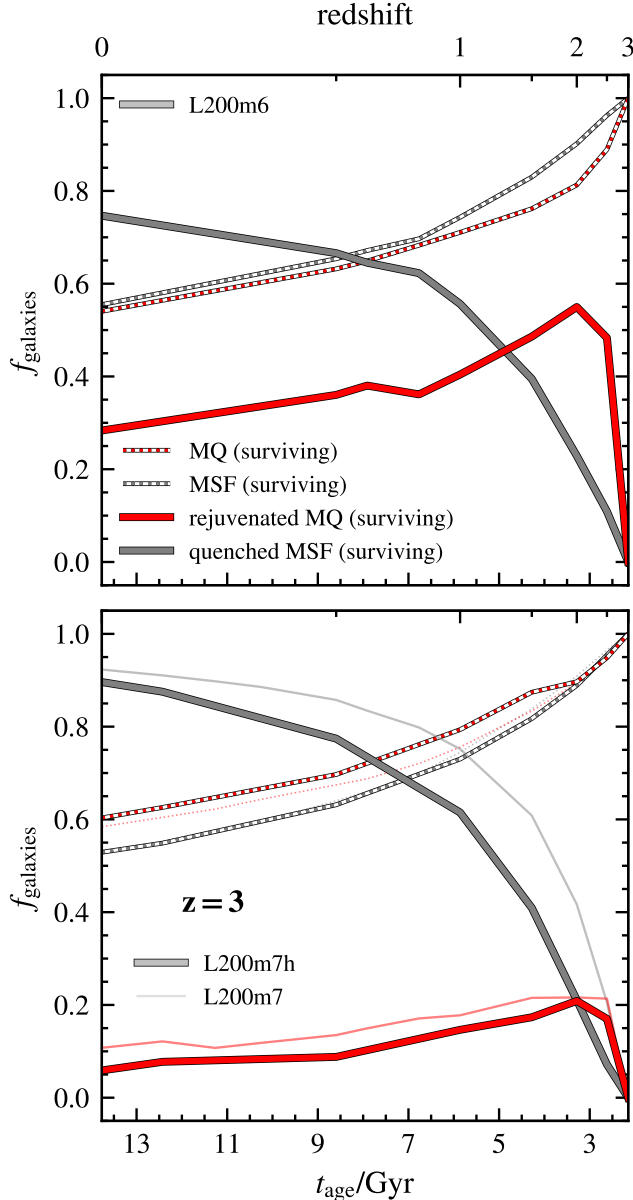


Figure 13. Evolution of the number fraction of galaxies as a function of the age of the Universe from $z = 3$ to $z = 0$ (redshift by the top x -axis). Solid red lines show galaxies that are MQGs at $z = 3$ and subsequently rejuvenate (they are star forming at the given time on the x -axis), while solid grey lines show galaxies that are MSFGs at $z = 3$ and later quench (they are quenched). Dotted red and grey lines indicate galaxies whose main progenitors are the MQGs and MSFGs selected at $z = 3$, respectively. Results are shown for the thermal L200m6 simulation (top panel) and the hybrid L200m7h simulation (bottom panel). Narrow solid lines in the background show the L200m7 results, included to illustrate the AGN feedback model effect.

prediction that is possible in simulations but not in observations. We analyse some properties of the main descendants from HBT-HERONS of all the MQGs and MSFGs (without applying any stellar mass binning) in Fig. 13, where we look at the number fraction of galaxies as a function of the age of the Universe. We compare results from the thermal L200m6 simulation (top panel) with those from the hybrid L200m7h simulation (bottom panel).

5.3.1 Number fraction of surviving main progenitors

First, we consider the number fraction of passive systems selected at $z = 3$ that survive as main descendants; that is, galaxies that have not merged. This fraction is shown in Fig. 13 as a red dotted line. By $z = 0$, around 55% of these systems are still detected in the simulation (either as centrals or satellites). The numbers are similar for MSFGs, shown with grey dotted lines. This large fraction of galaxies without experiencing mergers is consistent with the inside-out growth scenario, where systems grow primarily through minor mergers until $z = 0$, eventually becoming the elliptical galaxies observed locally (Bezanson et al. 2009). 67% (71%) of MQG descendants at $z = 0$ are central galaxies in the thermal (hybrid) simulation. Future work will investigate whether these correspond to the brightest cluster galaxies. The thermal and hybrid simulations produce broadly similar results in terms of how these systems survive down to $z = 0$.

Comparisons with other simulations show some variation, considering the different ‘massive quenched’ selection criteria. In ILLUSTRIS-TNG, Hartley et al. (2023) report that only 1 galaxy out of five selected MQGs at $z \approx 4.2$ in TNG300 has a main descendant that survives to $z = 0$ (20%). Weller et al. (2025) find $\approx 60\%$ at $z = 0$, with 30% identified as brightest cluster galaxies when selecting the sample at $z = 3$ in TNG100 and TNG300. These values are broadly consistent with the survival fraction we find in COLIBRE, given the comparable trends in terms of environment (§ 5.2). However, in the MAGNETICUM simulations, Remus & Kimmig (2025) report that by $z = 2$, $\approx 20\%$ of MQGs selected around $z = 3$ are accreted onto more massive structures (either as satellite galaxies or by having merged).

5.3.2 Number fraction of rejuvenated galaxies

We also investigate in Fig. 13 rejuvenation events. We compute the number fraction of quenched systems at $z = 3$ that temporarily exceed the sSFR threshold defined in § 3.1 at a given redshift $z < 3$, relative to those that survive at each redshift (not having merged). Rejuvenation peaks around 55% at $z = 2$ for the thermal L200m6 simulation, compared to only around 20% for the hybrid L200m7h. Initially, it takes ≈ 1 Gyr for the ISM to sustain star formation again in some systems, leading to an increase in the rejuvenation fraction from $z = 3$ to $z = 2$. Later, in these systems, presumably cooling and renewed gas inflow allow temporary star formation. However, BHs eventually re-establish strong feedback, reducing the rejuvenation fraction (increasing quenching) again from $z = 2$ to $z = 0$. Although we do not quantify this hypothesis nor the role of mergers in supplying gas for star formation, rejuvenated galaxies generally host lower-mass BHs, indicating weaker quenching that allows star formation to resume temporarily. In massive systems, strong BH feedback ultimately ensures most descendants remain quiescent as can be seen from the increasing fraction of MSFGs selected at $z = 3$ that quench with time by $z < 3$ (solid grey lines). The hybrid simulation results broadly follow those of L200m7 (background lines), pointing to the AGN feedback model effect analysed previously (§ 4.1.1): AGN feedback is stronger and burstier in the m7 resolution runs, preventing star formation from resuming. That explains why more MSFGs quench by $z = 0$ as well (solid grey line).

These trends are broadly consistent with other galaxy formation models (considering the different MQ selection; Szpila et al. 2025; Weller et al. 2025; Remus & Kimmig 2025), although they typically report slightly lower rejuvenation fractions ($\approx 30\%$ at $z \gtrsim 2$, dropping to $< 5\%$ at lower redshift); this is likely due to stronger AGN feedback. Observationally, as explained before, detecting rejuvenation features in possible MQGs descendants is difficult because the

SED-fitting process struggles to recover such features in SFHs, although some evidence exists from local counterparts (Yi et al. 2005).

6 CONCLUSIONS

We have analysed predictions from the new COLIBRE hydrodynamical simulations in its multiple volumes, resolutions, and AGN feedback models for the population of Massive Quiescent Galaxies (MQGs; defined as galaxies with $M_\star > 10^{10} M_\odot$ and $\text{sSFR} < 0.2/t_{\text{age}}$) at high-redshift ($z \gtrsim 2$). Recent *JWST* surveys have suggested that MQGs are more abundant than previously observed. Given the poorly understood nature of these MQGs and current observational limitations, we investigated what the state-of-the-art COLIBRE galaxy formation model predicts for a wide range of their properties. Our main findings are as follows:

(i) **Number densities:** We studied how MQG number densities change across the COLIBRE simulations (§ 4.1.1). We find a clear resolution effect: higher-resolution runs produce less quenching; while the hybrid AGN feedback model yields even fewer quenched systems, underpredicting the observational estimates. The fiducial L200m6 simulation yields results broadly consistent with the most recent and robust observational estimates (those covering larger areas or larger spectroscopic samples), especially after we include uncertainties to the simulation values that exemplify observational uncertainties. Compared to most galaxy formation models that also reproduce observations at $z = 0$, COLIBRE predicts higher number densities (Fig. 3).

(ii) **Stellar mass functions:** MQG stellar mass functions in COLIBRE agree with the latest observations when uncertainties are considered, and outperform other models (Fig. 4).

(iii) **Star formation histories:** MQGs show good qualitative agreement with observationally inferred SFHs (§ 4.3), with extended formation times (median $t_{50} \approx 0.5\text{--}1.5$ Gyr), rapid quenching (median $t_q \lesssim 0.6$ Gyr), and evidence of strong starbursts.

(iv) **Dust and molecular hydrogen:** With its explicit modelling of dust and a cold ISM phase, COLIBRE predicts that MQGs have much lower dust and molecular hydrogen fractions (medians $f_{\text{dust}} \sim 10^{-4}$ and $f_{\text{H}_2} \sim 10^{-2.5}$) than massive star-forming counterparts, with no evidence for dust regrowth (§ 4.4). Although current observations are limited in sample size and biased toward dust- and gas-rich systems, they generally agree with these predictions, with only a few cases showing very high dust fractions (Fig. 6).

(v) **Sizes and kinematics:** MQG sizes (in terms of the half-mass radius) and kinematics are broadly similar to those of coeval MSFGs (Fig. 8), suggesting a decoupling between quenching and morphological transformation at $z \gtrsim 2$, with the latter likely driven by subsequent mergers given the subtle signs of increased dispersion support by $z \approx 2$.

Secondly, to understand how MQGs assemble mass and quench so early in the COLIBRE model, we traced their evolutionary histories, focusing on galaxies selected at $z = 3$. Our key conclusions are:

- **AGN feedback drives quenching:** Both thermal and hybrid (thermal+jet) AGN feedback models quench MQGs (§ 5.1). Hybrid feedback produces less quenching due mainly to a slower BH growth, while the modelled jets take longer to impact the galaxy and initiate quenching. This clearly highlights that the timing and power of early AGN feedback are critical for rapid quenching.

- **Environment matters:** MQGs inhabit overdense regions, particularly before the selection time (§ 5.2); enabling earlier gas accre-

tion, BH growth and more powerful AGN feedback. This explains their accelerated evolution and enhanced star formation efficiencies.

- **Rejuvenation:** Rejuvenation episodes are common, peaking at $z \approx 2$ with up to 55% of MQGs experiencing renewed star formation in the thermal AGN feedback simulation and 20% in the hybrid AGN feedback simulation (§ 5.3). About 55% of MQGs survive as the main progenitors of $z = 0$ galaxies.

Taken together, the comparison between COLIBRE and current observations shows encouraging qualitative and often quantitative agreement across a wide range of properties. Although systematic differences remain, likely in some part attributable to observational uncertainties, sample selection, and measurement techniques; the level of tension previously reported between models and observations has decreased. We conclude that this convergence reflects progress in both simulations and observations. This also highlights the need for more accurate modelling of the physical processes that shape MQGs, as well as larger, deeper spectroscopic samples to further reduce systematics. We note that this observational field is rapidly evolving, so measurements may continue to change. Closing this gap will be key to advancing our understanding of the earliest quenched galaxies and their role in galaxy evolution.

Several caveats must be considered. From the simulation side, galaxy formation models are calibrated in the local Universe, and results at high- z remain sensitive to choices in e.g. AGN feedback modelling and uncertain parameters tied to BH physics, relevant for MQGs (Lagos et al. 2025b; Huško et al. 2025a). From the observational side, caveats related to sample selection, wavelength coverage, and measurement techniques (discussed throughout this paper) must be borne in mind when interpreting results. Nevertheless, when these factors are accounted for, this work provides robust predictions within the COLIBRE model for the population of MQGs, offering insights into the physical mechanisms that shape their origin and evolution, and in the process easing the tension between observations and simulations. Its predictions also offer guidance for upcoming surveys, given current observational limitations.

Looking ahead, COLIBRE opens several promising avenues for follow-up studies. One direction is to further investigate the connection between the halo assembly and MQG evolution. Predictions for galaxy clustering will also be valuable, as they can help establish links between MQGs and potential progenitor populations, such as highly star-forming galaxies. Upcoming observations leveraging the synergy of *JWST* and ALMA will allow detailed characterisation of the stellar populations and clustering of both populations, providing a way to test these connections (Long et al. 2023; Bodansky et al. 2025). Moreover, MQGs may also be linked to other high- z populations probed by *JWST*, including early massive galaxies at $z \gtrsim 7$ (Baggen et al. 2023) or the so-called ‘‘little red dots’’ (Kokorev et al. 2024), as well as to descendant populations such as the most massive elliptical galaxies in the local Universe or the rare class of compact, massive early-type ‘‘relic’’ galaxies (Hartmann et al. 2025). Additional work could test metallicity predictions, including recently observed α -enhancement signatures (Antwi-Danso et al. 2023).

ACKNOWLEDGEMENTS

ACG acknowledges Research Training Program and ICRAR scholarships. ACG acknowledges support for this project by the University of Western Australia via a Research Collaboration Award. This work used the DiRAC@Durham facility managed by the Institute for Computational Cosmology on behalf of the STFC DiRAC HPC Facility

(www.dirac.ac.uk). The equipment was funded by BEIS capital funding via STFC capital grants ST/K00042X/1, ST/P002293/1, ST/R002371/1 and ST/S002502/1, Durham University and STFC operations grant ST/R000832/1. DiRAC is part of the National e-Infrastructure. This project has received funding from the Netherlands Organization for Scientific Research (NWO) through research programme Athena 184.034.002. WMB would like to acknowledge support from DARK via the DARK Fellowship. This work was supported by a research grant (VIL54489) from VILLUM FONDEN. ABL acknowledges support by the Italian Ministry for Universities (MUR) program “Dipartimenti di Eccellenza 2023-2027” within the Centro Bicocca di Cosmologia Quantitativa (BiCoQ), and support by UNIMIB’s Fondo Di Ateneo Quota Competitiva (project 2024-ATEQC-0050). SP acknowledges support by the Austrian Science Fund (FWF) through grant-DOI: 10.55776/V982. JT acknowledges support of a STFC Early Stage Research and Development grant (ST/X004651/1). Minor typos, grammar and spelling mistakes were identified with the assistance of ChatGPT-4o⁸ when preparing this document. No passages of text or structural outlines for this paper were created with the help of any large language models.

DATA AVAILABILITY

The data underlying this article will be provided upon reasonable request to the corresponding author.

REFERENCES

Abbott T. M. C., et al., 2022, *Phys. Rev. D*, **105**, 023520
 Adamo A., et al., 2025, *Nature Astronomy*, **9**, 1134
 Adscheid S., Magnelli B., Ciesla L., Liu D., Schinnerer E., Bertoldi F., 2025, *arXiv e-prints*, p. [arXiv:2508.18097](https://arxiv.org/abs/2508.18097)
 Alberts S., et al., 2024, *ApJ*, **975**, 85
 Antwi-Danso J., et al., 2023, Is there Evidence of alpha-Enhancement in Massive Quiescent Galaxies at $z > 3$?, JWST Proposal. Cycle 2, ID. #4318
 Aoyama S., Hou K.-C., Shimizu I., Hirashita H., Todoroki K., Choi J.-H., Nagamine K., 2017, *MNRAS*, **466**, 105
 Baggen J. F. W., et al., 2023, *ApJ*, **955**, L12
 Bahé Y. M., et al., 2022, *MNRAS*, **516**, 167
 Baker W. M., et al., 2025a, *arXiv e-prints*, p. [arXiv:2506.04119](https://arxiv.org/abs/2506.04119)
 Baker W. M., et al., 2025b, *arXiv e-prints*, p. [arXiv:2509.09761](https://arxiv.org/abs/2509.09761)
 Baker W. M., et al., 2025c, *MNRAS*, **539**, 557
 Baker W. M., et al., 2025d, *A&A*, **697**, A90
 Barausse E., Morozova V., Rezzolla L., 2012, *ApJ*, **758**, 63
 Bell E. F., de Jong R. S., 2001, *ApJ*, **550**, 212
 Belli S., Newman A. B., Ellis R. S., 2017, *ApJ*, **834**, 18
 Bellstedt S., Robotham A. S. G., 2025, *MNRAS*, **540**, 2703
 Benítez-Llambay A., et al., 2025, *arXiv e-prints*, p. [arXiv:2509.25309](https://arxiv.org/abs/2509.25309)
 Benson A. J., Bower R. G., Frenk C. S., Lacey C. G., Baugh C. M., Cole S., 2003, *ApJ*, **599**, 38
 Bezanson R., van Dokkum P. G., Tal T., Marchesini D., Kriek M., Franx M., Coppi P., 2009, *ApJ*, **697**, 1290
 Bodansky S., et al., 2025, *arXiv e-prints*, p. [arXiv:2507.19472](https://arxiv.org/abs/2507.19472)
 Bondi H., 1952, *MNRAS*, **112**, 195
 Booth C. M., Schaye J., 2009, *MNRAS*, **398**, 53
 Borrow J., Schaller M., Bower R. G., Schaye J., 2022, *MNRAS*, **511**, 2367
 Bower R. G., Benson A. J., Malbon R., Helly J. C., Frenk C. S., Baugh C. M., Cole S., Lacey C. G., 2006, *MNRAS*, **370**, 645
 Boylan-Kolchin M., 2023, *Nature Astronomy*, **7**, 731
 Buitrago F., Trujillo I., Conselice C. J., Bouwens R. J., Dickinson M., Yan H., 2008, *ApJ*, **687**, L61
 Calzetti D., Armus L., Bohlin R. C., Kinney A. L., Koornneef J., Storchi-Bergmann T., 2000, *ApJ*, **533**, 682
 Cappellari M., 2016, *ARA&A*, **54**, 597
 Carnall A. C., McLure R. J., Dunlop J. S., Davé R., 2018, *MNRAS*, **480**, 4379
 Carnall A. C., et al., 2023a, *MNRAS*, **520**, 3974
 Carnall A. C., et al., 2023b, *Nature*, **619**, 716
 Carnall A. C., et al., 2024, *MNRAS*, **534**, 325
 Chabrier G., 2003, *PASP*, **115**, 763
 Chaikin E., Schaye J., Schaller M., Bahé Y. M., Nobels F. S. J., Ploeckinger S., 2022, *MNRAS*, **514**, 249
 Chaikin E., Schaye J., Schaller M., Benítez-Llambay A., Nobels F. S. J., Ploeckinger S., 2023, *MNRAS*, **523**, 3709
 Chaikin E., et al., 2025a, *arXiv e-prints*, p. [arXiv:2509.04067](https://arxiv.org/abs/2509.04067)
 Chaikin E., et al., 2025b, *arXiv e-prints*, p. [arXiv:2509.07960](https://arxiv.org/abs/2509.07960)
 Chandro-Gómez Á., et al., 2025, *MNRAS*, **539**, 776
 Chang W., et al., 2025, *arXiv e-prints*, p. [arXiv:2508.08460](https://arxiv.org/abs/2508.08460)
 Chittenden H. G., Glazebrook K., Nanayakkara T., Kawinwanichakij L., Lagos C., Kimmig L., Remus R.-S., 2025, *arXiv e-prints*, p. [arXiv:2504.19696](https://arxiv.org/abs/2504.19696)
 Cochrane R. K., Katz H., Begley R., Hayward C. C., Best P. N., 2025, *ApJ*, **978**, L42
 Conroy C., 2013, *ARA&A*, **51**, 393
 Conroy C., Gunn J. E., White M., 2009, *ApJ*, **699**, 486
 Crain R. A., van de Voort F., 2023, *ARA&A*, **61**, 473
 Crain R. A., et al., 2015, *MNRAS*, **450**, 1937
 Croton D. J., et al., 2006, *MNRAS*, **365**, 11
 Cutler S. E., et al., 2022, *ApJ*, **925**, 34
 D’Eugenio F., et al., 2024, *Nature Astronomy*, **8**, 1443
 Dalla Vecchia C., Schaye J., 2012, *MNRAS*, **426**, 140
 Davé R., Anglés-Alcázar D., Narayanan D., Li Q., Rafieferantsoa M. H., Appleby S., 2019, *MNRAS*, **486**, 2827
 Davies R. L., et al., 2024, *MNRAS*, **528**, 4976
 De Lucia G., Fontanot F., Xie L., Hirschmann M., 2024, *A&A*, **687**, A68
 Dehnen W., 2014, *Computational Astrophysics and Cosmology*, **1**, 1
 Dekel A., Zolotov A., Tweed D., Cacciato M., Ceverino D., Primack J. R., 2013, *MNRAS*, **435**, 999
 Dell’Agli F., García-Hernández D. A., Schneider R., Ventura P., La Franca F., Valiante R., Marini E., Di Criscienzo M., 2017, *MNRAS*, **467**, 4431
 Di Matteo T., Springel V., Hernquist L., 2005, *Nature*, **433**, 604
 Donevski D., et al., 2023, *A&A*, **678**, A35
 Driver S. P., et al., 2022, *MNRAS*, **513**, 439
 Dwek E., 1998, *ApJ*, **501**, 643
 Faisst A. L., Chen C.-C., Ciesla L., Gruppioni C., 2025, *arXiv e-prints*, p. [arXiv:2509.01674](https://arxiv.org/abs/2509.01674)
 Falcón-Barroso J., Sánchez-Blázquez P., Vazdekis A., Ricciardelli E., Cardiel N., Cenarro A. J., Gorgas J., Peletier R. F., 2011, *A&A*, **532**, A95
 Forouhar Moreno V. J., Helly J., McGibbon R., Schaye J., Schaller M., Han J., Kugel R., Bahé Y. M., 2025, *MNRAS*, **543**, 1339
 Forrest B., et al., 2020, *ApJ*, **903**, 47
 Forrest B., et al., 2024, *ApJ*, **977**, 51
 Forrest B., et al., 2025, *arXiv e-prints*, p. [arXiv:2508.10987](https://arxiv.org/abs/2508.10987)
 Franx M., van Dokkum P. G., Förster Schreiber N. M., Wuyts S., Labbé I., Toft S., 2008, *ApJ*, **688**, 770
 Gelli V., Salvadori S., Ferrara A., Pallottini A., Carniani S., 2023, *ApJ*, **954**, L11
 Glazebrook K., et al., 2017, *Nature*, **544**, 71
 Glazebrook K., et al., 2024, *Nature*, **628**, 277
 Gobat R., et al., 2018, *Nature Astronomy*, **2**, 239
 Graham A. W., Sahu N., 2023, *MNRAS*, **518**, 2177
 Hahn O., Michaux M., Rampf C., Uhlemann C., Angulo R. E., 2020, MUSIC2-monofonIC: 3LPT initial condition generator, *Astrophysics Source Code Library*, record ascl:2008.024 (ascl:2008.024)
 Han J., Cole S., Frenk C. S., Benítez-Llambay A., Helly J., 2018, *MNRAS*, **474**, 604

⁸ openai.com

Harbord K. E., Power C., Robotham A. S. G., Cortese L., Taranu D. S., 2019, *MNRAS*, **483**, 249

Hardwick J. A., Cortese L., Obreschkow D., Catinella B., Cook R. H. W., 2022, *MNRAS*, **509**, 3751

Hartley A. I., et al., 2023, *MNRAS*, **522**, 3138

Hartmann E. A., Martín-Navarro I., Huertas-Company M., Benedetti J. P. V., Iglesias-Navarro P., Vazdekis A., Montes M., 2025, *A&A*, **694**, L7

Häussler B., et al., 2007, *ApJS*, **172**, 615

Hirashita H., Voshchinnikov N. V., 2014, *MNRAS*, **437**, 1636

Hoyle F., Lyttleton R. A., 1939, *Proceedings of the Cambridge Philosophical Society*, **35**, 405

Huško F., Lacey C. G., Schaye J., Nobels F. S. J., Schaller M., 2024, *MNRAS*, **527**, 5988

Huško F., et al., 2025a, arXiv e-prints, p. arXiv:2509.05179

Huško F., Lacey C. G., Roper W. J., Schaye J., Briggs J. M., Schaller M., 2025b, *MNRAS*, **537**, 2559

Ito K., et al., 2022, *ApJ*, **929**, 53

Ito K., et al., 2024, *ApJ*, **964**, 192

Ito K., et al., 2025a, *MNRAS*, **538**, 1501

Ito K., et al., 2025b, *A&A*, **697**, A111

Izquierdo-Villalba D., Lupi A., Regan J., Bonetti M., Franchini A., 2023, arXiv e-prints, p. arXiv:2311.03152

Jespersen C. K., Carnall A. C., Lovell C. C., 2025, *ApJ*, **988**, L19

Ji Z., et al., 2024, arXiv e-prints, p. arXiv:2401.00934

Jin S., et al., 2024, *A&A*, **683**, L4

Johnson B. D., Leja J., Conroy C., Speagle J. S., 2021, *ApJS*, **254**, 22

Jones G. T., Byrne C. M., Stanway E. R., 2025, *MNRAS*, **543**, 167

Kakimoto T., et al., 2024, *ApJ*, **963**, 49

Kalita B. S., et al., 2021, *ApJ*, **917**, L17

Kawinwanichakij L., et al., 2025, arXiv e-prints, p. arXiv:2505.03089

Kennicutt Jr. R. C., 1998, *ApJ*, **498**, 541

Kennicutt R. C., Evans N. J., 2012, *ARA&A*, **50**, 531

Kimmig L. C., Remus R.-S., Seidel B., Valenzuela L. M., Dolag K., Burkert A., 2025, *ApJ*, **979**, 15

Kokorev V., et al., 2024, *ApJ*, **975**, 178

Kriek M., van Dokkum P. G., Labbé I., Franx M., Illingworth G. D., Marchesini D., Quadri R. F., 2009, *ApJ*, **700**, 221

Krumholz M. R., Gnedin N. Y., 2011, *ApJ*, **729**, 36

Krumholz M. R., McKee C. F., Klein R. I., 2005, *ApJ*, **618**, 757

Kurinchi-Vendhan S., Farcay M., Hirschmann M., Valentino F., 2024, *MNRAS*, **534**, 3974

Lacey C. G., et al., 2016, *MNRAS*, **462**, 3854

Lagos C. d. P., Schaye J., Bahé Y., van de Sande J., Kay S. T., Barnes D., Davis T. A., Dalla Vecchia C., 2018, *MNRAS*, **476**, 4327

Lagos C. d. P., Emsellem E., van de Sande J., Harbord K. E., Cortese L., Davison T., Foster C., Wright R. J., 2022, *MNRAS*, **509**, 4372

Lagos C. d. P., et al., 2024, *MNRAS*, **531**, 3551

Lagos C. d. P., et al., 2025a, arXiv:2512.11309, p. arXiv:2512.11309

Lagos C. d. P., et al., 2025b, *MNRAS*, **536**, 2324

Lee S.-K., Im M., Kim J.-W., Lotz J., McPartland C., Peth M., Koekemoer A., 2015, *ApJ*, **810**, 90

Lee M. M., et al., 2024, *MNRAS*, **527**, 9529

Leja J., Carnall A. C., Johnson B. D., Conroy C., Speagle J. S., 2019a, *ApJ*, **876**, 3

Leja J., et al., 2019b, *ApJ*, **877**, 140

Leśniewska A., Hjorth J., Gall C., 2025, *A&A*, **699**, A352

Lim S., Tacchella S., Maiolino R., Lovell C. C., Schaye J., 2025, arXiv e-prints, p. arXiv:2511.09618

Long A. S., Casey C. M., Lagos C. d. P., Lambrides E. L., Zavala J. A., Champagne J., Cooper O. R., Cooray A. R., 2023, *ApJ*, **953**, 11

Long A. S., et al., 2024, *ApJ*, **970**, 68

Looser T. J., et al., 2024, *Nature*, **629**, 53

Lorenzon G., et al., 2025, *A&A*, **693**, A118

Lovell C. C., et al., 2023, *MNRAS*, **525**, 5520

Ludlow A. D., Schaye J., Schaller M., Richings J., 2019, *MNRAS*, **488**, L123

Ludlow A. D., Fall S. M., Wilkinson M. J., Schaye J., Obreschkow D., 2023, *MNRAS*, **525**, 5614

Magdis G. E., et al., 2021, *A&A*, **647**, A33

Man A., Belli S., 2018, *Nature Astronomy*, **2**, 695

Martínez-Marín M., Glazebrook K., Nanayakkara T., Jacobs C., Labbé I., Kacprzak G. G., Papovich C., Schreiber C., 2024, *MNRAS*, **531**, 3187

McConachie I., et al., 2025, arXiv e-prints, p. arXiv:2510.25024

McGibbon R., Helly J., Schaye J., Schaller M., Vandenbroucke B., 2025, *The Journal of Open Source Software*, **10**, 8252

McKinnon R., Torrey P., Vogelsberger M., Hayward C. C., Marinacci F., 2017, *MNRAS*, **468**, 1505

Merlin E., et al., 2018, *MNRAS*, **473**, 2098

Michaux M., Hahn O., Rampf C., Angulo R. E., 2021, *MNRAS*, **500**, 663

Mitchell P. D., Schaye J., Bower R. G., 2020, *MNRAS*, **497**, 4495

Muzzin A., et al., 2025, arXiv e-prints, p. arXiv:2507.19706

Nanayakkara T., Esdale J., Glazebrook K., Espejo Salcedo J. M., Durre M., Jacobs C., 2022, *Publ. Astron. Soc. Australia*, **39**, e002

Nanayakkara T., et al., 2025, *ApJ*, **981**, 78

Narayan R., Yi I., 1995, *ApJ*, **452**, 710

Narayan R., Igumenshchev I. V., Abramowicz M. A., 2003, *PASJ*, **55**, L69

Narayan R., Chael A., Chatterjee K., Ricarte A., Curd B., 2022, *MNRAS*, **511**, 511

Newman A. B., Belli S., Ellis R. S., Patel S. G., 2018, *ApJ*, **862**, 126

Nobels F. S. J., Schaye J., Schaller M., Bahé Y. M., Chaikin E., 2022, *MNRAS*, **515**, 4838

Nobels F. S. J., Schaye J., Schaller M., Ploeckinger S., Chaikin E., Richings A. J., 2024, *MNRAS*, **532**, 3299

Ormerod K., et al., 2024, *MNRAS*, **527**, 6110

Pacifci C., et al., 2023, *ApJ*, **944**, 141

Park M., et al., 2024, *ApJ*, **976**, 72

Pascalau R. G., et al., 2025, arXiv e-prints, p. arXiv:2505.06349

Paxton B., et al., 2015, *ApJS*, **220**, 15

Pillepich A., et al., 2018, *MNRAS*, **473**, 4077

Ploeckinger S., Richings A. J., Schaye J., Trayford J. W., Schaller M., Chaikin E., 2025, arXiv e-prints, p. arXiv:2506.15773

Regan J., Volonteri M., 2024, *The Open Journal of Astrophysics*, **7**, 72

Remus R.-S., Kimmig L. C., 2025, *ApJ*, **982**, 30

Ricarte A., Narayan R., Curd B., 2023, *ApJ*, **954**, L22

Richings A. J., Schaye J., Oppenheimer B. D., 2014a, *MNRAS*, **440**, 3349

Richings A. J., Schaye J., Oppenheimer B. D., 2014b, *MNRAS*, **442**, 2780

Robotham A. S. G., Bellstedt S., Lagos C. d. P., Thorne J. E., Davies L. J., Driver S. P., Bravo M., 2020, *MNRAS*, **495**, 905

Ruffert M., Arnett D., 1994, *ApJ*, **427**, 351

Schaller M., et al., 2024, *MNRAS*, **530**, 2378

Schaye J., et al., 2015, *MNRAS*, **446**, 521

Schaye J., et al., 2025, arXiv e-prints, p. arXiv:2508.21126

Schmidt M., 1959, *ApJ*, **129**, 243

Scholtz J., et al., 2024, arXiv e-prints, p. arXiv:2405.19401

Schreiber C., et al., 2018, *A&A*, **618**, A85

Sersic J. L., 1968, *Atlas de Galaxias Australes*

Setton D. J., et al., 2024, *ApJ*, **974**, 145

Shakura N. I., Sunyaev R. A., 1973, *A&A*, **24**, 337

Shibuya T., et al., 2025, *PASJ*, **77**, 21

Shuntov M., et al., 2025, arXiv e-prints, p. arXiv:2511.05259

Sądowski A., Narayan R., McKinney J. C., Tchekhovskoy A., 2014, *MNRAS*, **439**, 503

Slob M., et al., 2025, arXiv e-prints, p. arXiv:2506.04310

Somerville R. S., Davé R., 2015, *ARA&A*, **53**, 51

Sommovigo L., Algeria H., 2025, *MNRAS*, **540**, 3693

Spilker J., et al., 2018, *ApJ*, **860**, 103

Springel V., Di Matteo T., Hernquist L., 2005, *MNRAS*, **361**, 776

Stefanon M., Marchesini D., Rudnick G. H., Brammer G. B., Whitaker K. E., 2013, *ApJ*, **768**, 92

Stevenson S. D., et al., 2025, arXiv e-prints, p. arXiv:2509.06913

Straut V., et al., 2023, *ApJ*, **949**, L23

Suess K. A., Kriek M., Price S. H., Barro G., 2019, *ApJ*, **877**, 103

Suess K. A., et al., 2022, *ApJ*, **935**, 146

Suzuki T. L., et al., 2022, *ApJ*, **936**, 61

Szpileja J., Davé R., Rennehan D., Cui W., Hough R. T., 2025, *MNRAS*, **537**, 1849

Tacconi L. J., Genzel R., Sternberg A., 2020, *ARA&A*, **58**, 157

Tchekhovskoy A., Narayan R., McKinney J. C., 2010, *ApJ*, **711**, 50
 Trayford J. W., et al., 2025, arXiv e-prints, p. arXiv:2505.13056
 Tsai J. C., Mathews W. G., 1995, *ApJ*, **448**, 84
 Valentino F., et al., 2020, *ApJ*, **889**, 93
 Valentino F., et al., 2023, *ApJ*, **947**, 20
 Wang B., et al., 2025a, *ApJ*, **987**, 184
 Wang T., et al., 2025b, *ApJ*, **988**, L35
 Weaver J. R., et al., 2022, *ApJS*, **258**, 11
 Weibel A., et al., 2025, *ApJ*, **983**, 11
 Weller E. J., Pacucci F., Ni Y., Hernquist L., Park M., 2025, *ApJ*, **979**, 181
 Wendland H., 1995, *Advances in Computational Mathematics*, **4**, 8
 Whitaker K. E., et al., 2021a, *Nature*, **597**, 485
 Whitaker K. E., et al., 2021b, *ApJ*, **922**, L30
 White S. D. M., Frenk C. S., 1991, *ApJ*, **379**, 52
 Williams C. C., et al., 2024, *ApJ*, **968**, 34
 Wright R. J., Somerville R. S., Lagos C. d. P., Schaller M., Davé R., Anglés-Alcázar D., Genel S., 2024a, *MNRAS*, **532**, 3417
 Wright L., et al., 2024b, *ApJ*, **964**, L10
 Yang T., et al., 2025, arXiv e-prints, p. arXiv:2510.12235
 Yi S. K., et al., 2005, *ApJ*, **619**, L111
 Zhang Y., et al., 2025, arXiv e-prints, p. arXiv:2508.08577
 Zhukovska S., Gail H. P., Trieloff M., 2008, *A&A*, **479**, 453
 de Graaff A., et al., 2025, *Nature Astronomy*, **9**, 280
 van Dokkum P. G., et al., 2008, *ApJ*, **677**, L5
 van der Wel A., et al., 2011, *ApJ*, **730**, 38
 van der Wel A., et al., 2014, *ApJ*, **788**, 28

APPENDIX A: SELECTION CRITERIA OF MQGS

We analyse how different selection criteria for MQGs may affect our results, focusing on the evolution of number densities in our fiducial L200m6 simulation (Fig. A1).

First, we test the impact of the aperture used by SOAP to compute M_\star and SFR (see § 3). In the left panel, we compare our fiducial 50 pkpc spherical aperture with 10 pkpc (similar to the observational aperture to measure *JWST* colours) and 30 pkpc. The results show minor differences, consistent with the compact nature of MQGs (§ 4.5).

Second, we examine how the definition of SFR might bias the selection. Observations typically measure SFRs averaged over different timescales depending on wavelength coverage and band availability (Kennicutt 1998). While our fiducial choice is the instantaneous SFR, the middle panel shows results using 10 Myr and 100 Myr averages, representative of observational tracers. Note, however, that if the time between snapshots is less than the averaging time, then the value is averaged over the time between snapshots. The number densities remain essentially unchanged, indicating that these galaxies have been quiescent on average over such timescales. This implies that their SFHs are not noisy, and our choice of SFR definition does not bias the results.

Finally, in the right panel, we explore alternative definitions of “massive” and “quenched”. Excluding satellites (blue–black bi-coloured solid line), identified by HBT-HERONS, does not have a great impact, particularly at $z \gtrsim 3$. These satellite galaxies are already quenched by AGN feedback, as evidenced by their more massive BHs in Fig. 10, supporting the idea that their dense environments accelerate feedback. In contrast, quenching due to environmental processes is not yet dominant at such high- z . The central–satellite hierarchy is determined with HBT-HERONS: in FoF groups with multiple substructures, the central subhalo is identified by retained mass and orbital kinetic energy in the group’s centre-of-mass frame. At the high redshifts we are interested in, the number fraction of MQG satellites relative to centrals is ≈ 0.31 at $z = 2$, ≈ 0.26 at $z = 3$, ≈ 0.13 at $z = 4$, ≈ 0.18 at $z = 5$, and 0.00 at $z = 6$ for L200m6.

For quenching, adopting a constant threshold of $\text{sSFR} < 10^{-10} \text{ yr}^{-1}$, as often in the literature (e.g. Weibel et al. 2025; Zhang et al. 2025), yields results similar to our redshift-dependent definition, with differences emerging mainly at $z \gtrsim 5$ where both definitions diverge more. A stricter cut of $\text{sSFR} < 10^{-11} \text{ yr}^{-1}$ produces much lower number densities, showing that most of the MQGs in COLIBRE retain some residual star formation. This threshold has frequently been used to identify quiescent galaxies at high redshift in pre-*JWST* studies (e.g. Stefanon et al. 2013), although some *JWST* sources also satisfy this criterion (e.g. some galaxies in Nanayakkara et al. 2025). Increasing the mass threshold to $M_\star > 10^{10.5} M_\odot$ reduces number densities slightly, indicating that MQGs are generally massive but not extreme outliers.

APPENDIX B: THE EFFECT OF ERROR CONVOLUTION ON THE NUMBER DENSITIES OF MQGS

In Fig. B1, we illustrate the impact of adopting different values for the width of the Gaussian-distributed convolution applied to the simulation properties independently (M_\star and SFR), intended to represent a reasonable error budget for these quantities. The top panel shows the effect of increasing the common standard deviation applied to both M_\star and SFR. The bottom panel presents a similar analysis but fixing the width of the M_\star convolution to 0.1 dex, while varying the width applied to the SFR in the range 0.1 – 0.4 dex. This choice is motivated by the fact that stellar mass estimates are generally better constrained than SFRs. In both panels, we find that increasing the convolution scatter leads to higher inferred number densities, as expected. Even when adopting a relatively small error budget for stellar masses (bottom panel), the resulting number densities increase sufficiently due to the SFR error to more consistently reproduce the latest observational data (in red and dark red).

Chaiquin et al. (2025b) report a similar effect, showing that adding scatter to simulated M_\star values (comparable to the uncertainties introduced in § 4.1.1) has a significant impact on MQG number densities. Specifically, they find that increasing the scatter raises the number densities at higher redshifts and in higher stellar-mass bins. The dependence on scatter amplitude is explored in their Fig. D3, albeit using a slightly different sample selection and including Poisson uncertainties. In general, a larger scatter produces a stronger increase in the number densities at fixed redshift and stellar mass.

The exact impact of the different sources of errors in the derived stellar masses and SFRs has been subject to extensive discussion in the literature (e.g. Robotham et al. 2020; Pacifici et al. 2023; Bellstedt & Robotham 2025). For the population of high- z massive quenched galaxies, Nanayakkara et al. (2025) show that random errors in stellar masses have a magnitude ≈ 0.09 dex, but that systematic errors can shift the derived values by as much as ≈ 0.4 dex. Our purpose is not to isolate the magnitude of different errors, but to demonstrate the effect an error budget of ≈ 0.1 – 0.4 dex can have on the derived number densities of massive quenched galaxies.

APPENDIX C: ERROR CONVOLUTION ON THE STELLAR MASS FUNCTIONS OF MQGS

In this appendix, we examine the impact of applying a Gaussian-distributed convolution, centred at 0 with a width of $\sigma = 0.3$ dex, to the simulated stellar masses and SFRs independently when computing the SMF of MQGs in the fiducial L200m6 simulation. The error-convolved SMF at $z = 3$ is shown in Fig. 4 and compared

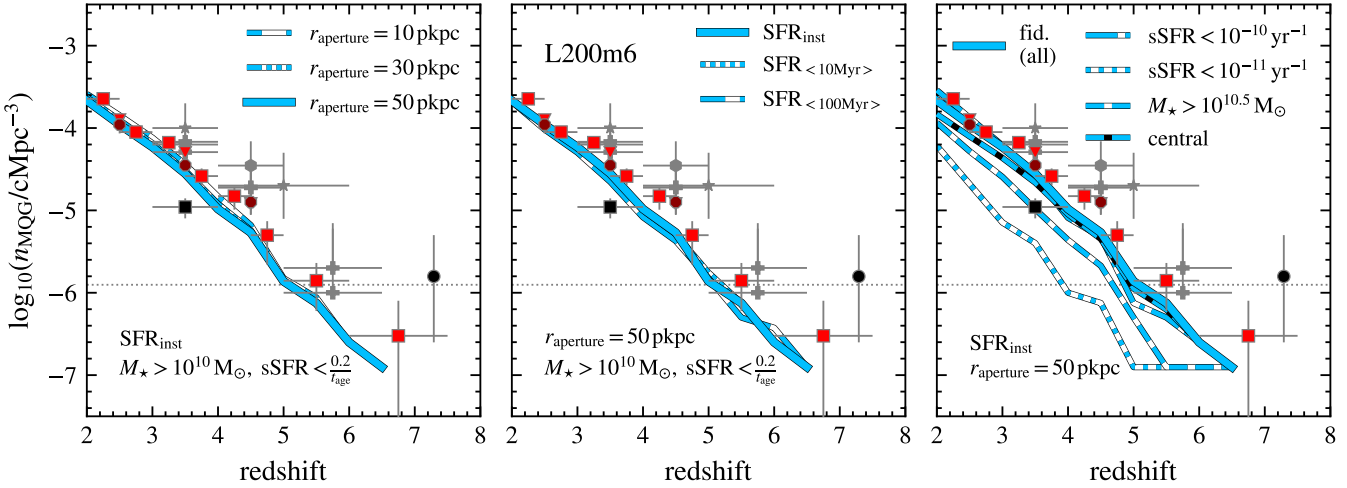


Figure A1. Comoving number density of MQGs as a function of redshift for different selection criteria. The panels show variations in aperture size for galaxy properties (left), instantaneous versus time-averaged SFR definitions (middle), and alternative ‘massive’ and ‘quenched’ thresholds (right), applied to the fiducial L200m6 simulation. Blue solid lines indicate the fiducial MQG selection described in § 3.1: $r_{\text{aperture}} = 50 \text{ pkpc}$, $\text{SFR}_{\text{inst}} M_{\star} > 10^{10} \text{ M}_{\odot}$, and $\text{sSFR} < 0.2/t_{\text{age}}$. Observational data are the same as in Fig. 2. The horizontal dotted line denotes the threshold of 10 galaxies, below which the statistics become unreliable.

with predictions from other galaxy formation and evolution models; here, we extend this analysis to the full redshift range $2 \leq z \leq 7$. In Fig. 4, we found that, relative to the latest *JWST* observations, the highest-mass end of the SMF and the predictions at $z \gtrsim 5$ lie towards the lower end of the observationally inferred range. When the same error convolution is applied across all redshifts, we find that it increases the number of systems in both regimes, thereby alleviating these discrepancies once potential uncertainties in the derivation of stellar masses and SFRs are taken into account.

APPENDIX D: STAR FORMATION HISTORIES OF MQGS

We present in this appendix a comparison between the SFH shapes of MQGs selected from our fiducial L200m6 simulation and those derived observationally via SED fitting. These SFHs are used to obtain the timescales described in § 3.2 and analysed in § 4.3.

Fig. D1 shows the median SFHs from COLIBRE (blue-palette solid lines) for different redshifts, $2 \leq z \leq 4$, compared with observational SFHs from Nanayakkara et al. (2025) in dark grey and Baker et al. (2025c) in red. Each panel corresponds to a stellar mass bin: the top panel shows low-mass MQGs and the bottom panel high-mass MQGs. In the simulations, higher selection redshifts correspond to more bursty SFHs. With less cosmic time available, galaxies must assemble through more intense starbursts, leading to higher peaks and distributions skewed towards later times, consistent with the discussion in § 3.2. As expected, the less massive MQGs (top panel) require less extreme bursts, reflected in their lower SFR values. The observations show similar behaviour: less bursty and more extended SFHs in the low-mass bin.

Interestingly, the Baker et al. (2025c) SFHs tend to assemble mass earlier than those of Nanayakkara et al. (2025). This is partly because the Baker et al. (2025c) sample is more skewed towards lower redshifts, but methodological differences in the SED fitting also contribute. Both studies use PROSPECTOR, but their assumptions differ in several ways. They do not cover the same spectral range: Nanayakkara et al. (2025) include the observed frame NIR ($\lambda = 1 - 5 \mu\text{m}$), while Baker et al. (2025c) use rest-frame $\lambda > 0.35 \mu\text{m}$ for the spectrum to avoid the less well-understood rest-frame UV (while the entire SED

for the photometry). Both adopt non-parametric SFHs, but one uses a flat continuity prior (Leja et al. 2019a) and the other an exponentially increasing prior in lookback time. They also use different lookback time intervals, and different SSP models: C3K (Conroy et al. 2009) for Nanayakkara et al. (2025) versus MILES (Falcón-Barroso et al. 2011) for Baker et al. (2025c). On the other hand, both employ MIST isochrones (Paxton et al. 2015) (which assumes fixed solar abundances), a Chabrier (2003) IMF, and the Calzetti et al. (2000) dust attenuation law and uniform metallicity priors.

These methodological differences explain the behaviours seen in Fig. 5. Overall, despite observational biases, the simulation results reproduce the qualitative features of the observed SFHs.

APPENDIX E: SIZES AND KINEMATICS OF MQGS FOR THE L400M7 SIMULATION

We show results analogous to those in § 4.5 and § 4.6 for the fiducial L200m6 simulation, but now for L400m7 in Fig. E1. We also comment on the L200m7h run where it differs. These results should be interpreted with caution because the larger gravitational softening lengths in these simulations (Table 1) shift the non-reliable regime to less compact systems.

In the top panel, we show the galaxy size–mass relation, which extends up to $z = 5$ owing to the larger volume of the L400m7 box. The blue arrows on the left-hand side indicate the corresponding softening length. Relative to L200m6, L400m7 displays a break in the power-law relation at slightly lower stellar masses ($M_{\star} \sim 10^{10.6} \text{ M}_{\odot}$). L200m7h, in contrast, shows a shallower decrease in size with stellar mass beyond this break. The flattening at the low-mass end persists, suggesting it is not a direct consequence of the softening length.

For the bottom panel, which presents the stellar kinematics via v_{\star}/σ_{\star} versus stellar mass, galaxies in L400m7 exhibit larger scatter at the high-mass end compared to L200m6. The contrast between MQGs and MSFGs is even more pronounced (especially in L200m7h), where MSFGs display substantially higher rotational support, and MQGs are more dispersion-dominated, effectively reversing the trend seen in L200m6 and suggesting that morphological transformation may precede quenching. However, these differences

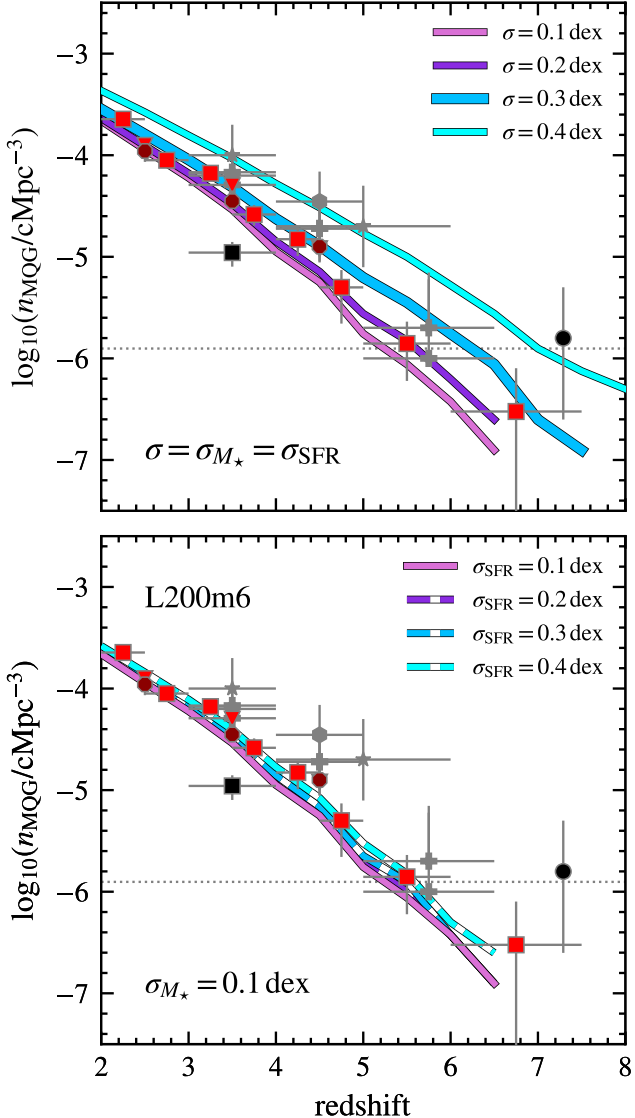


Figure B1. Comoving number density of MQGs as a function of redshift for different values of the Gaussian-distributed width applied independently to M_\star and SFR when convolving these quantities with potential observational uncertainties. The panels show variations in the convolution width applied to both M_\star and SFR when the two are assigned the same value (top), and variations in the SFR convolution width while fixing the M_\star scatter to 0.1 dex (bottom); applied to the fiducial L200m6 simulation. The blue solid line indicates the fiducial error budget used in § 4.1 and 4.2: 0.3 dex in both M_\star and SFR. Observational data are the same as in Fig. 2. The horizontal dotted line denotes the threshold of 10 galaxies, below which the statistics become unreliable.

should be interpreted cautiously, as the larger softening lengths in these runs likely affect the reliability of the kinematic measurements.

APPENDIX F: CORRELATIONS FOR MQGS

We present correlations for MQGs predicted by the COLIBRE model. Figs. F1 and F2 show several relations, with median values of Y versus X properties indicated in different colours for different selection redshifts ($2 \leq z \leq 4$) in the L200m6 simulation. Scatter points in the background represent individual galaxies selected at $z = 2$,

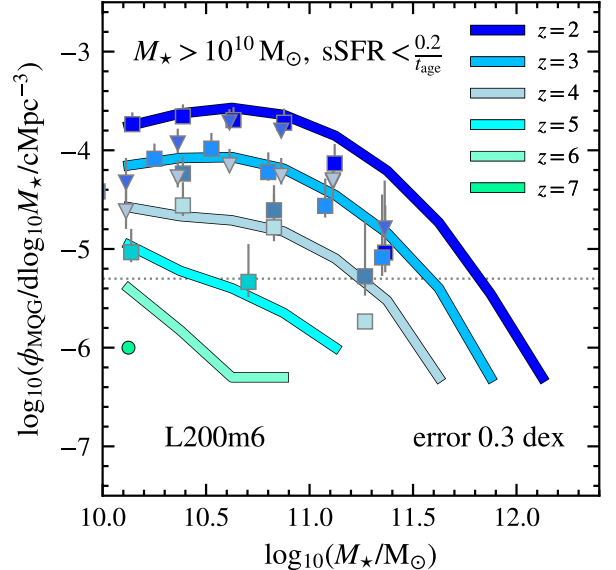


Figure C1. Stellar mass function of MQGs at different redshifts $2 \leq z \leq 7$ for the fiducial L200m6 simulation, where M_\star and SFR values in the simulations are convolved independently with a Gaussian distribution (mean 0, standard deviation 0.3 dex) representing a reasonable error budget for these quantities. Observational data are the same as in Fig. 4. The horizontal dotted line denotes the threshold of 10 galaxies, below which the statistics become unreliable.

colour-coded by a third Z property. In Fig. F1, satellite MQGs are highlighted with red scatter points; while Fig. F2 focuses on halo properties, using only central MQGs.

F1 Galaxy-related properties

Fig. F1 shows correlations involving galaxy properties discussed in § 4. In the left panel, we plot dust fraction versus quenching timescale, showing that galaxies that quenched earlier have lower dust content relative to their stellar mass. This relation becomes steeper at higher redshifts, indicating that dust is depleted after quenching, with no significant regrowth. The dust removal seems to be quicker the higher the redshift, as recently reported observationally with AGN as the main responsible mechanism (Leśniewska et al. 2025). The scatter points further show that dust fraction and H_2 fraction for MQGs, indicating that molecular hydrogen and dust are removed consistently in these systems. The points are colour-coded in this case by gas metallicity (measured within the 50 pkpc fiducial aperture as the linear sum of the diffuse oxygen over hydrogen ratio of gas, multiplied with the gas mass), showing that, as expected, more metal-rich systems have higher dust fractions. A tail of systems with relatively high metallicity but low dust fraction ($f_{\text{dust}} \lesssim 10^{-4}$) corresponds to satellite galaxies (in red).

The right panel presents galaxy size versus formation timescale, indicating that earlier-formed galaxies are more extended, having had more time to grow. This trend reflects hierarchical structure formation, where objects start smaller and grow over time. Colour-coding by quenching timescales further demonstrates that formation and quenching times are correlated. We also identify a shallower trend in which earlier-formed galaxies inhabit more massive haloes, a direct link between DM haloes and galaxies (White & Frenk 1991).

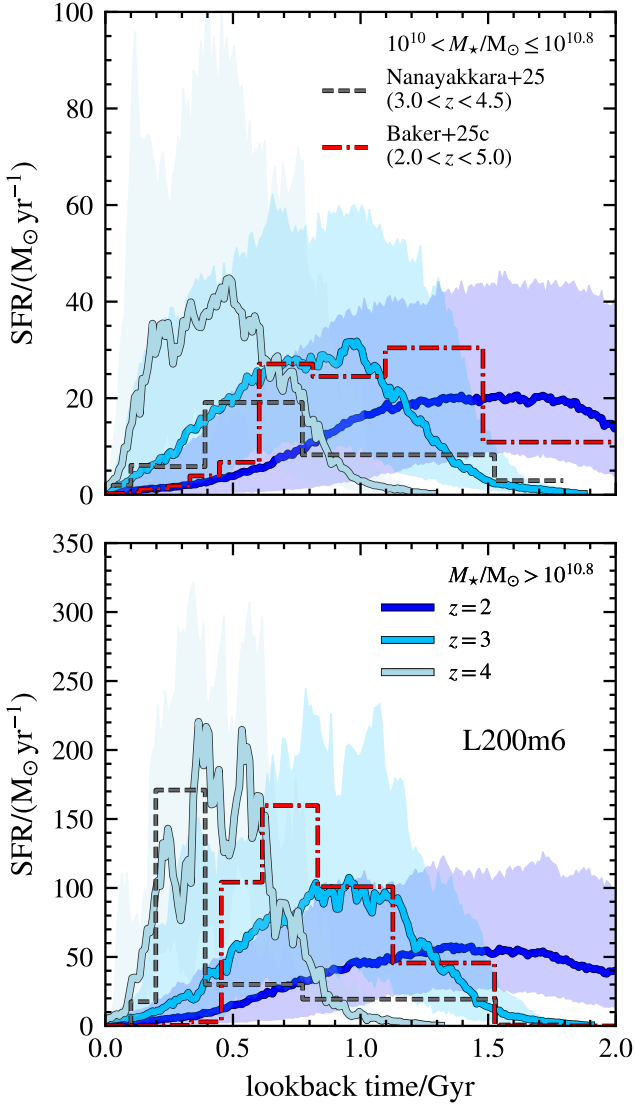


Figure D1. Star formation histories of MQGs. Solid lines show the median predictions from the L200m6 COLIBRE simulation at redshifts $2 \leq z \leq 4$, with different colours indicating selection redshift and shaded regions showing the 16th and 84th percentile range. These are compared to *JWST* spectroscopic measurements: dashed lines indicate the medians from Nanayakkara et al. (2025) and Baker et al. (2025c). Top: MQGs with $10^{10} < M_\star/M_\odot \leq 10^{10.8}$. Bottom: MQGs with $M_\star/M_\odot > 10^{10.8} M_\odot$.

F2 Environment-related properties

Correlations related to the environment are shown in Fig. F2. In the left panel, more rotation-supported systems tend to reside in lower-mass haloes. Denser environments correspond to larger haloes, as shown in the right panel, where the three environmental tracers used in this paper (halo mass, number of BH mergers, and $\delta_{\sigma_{\text{subh,rel}}(< R)}$, the deviation from the mean subhalo density contrast (§ 3.4)) are strongly correlated. Denser environments also host more massive black holes and greater feedback energy, as seen in the middle panel and discussed in § 5. Consequently, the loss of rotation in MQGs within dense environments is due to feedback disrupting their rotational support. This is in agreement with the observational results in (Kawinwanichakij et al. 2025), where more dispersion-supported systems live in denser environments, highlighting the role of envi-

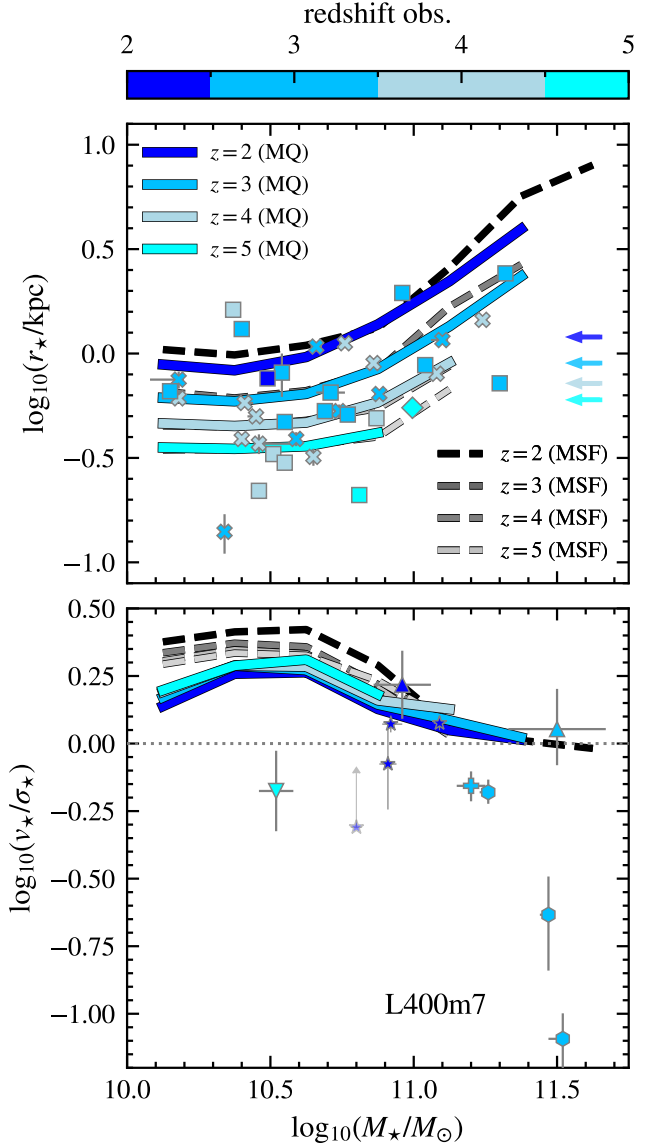


Figure E1. Stellar size-mass relation, with r_\star defined as the half-mass radius (top panel); and v_\star/σ_\star versus stellar mass relation for L400m7. Solid blue-palette lines show the median predictions for MQGs, and dashed grey-palette lines for MSFGs at different selection redshifts, $2 \leq z \leq 5$. Observational data of MQGs are the same as in Fig. 8. Arrows in the error bars indicate lower limits for galaxies where rotational velocity could not be constrained (also shown with a more faded colour). Blue arrows in the size-mass relation mark the gravitational softening length, ϵ_{prop} , at each redshift.

ronment in shaping morphology at such early times. Colour-coding by galaxy size in the left panel indicates that rotation-supported systems are more compact than dispersion-supported systems, a direct consequence of their later formation times (right panel of Fig. F1).

APPENDIX G: THERMAL VS HYBRID MODEL AT SAME RESOLUTION

In this appendix, we examine how the differences between thermal and hybrid AGN feedback models (in § 4.1 and § 5) arise from BH-related physics. To isolate the effects of feedback, we compare simulations with the same volume and resolution, namely L200m7

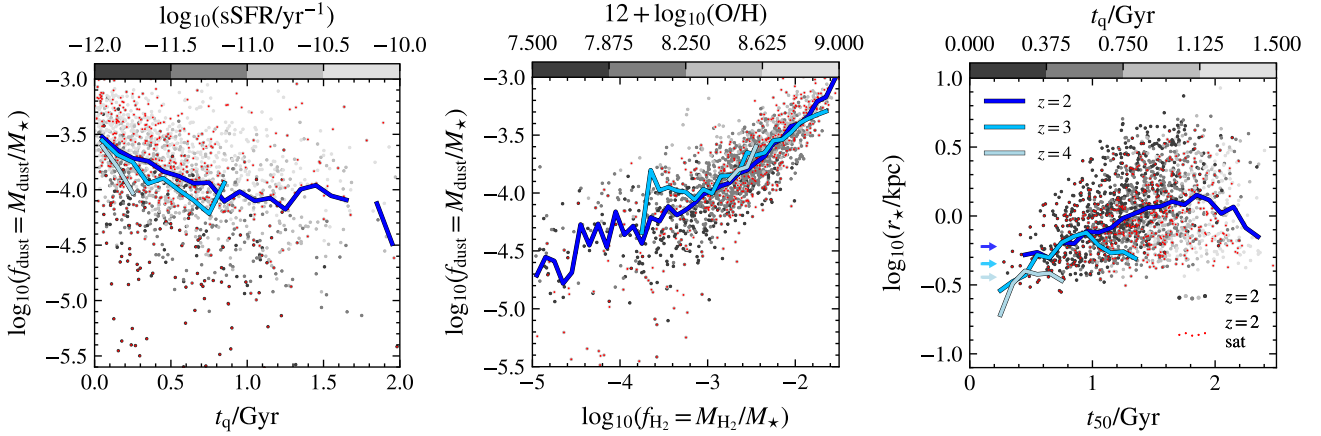


Figure F1. Dust fraction ($f_{\text{dust}} = M_{\text{dust}}/M_{\star}$) versus quenching time, colour-coded by sSFR (left panel); dust fraction ($f_{\text{dust}} = M_{\text{dust}}/M_{\star}$) versus molecular hydrogen fraction ($f_{\text{H}_2} = M_{\text{H}_2}/M_{\star}$), colour-coded by gas metallicity ($12 + \log_{10}(\text{O/H})$) (middle panel); and half-mass radius versus formation timescale, colour-coded by quenching timescale (right panel) for MQGs. Solid lines show the median values at different redshifts ($z = 2, 3, 4$), while (red) scatter points represent individual (satellite) MQGs selected at $z = 2$, colour-coded by the properties indicated above. Blue arrows in the galaxy sizes mark the gravitational softening length, ϵ_{prop} , at each redshift.

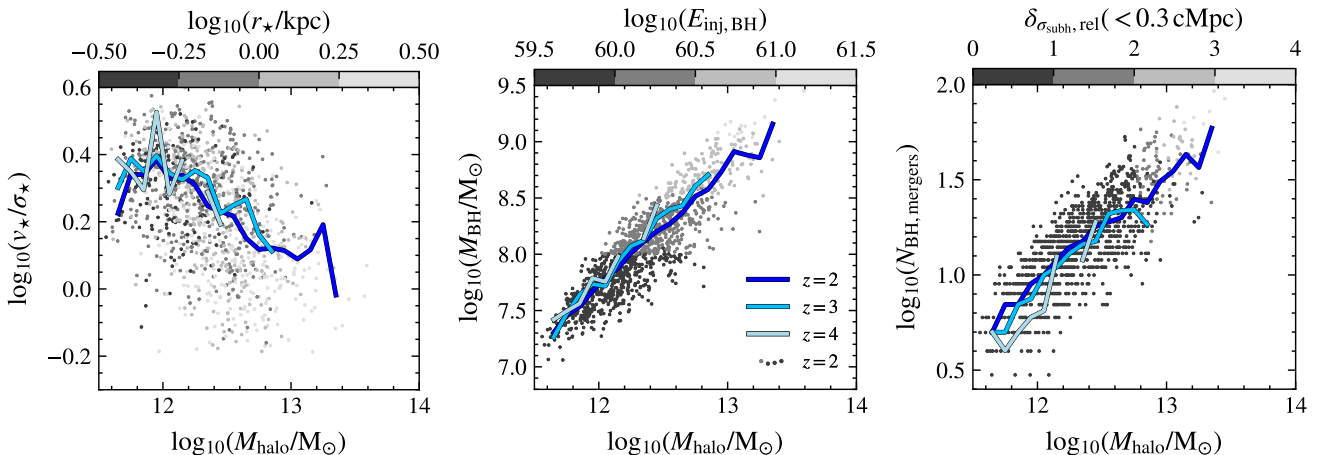


Figure F2. v_{\star}/σ_{\star} versus halo mass, colour-coded by half-mass radius (left panel); BH mass versus halo mass, colour-coded by BH-injected energy (middle panel); and number of BH mergers versus halo mass, colour-coded by $\delta_{\sigma_{\text{subh}}, \text{rel}}(< R)$ deviation from the mean subhalo density contrast, as defined in § 3.4, within a sphere of $R = 0.3$ cMpc (right panel) for MQGs. Solid lines show the median values at different redshifts ($z = 2, 3, 4$), while scatter points represent individual MQGs selected at $z = 2$, colour-coded by the properties indicated above.

(thermal) and L200m7h (hybrid). Fig. G1 shows the median relations (with the 16th and 84th percentile ranges) for all galaxies in the simulated volume: L200m7 in dotted dark blue and L200m7h in solid light blue, at $z = 2$ (first column), $z = 3$ (second), and $z = 5$ (third). The top row shows the BH–stellar mass relation. At high redshift ($z = 5$), BHs in the hybrid model grow less efficiently, especially in galaxies with $M_{\star} > 10^{10} M_{\odot}$, which are the focus of this study.

The middle row presents BH-injected energy as a function of BH mass. Although BHs are less massive in the hybrid model at early times, they are more efficient at injecting energy, with the jet model (thin black dotted line) dominating the contribution, consistent with fig. 14 in Huško et al. (2025a) and § 5.1. This is an indication of BH self-regulating its evolution (Booth & Schaye 2009).

The bottom row shows BH-injected energy versus stellar mass. At $z = 5$, the most massive galaxies in the hybrid simulation receive less injected energy than in the thermal case. By $z \approx 2 - 3$, however, the hybrid simulation reaches comparable or even higher values. Despite this, the thermal-only model still produces slightly

more quenching (see Fig. 4.1). Examining the jet and thermal contributions in the hybrid simulation (thin lines) suggests that jets act on longer timescales to be effective at quenching galaxies, as the thermal component remains consistently below the thermal-only case.

This paper has been typeset from a \TeX / \LaTeX file prepared by the author.

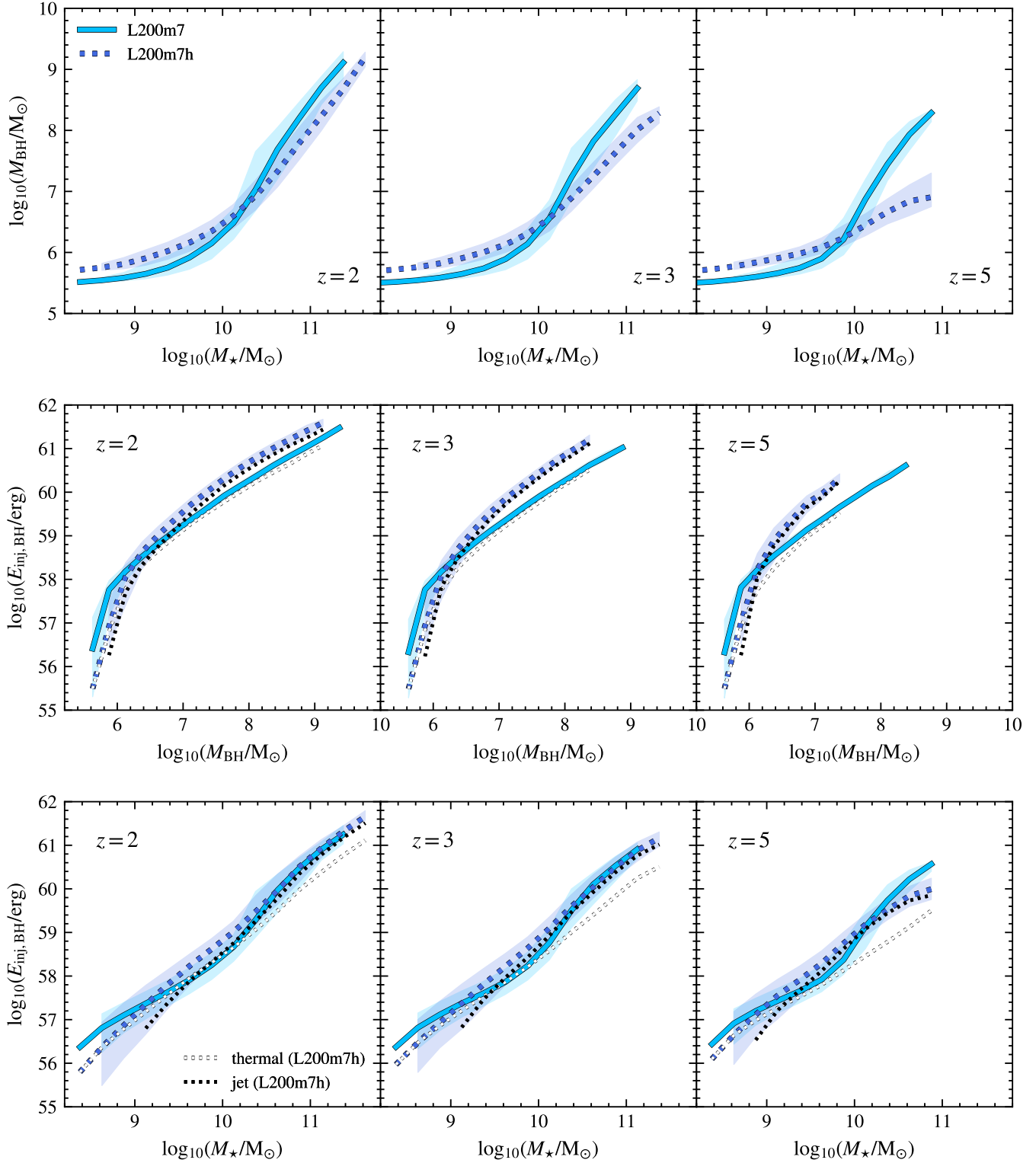


Figure G1. BH mass-stellar mass relation (first row), BH-injected energy-BH mass relation (second row) and BH-injected energy-stellar mass relation (third row) at different redshifts ($z = 2, 3, 5$; columns). Lines show median values with the 16th and 84th percentile ranges as shaded regions: solid light blue for L200m7 and dotted dark blue for L200m7h. Grey and black narrow dotted lines indicate the thermal and jet model contributions, respectively, in L200m7h.